UNIVERSIDAD COMPLUTENSE DE MADRID
FACULTAD DE CIENCIAS FÍSICAS

Departamento de Física de la Tierra, Astronomía y Astrofísica II (Astrofísica y Ciencias de la Atmósfera)

OCEAN CIRCULATION AND HEAT CONTENT VARIABILITY FROM 1000 TO 2100 AD

MEMORIA PARA OPTAR AL GRADO DE DOCTOR
PRESENTADA POR

Pablo Ortega Montilla

Bajo la dirección de los doctores

Jesús Fidel González Rouco
María Luisa Montoya Redondo

Madrid, 2012

Ocean circulation and heat content variability from 1000 to 2100 AD

PABLO ORTEGA MONTILLA

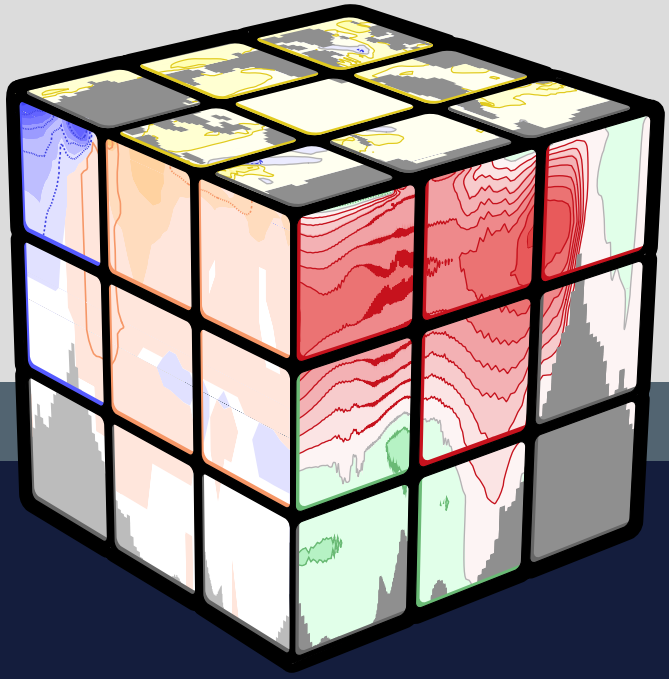

Dpto. Astrofísica y
Ciencias de la Atmósfera
Universidad Complutense de Madrid

Ocean circulation and heat content variability from 1000 to 2100 AD

Variabilidad de la circulación y contenido de calor oceánicos entre 1000 y 2100 AD

Memoria que presenta

Pablo Ortega Montilla

para optar al grado de

Doctor en Ciencias Físicas

Directores:

Dr. J. Fidel González Rouco

Dra. M^{a} Luisa Montoya Redondo

Departamento de Astrofísica y Ciencias de la Atmósfera
Facultad de Ciencias Físicas
Universidad Complutense de Madrid

II

Early chart of the Gulfstream from (Franklin, 1786). Illustration by James Poupard.

III

*The Florida Gulf-Stream is well known to issue from the Gulf of Mexico; whose waters, acquiring a higher level by accumulation, are discharged with great force and velocity through the channel between the southern Cape of Florida and the Island of Cuba: and, being subsequently opposed in front by the Bahama Archipelago, and its banks and shoals, turns northward, along the coast of North-America, skirting it, at no great distance, until it is again opposed by the banks of Nantucket and St. George, which advance far into the ocean, from the shores of New York and New England. These turn it so decidedly from the coast, that it never again returns to it; but perseveres in its newly acquired eastwardly course, through the Atlantic, passing over, or near, the tail of the Great Bank of Newfoundland, and to a point several degrees beyond it; when the stream from the Hudson's and Davis's Straits appears to give it a cast to the south-eastward. At this point, although it has made a course of more than 2,000 nautic miles, it still preserves a velocity of one mile and a quarter per hour; as also a temperature of 7 to 10 degrees of Fahrenheit's thermometer above the summer temperature of the surrounding ocean. So vast a body of water, making its way through the ocean, and carrying a breadth of 100 to 200 miles after its expansion, and with a velocity of two to 4*1/2 *miles per hour, cannot but materially affect the course of navigation. It moreover affects it in another way; for, preserving a great proportion of warmth which it acquired in the torrid zone, it influences the weather, by communicating its warmth to the incumbent atmosphere...*

James Rennell. An investigation
of the currents of the Atlantic ocean. 1832

Contents

Agradecimientos

Empezar la tesis es abrir la puerta a una aventura incierta y a la vez ilusionante. Uno se mete sin tener muy claro lo que viene, poco a poco va encontrándose las primeras dificultades, y aprende a ir superándolas casi sobre la marcha. Acabar la tesis supone algo distinto. Es una oportunidad para coger distancia y contemplar el camino recorrido. Justo ahora, desde esta perspectiva, uno es consciente de todo lo que ha aprendido y todo lo que ha cambiado. Y es ahora, más que nunca, cuando uno tiene presente a toda la gente que, de una u otra forma, le ha ayudado a llegar hasta el final. Es ahora cuando uno se siente más agradecido.

Quiero empezar dándole las gracias a Marisa y Fidel. Y también a Fidel y Marisa, que el orden de los factores no cambia el valor de la suma. Y la suma es grande porque afortunadamente sois compatibles y complementarios. Gracias por entender la ciencia como un camino sin atajos, y por acompañarla siempre de valores. Como vuestra cercanía. Saber que estáis ahí, sobre todo en los momentos de duda e incertidumbre, transmite tranquilidad y confianza en que los problemas tarde o temprano se acabarán resolviendo. Gracias también por vuestra dedicación. Siempre sacáis tiempo de debajo de las piedras si hace falta para poder atendernos. Y gracias por todos esos pequeños detalles que aunque se olvidan pronto, se van sumando poco a poco y uno siempre sabe que están ahí. Ojalá con el tiempo pueda llegar a compensaros por toda vuestra generosidad.

También me siento privilegiado de haber tenido el apoyo constante de mi familia. El de mis padres, María José y Jose Luis, José Luis y María José (tampoco importa el orden). Gracias por despertar muy pronto en mí el interés por la ciencia, y por fomentar mi curiosidad y mi espíritu crítico. Sin esa base firme seguramente no habría llegado hasta aquí. A mi hermana, Elisa, también le debo muchas cosas. Eres la pequeña pero no por ello vas detrás. Gracias por estar siempre ahí, por volcarte a los demás, por ser capaz de llegar donde otros no

alcanzamos. Y gracias también a mi cuñao escritor, Aaron, por enseñarme que las letras y las ciencias no son tan diferentes.

También está mi otra familia, mi grupo PalMA. Trabajar con vosotros es adictivo y estimulante. Hay tantas cosas que aprender de cada uno. Elena es todo naturalidad, escribe y habla en público que da gusto, y además es una todoterreno incansable, siempre 'palante' con todo. De Pedro siempre he envidiado su capacidad de concentración, su pasión por el trabajo y su constancia. Ángela llegó al grupo casi como de repente, y ahora parece que lleve toda la vida. Está siempre ahí, pendiente de todo y de todos, es un lujo tenerla con nosotros. De Volker admiro sus agallas por venirse a un país tan distinto, a sufrir las particularidades de la burocracia española. Nunca es tarde para empezar de nuevo. También está Jorge, la dosis de buen humor de cada mañana, todo honorabilidad y simpatía. Etor es imprescindible e insustituible, auténtico como ninguno. Cada día tiene algo nuevo con lo que sorprendernos. Laura irradia ilusión y alegría en todo lo que hace, y siempre consigue contagiárnosla a los demás. Ruben es un mago del balón dentro y fuera del campo, titular indiscutible en cualquier equipo. Con un poco más de suerte va a ser el pichichi de las publicaciones. De Jorge me quedo con su desparpajo y su iniciativa, y de Alex con su curiosidad sin límites, juntos hacen una mezcla explosiva, ¡que tiemble *nature*! Y qué decir de Edmundo, que apenas ha aterrizado y ya está integrado al cien por cien. O de los casipalmeros (pendientes de convalidación) Germán, Roland y Jose, que aunque no sean del grupo son como de la familia. Con esta pandilla es imposible no sentirse como en casa.

No me quiero olvidar tampoco de Belén y su 'Tropa', por su cercanía y su generosidad, cualquiera diría que somos de departamentos distintos. Gracias por acogernos al taller de atmósfera y océano. Se me va a hacer extraño no estar con vosotros en las siguientes ediciones. Ya me inventaré la manera de venir.

Por haber empezado conmigo, y por haber sido compañeros de máster, mus y aventuras recuerdo con cariño a Álvaro, Blanca y Javi. Y aunque estén un poco más lejos, también me sigo acordando de Alberto, Jose y Manolo, los otros ucofísicos exiliados. A ver si la próxima vez que vayamos al mesón 'la venta' terminamos de arreglar el mundo, o no.

Afortunadamente ni todo el monte es orégano, ni toda la vida es ciencia, ni toda la ciencia es física. Esta tesis le debe un poco a todos mis dargüins, por acogerme como un biólogo más, por su apoyo incondicional, y por haber compartido tantas fatigas y alegrías en Salamanca y alrededores. Y por supuesto también está en deuda con los otros madrileños de adopción: Vero, Isidro, Lucía, Jan, Josemi, Inés, Rafa y Elena, que han compartido tantos buenos momentos conmigo en ésta ciudad inagotable e inabarcable.

Mil gracias a todos.

Acknowledgments

There is nothing like the pleasure of saying thanks, especially when the work finally comes to an end and you feel grateful to all the people that made it possible. To be able to extend my gratitude to all the non-spanish people that has been important for me during this PhD, I will continue now in English.

First, I want to thank Hugo for inviting me to Canada, my first real experience abroad. It was a short but really encouraging stay. The month I spent with him, and with Bruce, Nick, Chance, Ashley and Etor in Antigonish was full of good moments. It was the perfect place to feel at ease with my English.

I also owe my most sincere gratitude to Ed and Rowan, who opened to me the door to the Meteorology Department in Reading, and whose dedicated efforts and kind supervising helped me to gain confidence in my work. Besides, I want to thank Deepthi, Elisa, Edgar, Kishore and Rob for offering me their friendship, in spite of all my silly talk. It was great to share all those winter barbecues with them.

From my visit to LOCEAN I also have but good memories. I feel particularly grateful to Juliette, for her hospitality and her generous help, and also to Myriam, Didier and Jerome for their valuable suggestions and advice on my work. I feel their help was decisive to overcome some issues and difficulties we encountered in the analysis of the AMOC.

I also feel indebted to all the people that made their data and programs available to us. This thesis would not have been the same without their disinterested contribution. In particular, I want to thank Stephanie for sharing the CTRL2 simulation with us, and also for clarifying several doubts on the experimental setup.

And finally, last but not least, I want to thank Lucie. It couldn't be otherwise. Meeting you was a turning point in my PhD. You helped me keep my motivation

up, accompanied me in the tough and discouraging moments, and also shared my joy when everything ended up turning out well. For this, and many other things, I feel lucky and grateful to have you at my side.

List of acronyms

AABW	Antarctic Bottom Water
AMO	Atlantic Multidecadal Oscillation
AMOC	Atlantic Meridional Overturning Circulation
AO	Arctic Oscillation
AOGCM	Atmosphere-Ocean General Circulation Model
AR1	1^{st} order Autorregresive process
CD	Convective Depth
CEOF	Complex Empirical Ortogonal Function
DWF	Deep Water Formation
EBM	Energy Balance Model
EA	East Atlantic pattern
ENSO	El Niño Southern Oscillation
EOF	Empirical Orthogonal Function
GCM	General Circulation Model
GHG	Greenhouse Gases
GSR	Greenland-Scotland Ridge
HFL	Heat Flux
IPCC	Intergovernmental Panel on Climate Change
ISD	Irminger Sea Density
ITCZ	Intertropical Covergence Zone
LIA	Little Ice Age
MCA	Medieval Climate Anomaly
MOI	Meridional Overturning Index
NADW	North Atlantic Deep Water
NAO	North Atlantic Oscillation
OHC	Ocean Heat Content

PC	Principal Component
PDO	Pacific Decadal Oscillation
PERC	Potential Energy Released by Convection
POP	Principal Oscillation Patten
RF	Radiative Forcing
SAT	Surface Air Temperature
SL	Sea Level
SLR	Sea Level Rise
SLP	Sea Level Pressure
SST	Sea Surface Temperature
UCM	Universidad Complutense de Madrid

Summary

Studies addressing climate variability during the last millennium generally focus on variables with a direct influence on climate variability, like the fast thermal response to the varying radiative forcing, or the largescale changes in atmospheric dynamics (e.g. North Atlantic Oscillation). The ocean is characterised by a delayed response to these radiative changes and produces remarkable climate impacts, but at longer timescales. Indeed, during the last glacial era, the ocean is thought to play a central role on the major climate excursions, triggered by changes in ocean circulation and thereby of the meridional heat transport. Future projections for the 21^{th} century further underline the importance of the ocean, given its high heat storage capacity and its active role on the most relevant feedback mechanisms that can enhance or modulate the global warming signal (e.g. polar albedo, slowdown of the ocean circulation).

This work focuses on the last one thousand years, the immediate context for two future climate projections, and investigates the main aspects of ocean variability as described by a set of different simulations with the ECHO-G model. Two particular quantities deserve our attention: the variability of the Atlantic meridional overturning circulation (AMOC), and the main changes in the ocean heat content (OHC). Particular emphasis is placed on their response to externally forced influences and on the potential impact of several well-known modes of climate variability.

In a first preliminary study, the processes that govern predictability of internal decadal variations in the AMOC are investigated in a long control simulation of the ECHO-G atmosphere-ocean coupled model. We elucidate the particular role of local stochastic forcing by the atmosphere and other potential ocean processes, and use the results to build a predictive regression model. The primary influence on AMOC variability is found to come from air-sea heat fluxes over the

Eastern Labrador Sea. The maximum correlation between such anomalies and the variations in the AMOC occurs at a lead time of 2 years, but we demonstrate that the AMOC integrates the heat flux variations over a period of 10 years. The corresponding univariate regression model accounts for 74.5% of the total AMOC variance (after the Ekman component has been removed). Dense anomalies to the south of the Greenland-Scotland ridge are also shown to precede the overturning variations by 4-6 years, and provide a second predictor. With the inclusion of this second predictor the resulting regression model explains 82.8% of the total variance of the AMOC. This final bivariate model is also tested during large rapid decadal overturning events. The sign of the rapid change is always well represented by the bivariate model, but the magnitude is usually underestimated, suggesting that other processes are also important for the occurrence of these large rapid decadal changes in the AMOC.

The variability of the AMOC is later investigated throughout the period 1000 to 2100 AD with several forced simulations. The main mechanisms responsible for the AMOC variability at interannual and multidecadal time scales are described. At high frequencies, the AMOC is directly responding to local wind-driven changes in the Ekman transport, associated to three different teleconnection indices: El Niño-Southern Oscillation (ENSO), the North Atlantic Oscillation (NAO), and the East Atlantic (EA) pattern. At low frequencies, the AMOC is largely controlled by convection activity south of Greenland. Again, the atmosphere is found to play a leading role on these variations. Positive anomalies of convection are preceded in 1 year by intensified zonal winds, associated in the forced runs to a positive NAO-like pattern. The sensitivity of the AMOC to three different forcing factors is also investigated. The major impact is associated to increasing greenhouse gases (GHG), in keeping with their strong radiative forcing. Indeed, starting in the Industrial Era and continuing in the future scenarios, the AMOC experiences a final decrease of up to 40% with respect to the preindustrial average. Also, a weak but significant AMOC strengthening is found in response to the major volcanic eruptions, which produce colder and saltier surface conditions over the main convection regions. In contrast, no meaningful impact of the solar forcing on the AMOC is observed.

Finally, OHC variability is also addressed in the same millennial and future climate change simulations. When compared to observations, which are available for the last 55 years, the model tends to overestimate the global trends, and underestimate the decadal OHC variability. In the context of the last millennium, the effect of initial trends on the simulated OHC is assessed by establishing a comparison with proxy reconstructions of sea level (SL). It is observed that the initial drift is almost negligible in the upper 700 m, but has a remarkable effect at deeper levels. Thereby the rest of the analysis focuses on the upper ocean.

At this depth, the main impact associated to the radiative forcing is an OHC increase at high latitudes. This OHC response is mostly associated to the effect of volcanoes during the preindustrial era, and to the increasing GHGs in the last 150 years. Yet, at local scales, internal modes of climate variability can dominate the OHC variations. For instance, upper temperature in the Equatorial Pacific is controlled by ENSO variability from interannual to multidecadal timescales. Also, both the Pacific Decadal Oscillation (PDO) and the Atlantic Multidecadal Oscillation (AMO) modulate intermittently the interdecadal OHC variability in the North Pacific and Mid Atlantic, respectively. The NAO, through its influence on North Atlantic convection and the AMOC strength, also plays an important role on the OHC at multiple timescales, leading first to a cooling in the Labrador and Irminger seas, and later on to a North Atlantic warming, through a delayed influence on the AMO.

Resumen

La Tierra es un planeta predominantemente oceánico, con un 71% de su superficie cubierta por agua (Grassl, 2001). El océano juega un papel fundamental en el clima y su variabilidad, así como en el transporte y almacenamiento de calor. La circulación oceánica es responsable de gran parte del transporte global de calor y agua dulce, y ejerce una influencia significativa en el clima a escalas global y regional. El océano, además, es una fuente de variabilidad en baja frecuencia, asociada a procesos de dinámica interna y a interacciones con otras componentes del sistema climático. También cabe destacar su alta capacidad calorífica (mil veces mayor a la de la atmósfera), gracias a la cual el océano domina la absorción de energía entrante en la Tierra (Levitus et al., 2005a).

En el contexto actual de cambio climático, caracterizado por un desequilibrio radiativo neto (Hansen et al., 2005), la importancia del océano en el clima es probablemente mayor. De hecho, variaciones significativas en variables como la circulación meridiana Atlántica de *overturning* (AMOC; del inglés Atlantic meridional overturning circulation) o el contenido de calor oceánico (OHC; del inglés ocean heat content) pueden llegar a modular o incluso intensificar la respuesta global a los gases de efecto invernadero.

La importancia del OHC va más allá de su participación en el balance radiativo terrestre. Aunque la energía transferida y almacenada en el océano profundo puede mitigar temporalmente el calentamiento en superficie, un afloramiento posterior por cambios en la dinámica oceánica puede amplificar localmente la respuesta en temperatura, y de esta forma modificar los impactos a escala regional. Además, el calentamiento reciente del océano global contribuye directamente a la subida del nivel del mar, considerada como uno de los impactos climáticos globales más importantes a afrontar durante las próximas décadas (Grinsted et al., 2010). Otros procesos, como la formación de agua profunda o la desintegración

de la capa de hielo oceánico, son también sensibles a variaciones en el contenido de calor oceánico (Hansen et al., 2005).

Asimismo, la AMOC es un factor clave para comprender el clima del Hemisferio Norte, debido a su papel fundamental en el transporte y redistribución de energía desde los trópicos, contribuyendo así a suavizar las temperaturas en Europa occidental. La AMOC, además, está relacionada con la Oscilación Multidecadal del Atlántico (AMO; del inglés Atlantic Multidecadal Oscillation), asociada a su vez con variabilidad multidecadal en distintas regiones del globo. Por ejemplo, la AMO ha sido vinculada con las temperaturas y precipitaciones de verano de Europa y Norte América, con la formación de huracanes en el océano Atlántico o con las sequías del Sahel (Sutton and Hodson, 2005; Knight et al., 2006; Zhang and Delworth, 2006, 2007).

Dada la importancia de la AMOC en el clima, y en particular en el Atlántico Norte, cabe esperar que variaciones en su intensidad o en sus características puedan conllevar variaciones climáticas considerables. En este sentido, el calentamiento global antropogénico afectaría a la circulación de dos maneras: produciendo un calentamiento de la superficie oceánica y modificando el transporte de vapor de agua hacia las altas latitudes. Ambos efectos conducirían a un mismo resultado: un descenso de la densidad de las aguas superficiales en el Atlántico Norte, que podría conllevar una disminución en la formación de agua profunda, y de esta forma debilitar la intensidad de la AMOC.

Por tanto, surge la necesidad de entender mejor cuales son los mecanismos que gobiernan la variabilidad y predictibilidad de la AMOC en el contexto de clima presente, y de investigar cómo se ven afectados por las condiciones de cambio climático futuro. La variabilidad natural de la AMOC ha sido ampliamente estudiada en simulaciones de control bajo condiciones del clima actual en diversos modelos de circulación general con atmósfera y océano acoplados (Delworth et al., 1993; Timmermann et al., 1998; Delworth and Greatbatch, 2000; Vellinga and Wu, 2004; Latif et al., 2004; Dong and Sutton, 2005; Knight et al., 2005; Jungclaus et al., 2005; Mignot and Frankignoul, 2005; Hawkins and Sutton, 2007). Estos estudios han permitido identificar varios mecanismos operando desde la escala interanual a la secular. La variabilidad interanual de la AMOC está dominada principalmente por el efecto del viento en superficie, que produce cambios en el transporte de Ekman y en la cizalladura vertical del flujo meridiano (Eden and Willebrand, 2001; Vellinga and Wu, 2004; Mignot and Frankignoul, 2005; Hirschi et al., 2007; Cabanes et al., 2008). Los cambios en los regímenes de viento están a su vez relacionados con modos de variabilidad climática como la Oscilación del Atlántico Norte (NAO; del inglés North Atlantic Oscillation) o El Niño-Oscilación del Sur (ENSO; del inglés El Niño-Southern Oscillation).

En contraste, la variabilidad interdecadal y secular de la AMOC está normalmente caracterizada por una respuesta retardada del overturning a cambios de la densidad superficial en las regiones de formación de agua profunda (e.g. Delworth et al., 1993; Timmermann et al., 1998; Delworth et al., 2002; Dong and Sutton, 2005). Sin embargo, tanto el origen como las escalas de tiempo de estos cambios suelen diferir de un modelo a otro. Por ejemplo, Delworth et al. (1993) describen una oscilación amortiguada de 50 años para el modelo GFDL, en la que un debilitamiento de la AMOC conduce a un descenso de la temperatura en latitudes subpolares del Atlántico Norte, aumentando la densidad en la región y de esta forma reforzando la intensidad del giro subpolar. Esta intensificación lleva consigo un aumento del transporte de anomalías de densidad a la región de convección, estableciendo así el mecanismo para el cambio de fase en la oscilación. Una oscilación parecida ha sido descrita por Dong and Sutton (2005) para el modelo HacCM3, aunque con una escala de tiempo sensiblemente menor (25 años). En un estudio complementario con la misma simulación del modelo HadCM3, Vellinga and Wu (2004) describen una oscilación secular, en la que la intensidad de la AMOC está ligada a desplazamientos de la zona de convergencia intertropical. Como último ejemplo, un mecanismo distinto, observado en los modelos HadCM3 (Hawkins and Sutton, 2007) y ECHAM5/MPI-OM (Jungclaus et al., 2005), relaciona las variaciones de la AMOC con descargas de agua dulce desde el Océano Ártico hacia las regiones de convección. No está claro, no obstante, hasta qué punto estos mecanismos son representativos de la realidad, y tampoco si se verían modificados por la influencia del forzamiento externo, que también puede modificar potencialmente las condiciones locales de densidad en las regiones de formación de agua profunda.

El último milenio destaca por ser uno de los periodos más relevantes para poner en contexto los cambios climáticos de origen antrópico, pues comprende un rango de variabilidad natural compatible con las condiciones actuales de forzamiento externo natural, que permite así establecer si tendencias similares a las del calentamiento actual han tenido lugar durante la era preindustrial. Además, este periodo destaca por el número de reconstrucciones (e.g. Briffa et al., 1998; Jones et al., 1998; Mann et al., 1999; Crowley and Lowery, 2000; Esper et al., 2002) y simulaciones (e.g. González-Rouco et al., 2003b; Stendel et al., 2006; Tett et al., 2007; Swingedouw et al., 2010; Hofer et al., 2011) climáticas disponibles, y también por tener estimaciones de los principales factores de forzamiento externo con una buena resolución temporal (e.g. Lean et al., 1995; Etheridge et al., 1996; Bard et al., 2000; Crowley, 2000). Sin embargo, la mayoría de los estudios realizados se centran en variables que responden directamente a los cambios en el forzamiento radiativo, como el promedio de temperaturas en superficie. Sólo

Swingedouw et al. (2010) y Hofer et al. (2011) analizan algunos aspectos de la influencia del forzamiento en la AMOC, ambos en simulaciones forzadas del último milenio, aunque con resultados bien diferentes. Por un lado, la simulación con el modelo CNRM-CM3.3 (Swingedouw et al., 2010) muestra un impacto significativo de la variabilidad solar en la NAO, que a su vez afecta a la intensidad de la AMOC varios años después. Por el otro lado, el estudio con el modelo CCSM3 (Hofer et al., 2011) concluye que la variabilidad de la AMOC no muestra una respuesta clara a los cambios en el forzamiento externo. Entender el origen de estas discrepancias no es fácil, dado que existen claras diferencias en la configuración de los modelos y en los factores de forzamiento externo considerados en cada caso. Para esclarecer la importancia de los distintos forzamientos, y sus impactos potenciales, es necesario ampliar los estudios anteriores a nuevos registros climáticos.

Objetivos

El objetivo fundamental de esta tesis es profundizar en la comprensión de la variabilidad oceánica, y más en particular de la circulación y el contenido de calor oceánicos, durante el último milenio y en dos escenarios de cambio climático. Previamente, se analizan los procesos fundamentales que determinan la formación de agua profunda y su predictibilidad en un contexto de variabilidad climática natural. También se investiga la respuesta a los distintos factores de forzamiento externo, distinguiendo los impactos potenciales que cada uno de ellos ejerce en las dos variables de estudio. Un último objetivo es determinar la influencia de otros modos o mecanismos de variabilidad interna sobre la intensidad de la AMOC por un lado, y sobre los cambios locales y globales en el contenido de calor por el otro. Este tipo de exploración se enmarca en el contexto de los llamados estudios de impacto y va a estar supeditado a la metodología y al tipo de registros utilizados durante nuestro estudio.

Aproximación metodológica

El estudio del clima del pasado se basa en la integración y comparación de distintas fuentes de información. En el caso del océano, y en especial para las variables de interés, las medidas instrumentales son muy recientes, y por tanto las series disponibles son cortas. Además, la cobertura espacial es también muy limitada. Más allá del periodo observacional existen medidas indirectas o proxy, que extraen información climática de otros registros con mayor alcance temporal. Sin

embargo, no conocemos ninguna reconstrucción de este tipo que esté directamente relacionada con la variabilidad de la circulación Atlántica o del contenido de calor. En este contexto, las simulaciones con modelos climáticos juegan un papel fundamental. En comparación con los registros proxy, las simulaciones presentan una cobertura espacial completa en tres dimensiones, tienen consistencia física y además son relativamente independientes de las observaciones. Para poder realizar simulaciones representativas del último milenio, es necesario incluir estimaciones de los forzamientos externos más importantes durante ese periodo. En nuestro caso, se han tenido en cuenta las variaciones de la irradiancia solar, el efecto radiativo de los aerosoles volcánicos, y las concentraciones de gases de efecto invernadero. No se han incluido ni los cambios en la cubierta vegetal, ni el efecto de los aerosoles atmosféricos de origen antrópico. Ambos forzamientos probablemente producen un atenuamiento de las tendencias de calentamiento en los siglos XX y XXI (Bauer et al., 2003; Osborn et al., 2006).

Para este estudio se ha utilizado el modelo de circulación general ECHO-G (Legutke and Voss, 1999), compuesto por la componente atmosférica ECHAM-4 (Roeckner et al., 1996) de resolución T30 y 19 niveles verticales, y la componente oceánica HOPE-G (Wolff et al., 1997), que tiene 20 niveles de profundidad y una resolución horizontal de ca. 2.8° x 2.8° con una discretización más fina en las regiones tropicales. Durante el desarrollo de la tesis se han analizado seis simulaciones diferentes realizadas con el modelo ECHO-G: dos simulaciones de control de mil años (CTRL1 y CTRL2), dos simulaciones forzadas del último milenio que cubren el periodo 1000 a 1990 AD (FOR1 y FOR2) y dos experimentos forzados de escenarios de futuro desde 1990 hasta 2100 (A2 y B2). Estos experimentos se han utilizado y validado previamente en numerosos estudios (González-Rouco et al., 2003a,b, 2006, 2009; von Storch et al., 2004; Zorita et al., 2003, 2005; Beltrami et al., 2006; Gouirand et al., 2007a,b; Stevens et al., 2007). Tanto en CTRL1 como en CTRL2 se ha mantenido un mismo forzamiento externo constante con valores correspondientes al clima actual ($[CO_2]$=353 ppm; $[CH_4]$=1,720 ppb; $[N_2O]$=310 ppb; constante solar=1.365 W/m^2). La principal diferencia es que CTRL1 se realizó en una versión del modelo anterior a la del resto de simulaciones. En CTRL2 y las simulaciones forzadas el código de la componente atmosférica fue traducido de f77 a f90, y la máquina se cambió de Cray C90 a NEC SX-6. Aunque en principio estos cambios no deberían introducir ninguna diferencia en los climas de control simulados, en vista de las diferencias observadas durante el análisis (ver Figura 6.1) otros cambios adicionales en la configuración del modelo no pueden descartarse. En las dos integraciones del último milenio se ha aplicado un forzamiento idéntico, obtenido a partir de observaciones y de evidencia indirecta (ver Figura 2.2). Las condiciones iniciales de FOR1 se toman del año 100 en CTRL2 y las de FOR2 del año 1700 AD en

FOR1. Durante los primeros 100 años de ambas simulaciones se va cambiando paulatinamente el forzamiento hasta alcanzar los valores estimados del año 1000 AD. Se observa que las condiciones iniciales en FOR1 son más cálidas que en FOR2 y están por encima de lo habitual en otras simulaciones de control con forzamiento actual. Esto hace que los primeros siglos de FOR1 parezcan estar afectados por un desequilibrio inicial (Goosse et al., 2005; Osborn et al., 2006) que ha de tenerse en cuenta en la interpretación de los resultados. Las dos simulaciones de futuro utilizan como condición inicial el estado simulado en FOR1 para el año 1990 AD.

Aportaciones fundamentales

A continuación se detallan los objetivos parciales que se tratan en cada capítulo.

- Capítulo 3: *Predictibilidad de la formación de agua profunda en el Atlántico Norte*

  En este capítulo se investigan las principales regiones y procesos que contribuyen a la formación de agua profunda y, por tanto, a la variabilidad de la AMOC en el modelo. Para este análisis se utiliza la simulación de control de mil años CTRL1. De esta manera, se pueden identificar los mecanismos de variabilidad natural independientes del forzamiento externo que ejercen una influencia sobre la AMOC. En particular, se intenta cuantificar la influencia en la formación de agua profunda del forzamiento estocástico de la atmósfera y de otros procesos no locales. El objetivo último es identificar nuevos predictores potenciales para desarrollar un modelo predictivo de regresión de la intensidad de la AMOC en el modelo. Este modelo de regresión se evalúa a continuación durante los episodios de variaciones rápidas e intensas de la AMOC (tanto debilitamientos como intensificaciones) y también se determinan los impactos climáticos correspondientes.
  Los resultados más importantes de este capítulo de la Tesis han sido publicados en Ortega et al. (2011b).

- Capítulo 4: *Variabilidad de la circulación Atlántica meridiana de overturning en el periodo 1000 a 2100 AD*

  Este capítulo desarrolla un estudio complementario enfocado en la variabilidad forzada de la AMOC, basado en el análisis de dos simulaciones del último milenio (FOR1 y FOR2) y dos escenarios de futuro (A2 y B2). En este caso,

por compatibilidad con las simulaciones forzadas, la simulación de control que se utiliza de referencia es CTRL2. Este conjunto de experimentos permite una comparación directa entre los aspectos generales de la variabilidad forzada y no forzada de la AMOC. Además se han considerado dos objetivos adicionales. El primero es investigar los mecanismos responsables de la variabilidad de la AMOC a escalas interanual e interdecadal, manteniendo una atención especial en las diferencias introducidas por el forzamiento. Finalmente, se realiza un análisis individualizado del impacto de cada uno de los factores de forzamiento sobre el océano, y más en particular sobre la AMOC. Los resultados más importantes de este capítulo de la Tesis han sido publicados en Ortega et al. (2011c).

- Capítulo 5: *Variabilidad del contenido de calor oceánico en el último milenio y dos escenarios del IPCC*

  En este capítulo se realiza un análisis análogo al del capítulo anterior, pero enfocado en la variabilidad forzada y no forzada del contenido de calor oceánico. Para esta variable el efecto de las condiciones iniciales se hace patente durante varios siglos (ver Figura 5.6). Por tanto, en un primer paso, las simulaciones son comparadas con otros registros disponibles para el último milenio (observaciones y reconstrucciones proxy) de variables relacionadas con el OHC, como el aumento del nivel del mar. Asimismo, en los últimos 50 años, el contenido de calor simulado es comparado con las observaciones. A continuación se investigan los impactos globales correspondientes a los distintos factores de forzamiento externo, y las contribuciones locales de varios modos de variabilidad climática natural con una influencia significativa en las temperaturas de superficie: ENSO, la Oscilación Decadal del Pacífico (PDO; del inglés Pacific Decadal Oscillation), la AMO y la NAO. El objetivo último de este análisis es avanzar en la comprensión de los procesos que potencialmente pueden modular o incluso mitigar el calentamiento reciente de los océanos (Levitus et al., 2000).
  Los resultados más importantes de este capítulo se encuentran en proceso de redacción para su posterior publicación (Ortega et al., 2011a).

Conclusiones más relevantes

Este trabajo ha contribuido a comprender mejor la variabilidad de la AMOC y el OHC en el contexto de los últimos mil años, un periodo en el que las fuentes proxy proporcionan un conocimiento limitado de ambas variables. Los resultados

y conclusiones más importantes de esta Tesis se destacan y detallan a continuación:

La predictibilidad de la formación de agua profunda, y por tanto de la AMOC, está controlada en su mayor parte en CTRL1 por la integración de flujos de calor en el Atlántico Norte. Se ha desarrollado un modelo de predicción de la intensidad de la AMOC, basado en dos predictores diferentes. El primero está asociado con la asimilación por el océano de flujos persistentes de calor desde la atmósfera en la región del mar de Labrador. Esta influencia local es integrada por el océano durante los 10 años precedentes a las variaciones de la AMOC, llegando a explicar más de un 70% de la variabilidad de la circulación cuando se filtra la señal de Ekman. El segundo predictor explica un 10% adicional de varianza y está relacionado con la acumulación de anomalías positivas de densidad al este del mar de Irminger, a su vez relacionadas con cambios locales en el giro subtropical y con la descarga de flujos de agua dulce desde los mares del Norte.

El modelo predictivo de regresión es capaz de reproducir las variaciones rápidas e intensas más importantes de la AMOC. Sin embargo, el análisis revela que otros métodos alternativos para la selección de predictores pueden llegar a mejorar la representación de estos episodios. Los cambios rápidos e intensos de la AMOC están bien descritos por el primer predictor, aunque normalmente su magnitud está sobreestimada. En cambio, la contribución del segundo predictor apenas es significativa. Esto indica que otros procesos no incluidos en el modelo de regresión pueden estar jugando un papel importante en el desarrollo de estas transiciones rápidas de la intensidad de la AMOC. También se ha observado que existe una asimetría tanto en la ocurrencia como en los impactos asociados a los debilitamientos e intensificaciones rápidas de la AMOC. Por tanto, un análisis por separado de los aumentos y disminuciones más importantes puede ayudar a la identificación de nuevos predictores para el modelo de regresión.

En las otras simulaciones con el modelo ECHO-G el viento domina la variabilidad de la AMOC tanto en alta como en baja frecuencia. La variabilidad interanual de la AMOC está controlada en gran parte por variaciones en el transporte de Ekman, vinculadas a su vez a cambios en tres modos de variabilidad climática bien conocidos: ENSO, la NAO y el patrón del Atlántico Este (EA; del inglés East Atlantic). En las escalas de tiempo decadal a secular la variabilidad de la AMOC responde a cambios en la convección profunda del mar de Labrador, favorecidos por un enfriamiento local forzado por el viento. En el caso de las simulaciones forzadas del último milenio, estos cambios en el regímen de vientos están modulados en última instancia por variaciones de la NAO. Además, el

forzamiento atmosférico produce una disminución local en el contenido de calor oceánico, tanto en las simulaciones como en las observaciones.

Otros modos de variabilidad climática natural también pueden producir cambios destacables en el contenido de calor oceánico en superficie. Además del efecto de la NAO descrito anteriormente, se ha observado que la variabilidad de ENSO y la PDO se relaciona respectivamente con un calentamiento tropical y un enfriamiento extratropical en el océano Pacífico. En el Atlántico, la AMO está asociada con un incremento del OHC en latitudes medias. Sin embargo, es preciso destacar que las escalas de tiempo en que cada uno de los modos ejerce su influencia son significativamente distintas. Mientras que ENSO domina la variabilidad local del OHC a todas las escalas, tanto la PDO como la AMO producen impactos intermitentes en el OHC, en su mayor parte a escalas de tiempo multidecadales.

Los mecanismos e interacciones previamente descritos son característicos de las simulaciones analizadas y deben interpretarse dentro del marco de las limitaciones y particularidades del modelo ECHO-G. Por tanto, no se pueden establecer inferencias sobre las regiones, los mecanismos y las escalas de tiempo descritas hasta obtener evidencias adicionales de otros modelos y reconstrucciones paleoclimáticas. La representación de la dinámica oceánica y por extensión de la formación de agua profunda está constreñida por la limitada resolución del modelo, insuficiente para resolver la formación de *eddies*. El modelo infraestima variables como la intensidad del giro subpolar (∼15 Sv) o el rebosamiento a través de la dorsal de Groenlandia-Islandia-Escocia (0-3 Sv, ver Figuras 3.1 y 4.1), ambas claramente por debajo del rango de valores observados de 6 Sv (Olsen et al., 2008) y 25 a 40 Sv (Clarke, 1984; Reynaud et al., 1995; Bacon, 1997), respectivamente. Como consecuencia de los distintos procesos no resueltos, las escalas de tiempo típicas de los mecanismos descritos pueden estar sobreestimadas. De hecho, la propagación latitudinal de anomalías del *overturning* es significativamente más rápida en modelos que permiten la formación de *eddies* (Getzlaff et al., 2005). A pesar de todas las incertidumbres, los resultados descritos son físicamente consistentes, y por tanto ilustran procesos y mecanismos que potencialmente pueden ser importantes para la variabilidad oceánica.

Los impactos más importantes identificados en este estudio corresponden a la influencia de los gases de efecto invernadero. Con el comienzo de la era industrial la AMOC experimenta un debilitamiento progresivo, que supone una reducción de un 40% con respecto al promedio preindustrial al final de los escenarios de futuro. Este debilitamiento responde a una reducción de la evaporación y a un aumento de la precipitación en altas latitudes, ambas contribuyendo a su vez a

una disminución de la convección en el mar de Labrador. Esta estimación se encuentra dentro del rango de otras proyecciones de futuro con diferentes modelos climáticos (Schmittner et al., 2005; Schneider et al., 2007). Además, las simulaciones de futuro predicen un aumento del nivel del mar por expansión térmica de 0.14 a 0.17 m durante el siglo XXI. El resto de contribuciones (por fusión de glaciares y de la capa de hielo continental) no están representadas en el modelo. La comparación con observaciones del nivel del mar en los últimos 200 años sugiere que la expansión térmica simulada por el modelo representa un sexto del aumento total del nivel del mar. Si asumimos que esta relación se mantiene durante el siglo XXI, la suma de todas las contribuciones al nivel del mar total sería del orden de un metro, muy por encima de los valores predichos en el 4° informe de evaluación del Panel Intergubernamental sobre Cambio Climático (Meehl et al., 2007), pero en mejor acuerdo con los estudios más recientes (Rahmstorf, 2007; Pfeffer et al., 2008; Vermeer and Rahmstorf, 2009; Grinsted et al., 2010; Jevrejeva et al., 2010). Los procesos no representados por el modelo, como la fusión de hielo continental, pueden a su vez afectar a la representación de otras variables, como la intensidad de la AMOC. Por ejemplo, los cambios de agua dulce asociados a una fusión total o parcial de la capa de hielo de Groenlandia pueden potencialmente reducir la formación de agua profunda, y de esta forma acelerar el debilitamiento simulado de la AMOC para las próximas décadas.

Del resto de forzamientos, los volcanes tienden a mostrar un impacto mayor que los cambios en la actividad solar. Durante el periodo preindustrial, el forzamiento volcánico domina la respuesta radiativa global desde la escala interanual a la multidecadal (ver Figura 5.14). En comparación, la irradiancia solar muestra un impacto considerablemente menor. En las simulaciones con el modelo ECHO-G, la señal de enfriamiento asociada a los volcanes penetra paulatinamente en el océano, donde persiste durante al menos una decada (ver Figura 4.13). La integración de esta señal durante periodos de intenso volcanismo (e.g. 1150-1300 AD) produce cambios multidecadales de temperatura en la superficie del océano, afectando también al contenido de calor global. En las regiones de convección, este enfriamiento en superficie favorece la formación de agua profunda, llegando incluso a provocar una ligera intensificación de la célula de la AMOC (ver Figura 4.11-b). Esta respuesta dinámica no se observa para los cambios en la irradiancia solar.

En los análisis de la respuesta forzada (Capítulos 4 y 5) las fuentes principales de incertidumbre son las reconstrucciones consideradas, las metodologías aplicadas y la resolución del modelo. Las estimaciones más recientes han disminuido el rango de varibilidad solar desde el mínimo de Maunder hasta el presente en un

factor de 2 a 4 (Wang et al., 2005; Krivova et al., 2007; Tapping et al., 2007) en comparación con los valores usados para este estudio (Lean et al., 1995; Crowley, 2000). Para estas nuevas reconstrucciones, la respuesta global en temperaturas es significativamente menor, y por tanto los impactos en el OHC y la AMOC deberían también ser menores. Cabe también destacar que la señal volcánica se ha incluido como una modulación directa de la constante solar global, sin tener en cuenta la distribución latitudinal. Esta aproximación no es la más realista. Sin embargo, otros trabajos que analizan la respuesta del océano a erupciones de gran intensidad (e.g. Tambora, Pinatubo, Krakatoa) también identifican una señal de enfriamiento en profundidad, que persiste durante varias decadas (Gleckler et al., 2006a,b), y que, igual que en el modelo ECHO-G, puede llegar a tener un impacto significativo en la AMOC (Stenchikov et al., 2009). Finalmente, queda abierto el interrogante de hasta qué punto es realista la respuesta simulada de la AMOC al incremento de gases de efecto invernadero, teniendo en cuenta las incertidumbres en las emisiones futuras (Nakicenovic et al., 2000) y la complejidad de los mecanismos de *feedback* involucrados.

Publicaciones relacionadas con la Tesis en las que ha participado el autor

- Ortega, P., E. Hawkins and R. Sutton, 2011: Processes governing the predictability of the Atlantic Meridional Overturning Circulation in a coupled GCM. *Clim. Dyn.*, **37**, 1771-1782,, DOI: 10.1007/s00382-011-1025-1
- Ortega, P., M. Montoya, J. F. González-Rouco, J. Mignot and S. Legutke, 2011: Variability of the Atlantic meridional overturning circulation in the last millennium and two IPCC scenarios. *Clim. Dyn.*, Publicado online, DOI: 10.1007/s00382-011-1081-6
- Ortega, P., J. F. González-Rouco, M. Montoya and H. Beltrami, 2011: Variability of the ocean heat content during the last millennium. An assessment with the ECHO-g Model. En preparación.

1

Introduction

The ocean is a major component of the Earth's climate system, occupying over 71% of the total surface, and playing a crucial role in heat transport and storage as well as in climate variability. The ocean circulation is responsible for a large amount of the global freshwater and heat transport, and thus can have an important effect on climate at regional and global scales. Through internal dynamics and interactions with other components of the climate system the ocean generates variability from seasonal to decadal and longer timescales thus acting as a source of low-frequency variability (Hasselmann, 1976; Frankignoul and Hasselmann, 1977). Also, due to its high heat capacity (a thousand times larger than that of the atmosphere) about 84% of the total increase in heat content from 1955 to 1998 has been stored in the ocean (Levitus et al., 2005a).

In the present context of climate change, characterised by a net radiative imbalance (Hansen et al., 2005), the role of the ocean becomes of paramount importance since the global temperature response may be modulated by local changes in key quantities such as the Atlantic meridional overturning circulation (AMOC) or the ocean heat content (OHC). This chapter focuses specifically in three aspects that are relevant to provide a context for this thesis: first, the processes controlling AMOC variability, and the potential climate impacts (Section 1.1); second, the relevance of this variable for climate predictability (Section 1.2); and finally, the influence of ocean heat content in climate (Section 1.3).

1.1 Mechanisms of AMOC variability and their role in climate

The AMOC is a key factor for understanding the climate of the Northern Hemisphere by virtue of its role in the Earth's energy balance and its contribution to climate variability. Atlantic northward ocean heat transport peaks at about 1 PW (10^{15}W) in the northern tropics (e.g. Trenberth and Caron, 2001). A substantial amount of this heat is conveyed by the deep and intermediate overturning circulation (e.g. Talley, 2003), which thereby contributes to temper the climate in northwestern Europe.

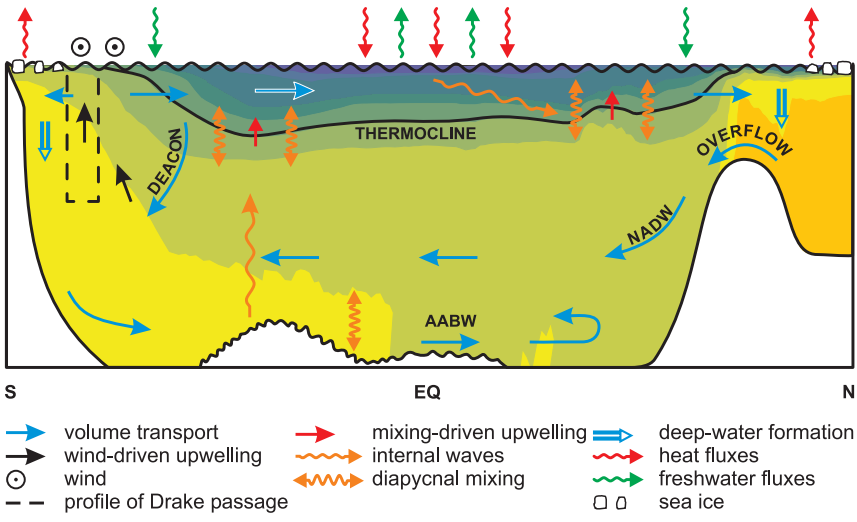

Fig. 1.1: Idealized latitudinal section of the zonally averaged Atlantic Meridional Overturning Circulation (Figure from: Kuhlbrodt et al., 2007).

An schematic picture of the zonally-averaged AMOC is illustrated in Figure 1.1. The AMOC strength is controlled by deep water formation (DWF) in the North Atlantic, which accounts for the contribution of deep convection in the Labrador and Irminger Seas (Marshall and Schott, 1999; Pickart et al., 2003), and an overflow of dense waters through the Greenland-Scottland ridge, driven by convection in the Nordic Seas (Hansen and Østerhus, 2000). North Atlantic Deep Water (NADW; Figure 1.1) moves southward in depth, reaching the Southern

Ocean where it upwells through the combined effect of wind-driven Ekman forcing and diapycnal mixing (Kuhlbrodt et al., 2007). The overturning cell is closed by surface ocean currents along the western Atlantic boundary, transporting warm and salty waters all the way from the Equator to the NADW regions, where they cool and densify, thus helping to maintain North Atlantic convection. A similar overturning cell formed by Antarctic Bottom Waters (AABW) and driven by deep convection in the Ross and Weddell seas spreads near the bottom below the NADW cell. In the other basins, no deep water formation takes places and ocean currents are mostly wind-driven. The idealized diagram of the large-scale ocean circulation, usually called as the ocean 'conveyor belt' (Broecker, 1987), is shown in Figure 1.2.

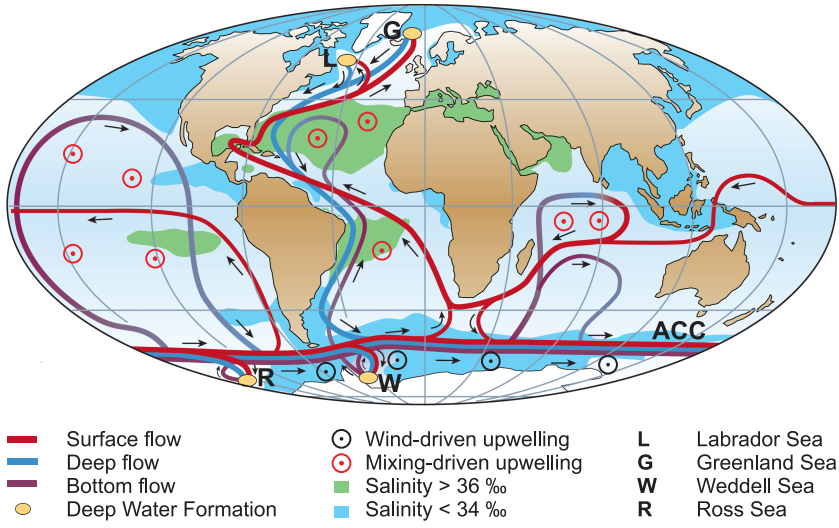

Fig. 1.2: Simplified scheme of the global-scale ocean circulation. Surface ocean currents are represented in red, deep flows in light blue, and bottom flows in dark blue lines. Deep water formation regions are represented by the yellow spots (Figure from: Kuhlbrodt et al., 2007).

Through its interaction with the atmosphere, the AMOC has been shown to account for a significant part of surface climate variability on interannual and, to a larger extent, on decadal and multidecadal time scales. A number of

studies suggest an active role of the AMOC in shaping Atlantic and Pacific multidecadal variability (Delworth and Mann, 2000; Kerr, 2000; Wu and Gordon, 2002; Sutton and Hodson, 2003; Dong et al., 2006). The AMOC is thought to be linked to the Atlantic multidecadal oscillation (AMO; Kushnir, 1994; Delworth and Mann, 2000; Kerr, 2000; Knight et al., 2005), which has in turn been related to widespread regional multidecadal variability, like Atlantic hurricane activity, summer temperature and precipitation anomalies across Europe and North America, or droughts in the Sahel (Sutton and Hodson, 2005; Knight et al., 2006; Zhang and Delworth, 2006, 2007). Furthermore, climate model studies suggest that Atlantic sea surface temperatures (SSTs) are linked to decadal and interdecadal variations of the North Atlantic Oscillation (NAO; Wu and Gordon, 2002; Sutton and Hodson, 2003), and contribute as well to a multidecadal modulation of El Niño-Southern Oscillation (ENSO) variance (Dong et al., 2006). Likewise, Timmermann et al. (2007) and Dong and Sutton (2007) report enhanced ENSO interannual variability and stronger asymmetry between El Niño and La Niña events as a response to a weakening in the AMOC strength.

Given the evidence that the AMOC may contribute to climate variability at multiple time scales, there is increasing interest in understanding the origins of its own variability and investigating its possible response to climate change conditions. Natural AMOC variability has been widely studied through the use of control simulations under current climate conditions performed with atmosphere-ocean general circulation models (AOGCMs; Delworth et al., 1993; Timmermann et al., 1998; Delworth and Greatbatch, 2000; Vellinga and Wu, 2004; Latif et al., 2004; Dong and Sutton, 2005; Knight et al., 2005; Jungclaus et al., 2005; Mignot and Frankignoul, 2005; Hawkins and Sutton, 2007). These studies have led to the identification of several modes of ocean variability operating from interannual to centennial time scales. AMOC interannual variability is found to be mainly dominated by surface wind-stress variations, through changes in both the Ekman transport and the vertical shear of the meridional flow (Eden and Willebrand, 2001; Vellinga and Wu, 2004; Mignot and Frankignoul, 2005; Hirschi et al., 2007; Cabanes et al., 2008). These wind variations are in turn related to modes of climate variability such as NAO and ENSO. In contrast, interdecadal to centennial variability in the AMOC is characterised by a delayed response of the overturning, usually forced by near surface density anomalies in the NADW formation regions (e.g. Delworth et al., 1993; Timmermann et al., 1998; Delworth et al., 2002; Dong and Sutton, 2005). The origin of these anomalies differs from one model to another, also producing differences in the dominant time scales of AMOC variability. For instance, Delworth et al. (1993) presented a 50-yr damped oscillation in a 600-yr control simulation with the GFDL model, in which a weakening of the AMOC was found to lead to lower temperatures in the subpolar North Atlantic,

thereby enhancing density in the region and leading to a strengthening of the subpolar gyre. The strengthened subpolar gyre contributed in turn to increase the transport of salinity anomalies to the convection region, thus establishing a mechanism for phase reversal. This mechanism was later found as well by Dong and Sutton (2005) in a 1000-yr control run with the HadCM3 model, albeit with a shorter time scale (25 yr). A complementary analysis with an extended 1600 yr long version of the same HadCM3 control run was performed by Vellinga and Wu (2004) to identify centennial oscillations. They found a secular mode in which variations in the AMOC strength led to shifts in the Intertropical Convergence Zone (ITCZ) location and thereby to the formation of tropical salinity anomalies. These anomalies were subsequently advected to the North Atlantic, causing a lagged response of the AMOC that contributed to restore the initial ITCZ position. A different multidecadal mechanism has been observed in the same HadCM3 control run (Hawkins and Sutton, 2007) as well as in a 500 yr control simulation with the ECHAM5/MPI-OM model (Jungclaus et al., 2005). Both simulations identify an internal mode with overturning variability driven by freshwater discharges from the Artic Ocean that modulate the convective activity in the deep water formation regions. In the HadCM3 model, convection happens most actively in the Nordic Seas region and generates overturning variability in a range of time scales, from multidecadal to centennial. In the ECHAM5/MPI-OM simulation most deep convection variability takes place near the Labrador Sea, where the freshwater export from the Arctic leads to a fluctuation of 70-80 years. Moreover, Guemas and Salas-Mélia (2008) have analysed a 400 yr long preindustrial control simulation with the CNRM-CM3 model, where the overturning strength also responds to North Atlantic convective forcing on time scales of 5 to 10 years. They find that convection variability is controlled by the NAO in the Labrador Sea, and is favoured by intensified northerly winds in the Greenland-Iceland-Norwegian (GIN) and Irminger Seas.

Interestingly, modes of interdecadal AMOC variability can be also observed in simple, idealized models (e.g. Weaver and Sarachik, 1991; Saravanan and McWilliams, 1997; Colin de Verdière and Huck, 1999; Te Raa and Dijkstra, 2002). For example, Colin de Verdière and Huck (1999) and Te Raa and Dijkstra (2002) describe an oscillation mechanism based on an interplay between zonal and meridional temperature gradients that produce in turn meridional and zonal overturning responses. A recent attempt to reconcile mechanisms from models with evidence from observations is made in Frankcombe et al. (2010). They compare several observational datasets and a long control simulation performed with the GFDL CM2.1 model and identify two predominant modes of North Atlantic multidecadal variability, operating at 20-30 and 50-70 years, respectively. The

first mode is related to internal AMOC variability and is characterised by westward propagation of subsurface anomalies, similar to that already described by Colin de Verdière and Huck (1999) and Te Raa and Dijkstra (2002). The second mode is mainly related to both interdecadal atmospheric forcing and ocean exchange processes from the Arctic to the Atlantic, with a major role of salinity. However, given the short time span of the observational datasets, their work could only identify a few climate cycles. Further insight into the processes responsible for AMOC multidecadal variability is important for the assessment of decadal predictability and also for discriminating anthropogenic climate change from natural climate variability in the next decades (Dong and Sutton, 2005; Keenlyside et al., 2008).

A most relevant context for the assessment of current and future climate change is the last millennium, which encompasses a range of natural variability compatible with the current natural external forcing conditions. This is the period with more climate reconstructions (e.g. Briffa et al., 1998; Jones et al., 1998; Mann et al., 1999; Crowley and Lowery, 2000; Esper et al., 2002) and simulations (e.g. González-Rouco et al., 2003b; Stendel et al., 2006; Tett et al., 2007; Swingedouw et al., 2010), and better resolved estimates of the forcing factors (e.g. Lean et al., 1995; Etheridge et al., 1996; Bard et al., 2000; Crowley, 2000). Nevertheless, studies addressing externally forced AMOC variability within this period are scarce (e.g. Hofer et al., 2011; Swingedouw et al., 2010). Better known is the AMOC response to increasing greenhouse gas (GHG) concentrations in the context of future climate change simulations (Cubasch et al., 2001; Thorpe et al., 2001; Gregory et al., 2005; Schmittner et al., 2005; Meehl et al., 2007; Drijfhout and Hazeleger, 2007; Drijfhout et al., 2008). According to most simulations (Cubasch et al., 2001; Meehl et al., 2007), temperature and precipitation are expected to increase at high-latitudes of the Northern Hemisphere throughout the 21^{st} century, both likely contributing to a weakening of the AMOC. In fact, all the experiments including an increase of anthropogenic emissions support this weakening, although none of them simulates a complete collapse by the end of the current century (Gregory et al., 2005; Schmittner et al., 2005; Meehl et al., 2007). Another feature observed in some future scenario projections is a shallowing of the overturning cell that is simultaneous to a northward shift of DWF regions (Drijfhout et al., 2008).

Yet, the influence of natural forcing factors (e.g. volcanic aerosols and solar irradiance) on AMOC variability remains unclear (Zorita et al., 2004; Stendel et al., 2006; Stenchikov et al., 2009; Swingedouw et al., 2010; Ottera et al., 2010). A better understanding of such potential impacts is important, since these could

modulate the AMOC response to the GHG forcing. Also, an assessment of past AMOC variability throughout the last millennium would allow to place the future projections in a broader temporal context, thus helping to identify unprecedented AMOC trends.

1.2 Relevance of AMOC for climate predictability

A slowdown of NADW formation in the next few decades could have climatic impacts worldwide (e.g. Vellinga and Wood, 2002; Levermann et al., 2005). Hence the importance of developing successful decadal climate predictions. Predictive skill arises from a good representation of natural variability, especially in the ocean, as well as from a realistic climate response to external radiative forcings (Meehl et al., 2009). The skill of predictions also relies on a proper model initialization, that requires in turn optimal estimates of the current observed state of the atmosphere, oceans, cryosphere, and land surface. For example, recent advances in ocean initialization have led to improved decadal predictive skill globally, and more particularly in the North Atlantic region (Smith et al., 2007; Keenlyside et al., 2008; Pohlmann et al., 2009; Meehl et al., 2009), through a more accurate representation of the initial state (in phase and magnitude) of key processes of internal variability, such as the subpolar gyre dynamics, or the Atlantic meridional overturning circulation (Keenlyside et al., 2008).

A rapid AMOC weakening, either as a response to anthropogenic forcings or because of a natural fluctuation, would have major impacts on regional and global climate (e.g. Hall and Stouffer, 2001; Hawkins and Sutton, 2008). This highlights the necessity of establishing a continuous monitoring of the AMOC intensity, and perhaps more importantly, of assessing which key regions and variables can lead to skillful predictability of its variability. Such successful predictions become crucial since they would allow longer response time for the development and application of mitigation and adaptation strategies. Recent efforts from the transoceanic Rapid Climate Change (RAPID) array have produced continuous in-situ measurements of AMOC intensity and its different components at 26.5°N since March 2004 (Cunningham et al., 2007; Kanzow et al., 2007, 2010). Although this is an important step, a longer observational database is still required for the identification of possible future trends and for the validation of simulated mechanisms of low frequency AMOC variability.

Concurrently, a growing body of studies with general circulation models (GCMs) has been devoted to the identification of ocean quantities with long observational records available that could lead to potential AMOC predictability.

For example, Latif et al. (2004) find a close correspondence between multidecadal North Atlantic SST fluctuations and the AMOC intensity. Other models also find a link between the AMO, a coherent pattern of multidecadal surface temperature variability in the North Atlantic, and the AMOC (Knight et al., 2005; Zhang and Delworth, 2006; Msadek and Frankignoul, 2009). This index is therefore a first candidate to monitor the variability of the AMOC. However, it is also influenced by changes in solar irradiation and high-frequency atmospheric forcing that might be unrelated to the AMOC (Msadek et al., 2010). Other alternative AMOC fingerprints have been also identified. In the GFDL CM2.1 model, the leading modes of upper ocean heat content, sea surface height and subsurface temperature in the North Atlantic are also related to AMOC variability (Zhang, 2008) and have potential predictability for lead times of 10 to 20 years (Msadek et al., 2010). Likewise, as previously illustrated in Section 1.1, other studies highlight the key role of the subpolar North Atlantic, and in particular of the Labrador and Irminger Seas in driving deep water formation and therefore the AMOC (e.g. Delworth et al., 1993; Timmermann et al., 1998). Finally, other forerunners for the rapid AMOC fluctuations are identified by Hawkins and Sutton (2008) for the HadCM3 model. These consist of rapid changes in both temperature and salinity in the Nordic Seas, as well as in the density of the water flowing through the Denmark Strait, all preceding rapid AMOC variations by about 10 years.

Overall, evidence from previous studies is far from conclusive. There is a need for improving our understanding of the processes controlling DWF by extending similar analyses to other models and simulations, aiming both to the identification of new potential predictors (e.g. by quantifying the contribution of local atmospheric heat fluxes over the main convection regions), and to evaluate their role during the large rapid AMOC fluctuations.

1.3 The role of ocean heat content on climate

Recent studies suggest that predictability beyond seasonal timescales may result from persistence of large-scale OHC anomalies, associated to regions like the North Atlantic and the Southern Ocean, or to mechanisms related to ENSO dynamics (Hermanson and Sutton, 2009, 2010). Monitoring the present OHC changes is also important for other reasons. Since the ocean is the main reservoir for the heat gain, the recent OHC increase is an important indicator of the Earth's radiative imbalance, and therefore of anthropogenic impact on the ocean (Levitus et al., 2001). Besides, ocean heat uptake can temporarily mitigate the transient surface temperature rise, and thus produce a delayed climate impact on decadal to centennial timescales. Also, the recent ocean warming has a direct

influence on sea-level rise, this being probably one of the most important impacts of climate change over the coming century (Grinsted et al., 2010). Other processes, such as deep water formation, or the rate of ice sheet disintegration (Hansen et al., 2005) are also sensitive to ocean heat content changes. As a final example, progress in hurricane prediction also leans on a correct representation of the spatial distribution of the heat content changes (Mainelli et al., 2008).

The balance of evidence from both proxy reconstructions of past sea level changes (Tanner, 1992; Van De Plassche et al., 1998; Jevrejeva et al., 2009; Grinsted et al., 2010), as well as from energy balance models (EBMs; Crowley et al., 2003) and intermediate complexity climate models (Sedláček and Mysak, 2009a) suggests that the recent ocean warming might be unprecedented for at least the last millennium. In the 20^{th} century, the rise in ocean heat content is mostly explained by the warming following the increase in greenhouse gases (e.g. Crowley et al., 2003; Gregory et al., 2004; Delworth et al., 2005), which is partially offset by the cooling effect of both anthropogenic and volcanic aerosols, the latter mitigating the warming signal in a factor from one third (Stenchikov et al., 2009) to one half (Delworth et al., 2005). In the observational period, models generally reproduce realistic warming trends, but tend to underestimate the observed decadal changes of OHC (Levitus et al., 2001; Barnett et al., 2001; Sun and Hansen, 2003; Gregory et al., 2004; Barnett et al., 2005; Church et al., 2005; Delworth et al., 2005). However, recent results suggest that observed OHC interdecadal variability is likely inflated due to the effect of sampling (Gregory et al., 2004) and bias correction methods (Levitus et al., 2009). More recent and reliable observations (Domingues et al., 2008; Ishii and Kimoto, 2009; Levitus et al., 2009) have comparatively smaller interdecadal OHC variability, this being mostly related to the cooling effect of volcanic forcing. Also important is the contribution of natural climate variability to the global OHC changes. For instance, Levitus et al. (2005b) argue that interdecadal variability in the global OHC records may result from the shift in polarity of the Pacific Decadal Oscillation (PDO) during the late-1970s. A different modulation is discussed in Willis et al. (2004). They find evidence that ENSO-related variability can be large enough to affect the global OHC changes on interannual timescales. Such contributions from internal climate variability can modulate the GHG-driven warming signal on future climate change projections. This is important since other relevant influences, such as the solar and volcanic forcing, are unpredictable and thereby cannot be included.

Such assessments of natural OHC variability are based on observations, being therefore only representative of the last 50 years. Again, as for the interpretation of the AMOC trends, a broader time perspective is desirable. Extending the pre-

vious analysis to the context of the last millennium, for instance by studying long forced simulations, is interesting for two particular reasons. First, the influence of internal modes of climate variability on the OHC can be assessed within a longer time period, thus allowing for a quantification of their associated global and local impacts at longer timescales (multidecadal to secular). And second, further insight into the influence of external forcings can be achieved in such extended time interval that incorporates more volcanic eruptions and larger insolation changes, such as the transition from the Medieval Climate Anomaly (MCA) to the Little Ice Age (LIA).

1.4 Main objectives and structure of the text

This work sits on the previous context and attempts to shed light on the main aspects of ocean variability and predictability throughout the period 1000 to 2100 AD. To this end, we make use of six different experiments performed with the ECHO-G AOGCM, namely two 1000 yr long control runs, two forced simulations of the last millennium, and two climate change runs using 21^{st} century scenarios of the Intergovernmental Panel on Climate Change (IPCC). The model and the experimental procedure are described in detail in Chapter 2. We will focus on two main ocean quantities with relevance for climate variability and predictability: first, the variations in the Atlantic meridional overturning circulation, and second, the changes in the ocean heat content. The analysis will be structured in three different but complementary parts, each addressing specific questions.

A first analysis, starting in Chapter 3, will investigate the main regions and processes contributing to deep water formation and, therefore, AMOC variability in the model. For this analysis, a present-climate long control simulation will be employed. In this way, the sources of natural internal AMOC variability, unrelated to external forcing factors, can be identified. Particular emphasis will be given to the potential contributions of the stochastic forcing from the atmosphere, and other non-local processes. The final aim will be to identify new potential predictors, and use them to develop a predictive regression model of the AMOC strength. This regression model will be tested during the large rapid decadal overturning changes (both increases and decreases), and their potential climate impacts will be evaluated.

A complementary study focused on the externally forced AMOC variability will be developed in Chapter 4, based on the analysis of two forced simulations of the last millennium and two IPCC scenario runs for the 21^{st} century. A new control simulation, compatible with the previous forced runs, will be used as well. This suite of experiments allows for a direct comparison between the main aspects

of forced and unforced AMOC variability. Two main objectives will deserve further attention. First, a comparison between the leading mechanisms of AMOC variability at interannual and longer time-scales, with special emphasis on the differences introduced by the external forcing. And second, a specific account of the AMOC response to each of the forcing factors.

Forced and unforced variability of ocean heat content during the period 1000 to 2100 AD will be analysed in Chapter 5. In this study, the importance of the initial conditions to produce realistic OHC estimates (which are in turn relevant for climate predictability) will become evident. Therefore, in a first step, the reliability of the simulations will be validated against previous evidence of past OHC variability (i.e. observations and proxy reconstructions). Likewise, the natural forced and unforced contributions to global and local OHC variability will be evaluated in an attempt to shed light on the processes that can potentially modulate or even mitigate the recent upper warming of the world oceans (Levitus et al., 2000). These contributions will be obtained and compared both for observations and simulations. This step is also important, since OHC observations are only available for the last 50 years, and different impacts could appear when extending the analysis to longer timescales.

A final account of the main conclusions, including a discussion on the open questions, and possible lines for future research is developed in Chapter 6.

2

Model and experiments

This chapter contains a description of the climate model and simulations that have been used in the work. Section 2.1 characterises the model components, and discusses the flux correction methodology. Section 2.2 introduces the experimental procedure and the forcing factors considered, making emphasis on the differences between simulations, and placing them within the framework of similar model experiments.

2.1 Model description

The analysis of OHC and AMOC variability in this work leans on the use of several control and externally forced climate simulations performed with the ECHO-G AOGCM. The ECHO-G model (Legutke and Voss, 1999) consists of the spectral atmospheric model ECHAM4 (Roeckner et al., 1996) and the ocean model HOPE-G (Wolff et al., 1997). Its atmospheric component is set up with a T30 horizontal resolution (ca. $3.75° \times 3.75°$) and 19 vertical levels extending up to 10 hPa, with five of them located above 100 hPa. The horizontal resolution of the ocean model is about $2.8° \times 2.8°$, with an enhancement of the meridional resolution in the Tropics and towards the Equator, where it reaches a minimum grid point separation of 0.5°. This refinement in resolution is intended to provide a more realistic representation of equatorial and tropical ocean currents. Vertical discretisation of the ocean incorporates 20 variably spaced levels, 14 of which are located in the upper 1000 m. To avoid climate drift, the ocean component includes both heat and freshwater flux adjustments. The same corrections are applied to all experiments analysed in this study. They are diagnosed as annual mean values from the relaxation terms during the last 100 years of a coupled spin-up phase which preceded the control experiment. In that spin-up phase, SST was

relaxed to monthly climatological values calculated from the Atmospheric Model Intercomparison Project (AMIP) data for 1979-1994 (Gates, 1992) assuming a relaxation constant of 40 W/m^{2}K. Sea surface salinity is relaxed to seasonal climatological values (Levitus et al., 1994) on a time scale of 30 days. No salinity relaxation is applied in the climatological sea-ice regions as diagnosed from the AMIP SST to avoid distortion of the upper salinity changes related with sea-ice production. Both flux fields are normalized to vanish globally. With this flux correction method the wind-stress, which plays an important role in the mechanisms described in this study (Chapters 3 and 4), is determined by the model. These adjustments are a drawback if ECHO-G is compared to other simulations that do not use flux corrections (e.g. Vellinga and Wu, 2004; Jungclaus et al., 2005) since their need is an indication of erroneous feedbacks in the transient climate (Marotzke and Stone, 1995). The degree to which they may affect the results shown herein is not known. However, large impacts are not expected since the mechanisms that will be described are comparable in physics and time scales to those of other simulations without flux corrections.

2.2 Experimental set up

This study makes use of six different simulations: two 1000-yr control simulations (CTRL1 and CTRL2, hereafter), two forced simulations for the period 1000 to 1990 AD (FOR1 and FOR2, hereafter), and two future scenario simulations (A2 and B2, hereafter) that extend FOR1 until 2100 AD.

Both CTRL1 (Zorita et al., 2003) and CTRL2 (Ortega et al., 2011c) use identical external forcing fixed to present day values ([CO_2]=353 ppm; [CH_4]=1,720 ppb; [N_2O]=310 ppb; solar constant = 1.365 Wm^{-2}). The main difference is that CTRL1 was run in an earlier version of the ECHO-G model to that employed for the other five simulations. CTRL1 was run in a Cray C90 system using an atmospheric component written in f77, whereas the rest of experiments were made in a NEC SX-6 machine with a most recent version of the atmospheric model coded in f90. Although, in principle, both model versions are thought to be equivalent, some minor changes in the code cannot be discarded, in view of some clear differences in the climatological values of the main atmospheric and oceanic variables in CTRL1 and CTRL2. A clear example is illustrated by the global SST mean values (Figure 2.1). While temperature variability in CTRL1 remains stable around 18°C throughout the whole simulation, CTRL2, that starts from year 305 in CTRL1, shows an initial warming trend that stabilises about one century after, indicating that both runs have somewhat different equilibrium states. Other important changes between both forced runs concern the convection regions and

the AMOC cell and will be discussed in the final conclusions. CTRL1 will be employed in a first assessment of AMOC predictability in the ECHO-G model (Chapter 3). Likewise, CTRL2 will be used as a reference control simulation to compare with the forced experiments in the analyses of AMOC (Chapter 4) and OHC (Chapter 5) variability during the last millennium, since it is run under the same model version than the forced experiments, and provides their initial conditions.

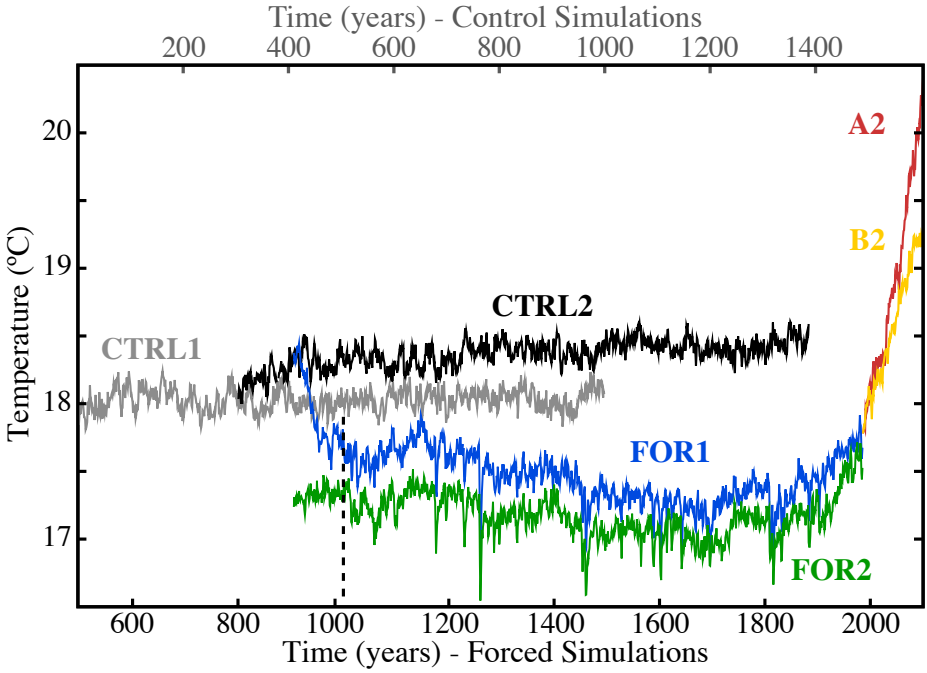

Fig. 2.1: Evolution of the global SST mean (in °C) in the whole suite of ECHO-G simulations. CTRL2 and CTRL1 are displayed so that their dates match the starting conditions taken for FOR1 and CTRL2, respectively. All the forced simulations are set to match the corresponding historical years (represented in the bottom axis). The vertical dashed line separates the forced millennial simulations from their corresponding spin down periods.

The forced simulations of the past millennium (FOR1 and FOR2, González-Rouco et al., 2003b, 2006) use identical estimates of natural and anthropogenic forcing factors: solar irradiance, the radiative effects of stratospheric volcanic

aerosols, and concentrations of greenhouse gases (CO_2, CH_4 and N_20) based on reconstructions provided by Crowley (2000). Figure 2.2 shows the time evolution of all these forcing factors. In particular, the representation of the volcanic forcing is rather simplified, with the effect of volcanic aerosols incorporated as global variations in the effective solar constant. Changes in tropospheric sulphate aerosols and vegetation, both of which are likely to attenuate the warming trends in the 20^{th} and 21^{st} centuries (Bauer et al., 2003; Osborn et al., 2006) are not included. Within the climate change scenarios net solar irradiance is kept constant and fixed to the value of year 1990, and GHG concentrations vary according to the IPCC emission scenarios A2 and B2 (Nakicenovic et al., 2000).

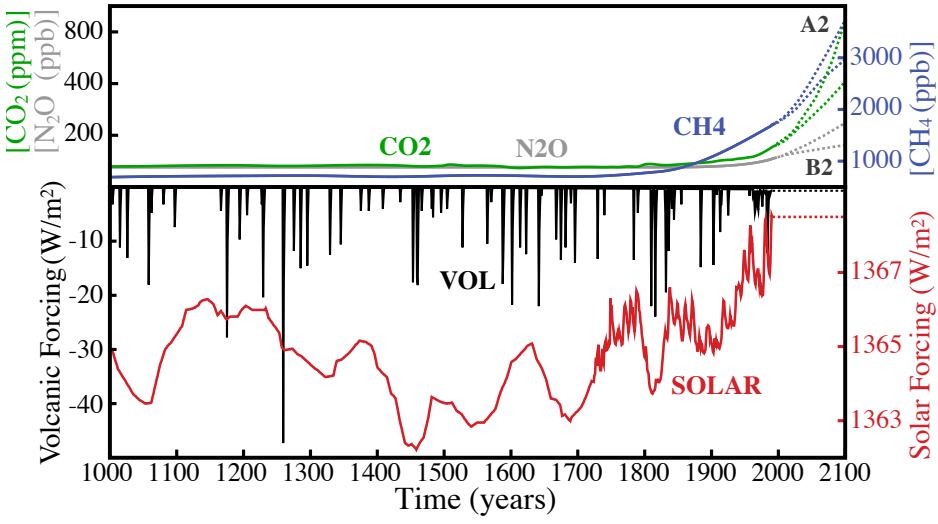

Fig. 2.2: Estimations of natural and anthropogenic forcing factors used to drive the ECHO-G model: solar irradiance (red line), greenhouse gas concentrations (green, grey and blue lines for CO_2, N_2O and CH_4 respectively), and the radiative effect of volcanic aerosols (black lines). Dotted lines represent the forcing in the future climate scenario runs. Figure modified from González-Rouco et al. (2009).

The two long forced simulations start from different initial conditions. FOR1 (blue line in Figure 2.1) is initiated from year 100 in CTRL2 and FOR2 from year 1700 AD in FOR1. In both forced runs a spin down period of 100 years was allowed to drive the model to equilibrium with the forcing conditions of year 1000 AD. The initial state was comparatively warm in FOR1 and the spin down

period proved to be too short to reach at least equilibrium in surface temperatures (Goosse et al., 2005; Osborn et al., 2006). In turn, FOR2 was started from a colder state (green line in Figure 2.1) and its temperature variability was found to be well within the range of other millennial simulations (Jansen et al., 2007; Zorita et al., 2007). Both FOR1, and to a lesser degree, FOR2, exhibit initial trends in the deep ocean (not shown), indicating that it requires some time to reach thermal adjustment. Some initial thermal imbalance is also present in CTRL1 and CTRL2. For that reason, the first two centuries of each simulation, which incorporate the largest drifts, are generally not considered in this study.

A more detailed description of the model setup, the forcing and the simulations can be found in González-Rouco et al. (2009). Internal climate variability has been validated against instrumental data in CTRL1 (Min et al., 2005a,b). Many features of the long forced simulations employed in our study have been analysed in previous works (González-Rouco et al., 2003a,b, 2006, 2009; von Storch et al., 2004; Zorita et al., 2003, 2005; Beltrami et al., 2006; Gouirand et al., 2007a,b; Stevens et al., 2007).

FOR1 and FOR2 were the first AOGCM simulations covering the last one thousand years (González-Rouco et al., 2003b). Since then, additional simulations covering the last millennium or parts of it with new state-of-the-art models have become available (Stendel et al., 2006; Tett et al., 2007; Ammann et al., 2007; Servonnat et al., 2010; Swingedouw et al., 2010; Jungclaus et al., 2010; Hofer et al., 2011), thanks to the combined effort of different groups and institutions. A first inter-model comparison, including the ECHO-G runs, as well as other millennial simulations with the NCAR-CSM1.4 (Ammann et al., 2007), CCSM3 (Hofer et al., 2011), IPSLCM4_v2 (Servonnat et al., 2010), CNRM-CM3.3 (Swingedouw et al., 2010) and MPI-ESM (Jungclaus et al., 2010) coupled models is performed by González-Rouco et al. (2011), highlighting some discrepancies in the representation of the transition from the Medieval Climate anomaly to the Little Ice Age. In these studies, most of the emphasis has been placed on the atmospheric radiative response to the forcing, with lesser interest on ocean variability. Only Swingedouw et al. (2010) and Hofer et al. (2011) investigate to some extent the impact of the forcing on the AMOC strength. Swingedouw et al. (2010) identify some NAO delayed response to changes in solar irradiation, producing also a weakening of the AMOC strength with a lead time of 10 years. In contrast, (Hofer et al., 2011) find that changes in their radiative forcing are too small to produce a direct AMOC response in the last millennium. This work provides further insight about simulated ocean variability within the last millennium in the ECHO-G simulations.

3

Predictability of deep water formation in the North Atlantic *

In our mind's eye we can almost see it whole, the round-the-world journey that seawater takes. We can imagine taking the trip ourselves.

It begins north of Iceland, a hundred miles off the coast of Greenland, say, and on a black winter's night. The west wind has been screaming off the ice cap for days now, driving us to ferocious foaming breakers, sucking every last ounce of heat from us, stealing it for Scandinavia. We are freezing now and spent, and burdened by the only memory we still have of our northward passage through the tropics: a heavy load of salt. It weights on us now, tempts us to give up, as the harsh cold itself does. Finally comes that night when, so dense and cold we are almost ready to flash into ice, we can no longer resist: we start to sink. Slowly at first, but with gathering speed as more of us join in, and as it becomes clear that there is nothing to catch us - no water underneath that is denser than us. We fall freely through the tranquil dark until we hit bottom, more than a mile and a half down...

Robert Kunzig. Mapping the deep. 2000.

The importance of the AMOC for climate highlights the need for research to better understand the processes that govern its variability and predictability. Previous research has established that the AMOC responds to variations in the

* The main contents of this chapter are included in:
Ortega, P., E. Hawkins and R. Sutton, 2011: Processes governing the predictability of the Atlantic Meridional Overturning Circulation in a coupled GCM. *Clim. Dyn.*, **37, 1771-1782,** DOI: 10.1007/s00382-011-1025-1

formation of dense waters in the subpolar North Atlantic (e.g. Delworth et al., 1993; Timmermann et al., 1998). Deep water formation itself is subject to both local and non-local influences. Local influences are associated particularly with variations in the air-sea fluxes that modulate deep convection. Non-local influences may arise through advection or wave propagation in the ocean. Lateral mixing processes may give rise to interactions between local and non-local influences. The predictability of AMOC variations depends, in substantial part, on the relative importance of these different influences, and on the detailed nature of each of them. The first aim of this chapter is to elucidate the roles of local stochastic forcing and other potential processes in governing AMOC variability and predictability in the ECHO-G model.

The variability of air-sea fluxes on interannual and longer timescales is often assumed to be stochastic (Griffies and Tziperman, 1995; Saravanan and McWilliams, 1997; Kravtsov and Ghil, 2004; Monahan et al., 2008) and hence unpredictable. However, its influence on deep water formation is not instantaneous (e.g. Delworth and Greatbatch, 2000; Eden and Willebrand, 2001). The ocean has significant memory, and consequently integrates the fluctuations over a period of time (e.g. Hasselmann, 1976; Frankignoul and Hasselmann, 1977). Less clear, for a particular application, is the time period over which this integration occurs. In the case of deep water formation in the North Atlantic, the effective time period is an important matter, because it may determine the predictability of AMOC fluctuations. Consequently, a second aim of this study is to investigate the extent to which the AMOC integrates in time the influence of air-sea fluxes, and the consequences for AMOC predictability.

This analysis is performed with a control 1000 year long simulation performed with the ECHO-G model (CTRL1; see Chapter 2). First, the processes governing decadal AMOC variability in the model are explored (Section 3.1) and, based on the results, a predictive regression model is developed (Section 3.2). Section 3.3 evaluates the model's performance in the representation of large decadal AMOC increases and decreases, which may have major impacts on regional and global climate (e.g. Hall and Stouffer, 2001; Hawkins and Sutton, 2008). Indeed, this section also explores the respective climate fingerprints and particular conditions of such events in the ECHO-G model. Finally, the main results and conclusions of this chapter are summarised in Section 3.4.

3.1 Climatology and temporal variability

We now consider the relevant aspects of the AMOC, as represented by the ECHO-G model. Figure 3.1 shows the mean AMOC streamfunction, which has a typical spatial structure, but the maximum overturning strength is found further north

than in some other GCMs (e.g. Timmermann et al., 1998; Jungclaus et al., 2005; Dong and Sutton, 2005). A meridional overturning index (MOI) is defined locally at 47.4° N and 1050 m to represent the AMOC temporal variability near its climatological maximum. The long-term mean of the MOI is 16.5 Sv, with a standard deviation of 1.8 Sv. For the following analysis the MOI has been detrended and normalised. Figure 3.2a shows that MOI fluctuations tend to occur at decadal to interdecadal timescales, suggesting potential predictability. Indeed, the corresponding power spectrum (Figure 3.2b) gives evidence of significant MOI variability other than pure red noise at both interannual (periods from 2 to 5 years) and interdecadal timescales. In Figure 3.3 a Hovmoller diagram (latitude vs time) shows the variability of the integrated ocean transport down to 1050 m, and highlights the different temporal scales of variability at different latitudes. It is clear that variability is predominantly decadal at midlatitudes, whereas the tropics are more noisy and therefore interannual variability is more prominent (similar to the HadCM3 GCM; Bingham et al., 2007). A slight tilt of the anomalies is visible in the latitude belt around 40-45°, indicating a localised slow-down in the southward propagation.

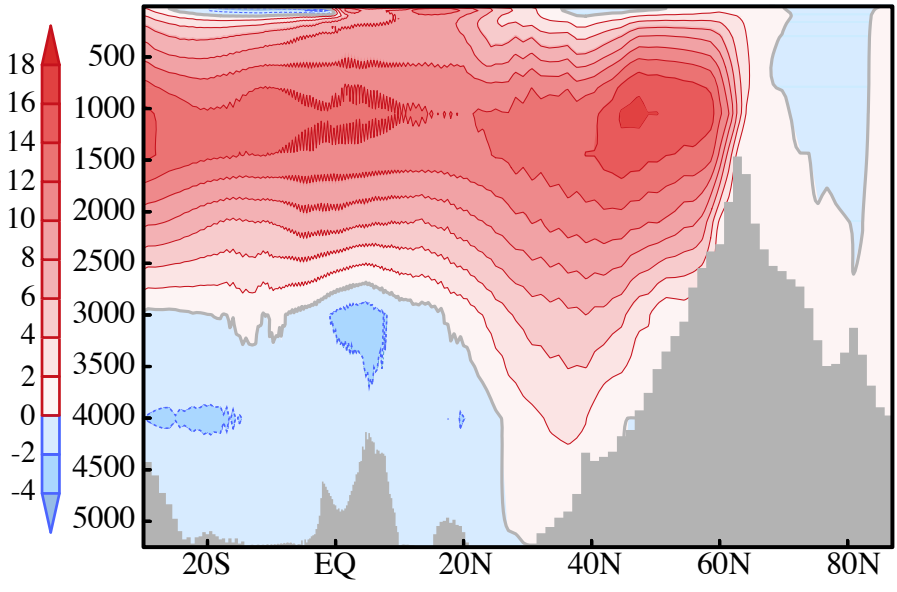

Fig. 3.1: Long-term mean climatology of the Atlantic meridional overturning streamfunction (in Sv).

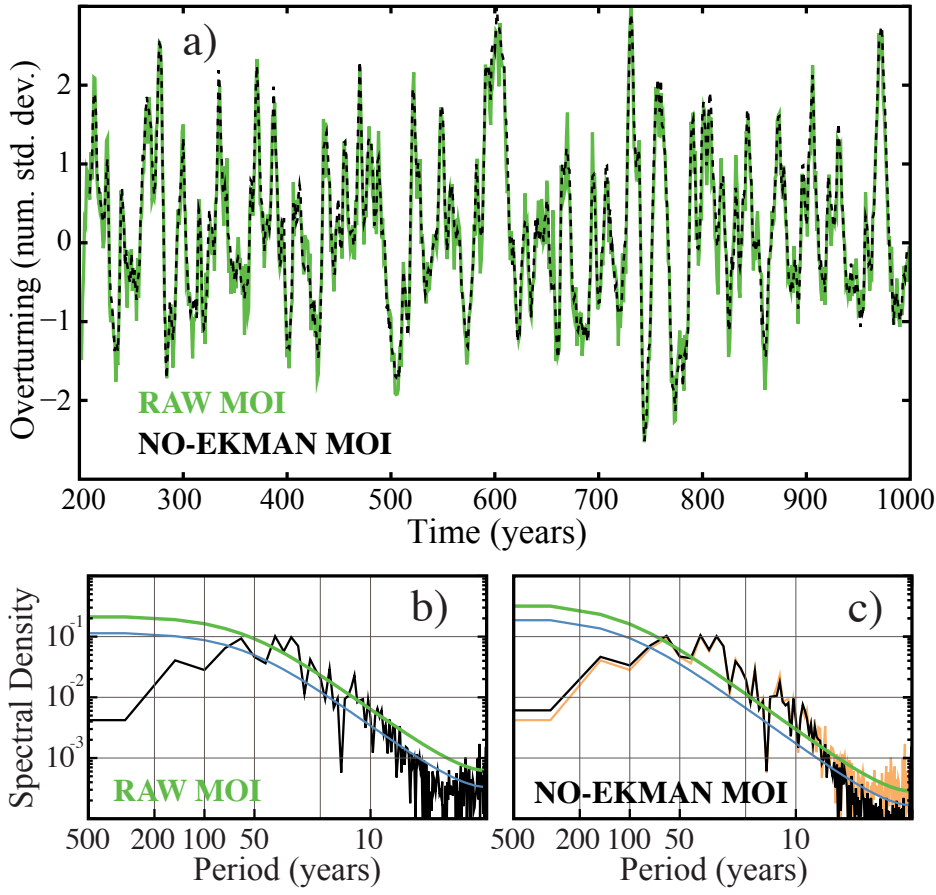

Fig. 3.2: a) Time series of the normalised MOI (in std. dev.), defined as the local overturning at 1050 m and 47.4°N (climatological maximum). The dashed line represents the MOI after removing the Ekman signal. Note that the standard deviation of the MOI is 1.8 Sv. b-c) Fourier spectra of the raw and Ekman filtered MOI, respectively. The black solid lines represent the spectrum calculated for the complete simulation. In c), the orange line shows the spectral density for the raw MOI to ease comparison. The blue line accounts for the spectrum of a red noise process with the same first autorregresive coefficient as the complete time-series. The green line sets the 90% confidence interval of this red-noise process.

Figure 3.4 shows the main spatial features of North Atlantic convection in March (when events of deepest convection occur). The variability of convection is commonly represented by the variations of the Convective Depth (CD). Unfortunately, this variable was not stored in this control run, and we use the Potential Energy Released by Convection (PERC) instead (similarly to Timmermann et al., 1998). The variability of the PERC and the CD has been compared in the other simulations with the ECHO-G model (see Chapter 2), and they produce virtually identical results for both variables (not shown). The mean PERC pattern (Figure 3.4a) shows three main convection regions with comparable climatological values: the East Labrador, Central Irminger, and Norwegian Seas. More interestingly, variability of convection is considerably larger near the Labrador Sea (Figure 3.4b). ECHO-G is not eddy-resolving, and therefore the representation of deep water formation lacks some essential dynamics that could explain the main discrepancies with respect to observations (Marshall and Schott, 1999), such as the rather eastern location of Labrador convection, or the relative small variance in the Norwegian Seas. Likewise, convection in Central Irminger Sea has been reported in other models (e.g. Guemas and Salas-Mélia, 2008; Lohmann et al., 2009; Msadek and Frankignoul, 2009), but is not supported by observations.

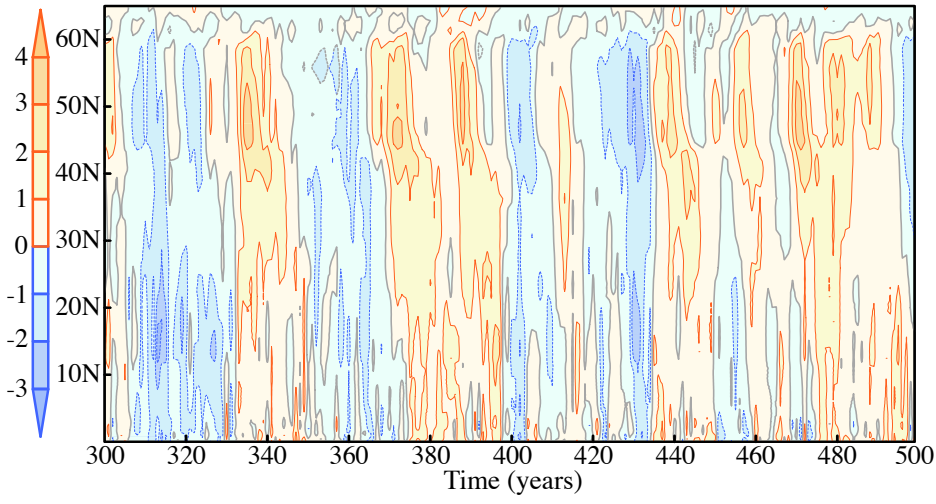

Fig. 3.3: Zonally averaged northward transport anomalies integrated between 100 and 1050 m depth (in Sv). Note the two different timescales of variability in tropical and extra-tropical latitudes and the southward propagation of anomalies.

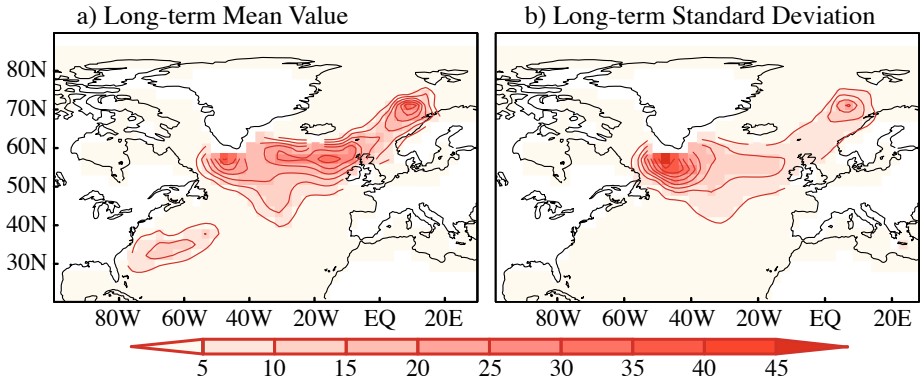

Fig. 3.4: (a) Long-term mean and (b) standard deviation of the Potential Energy Released by Convection (PERC; in W/m^2) in March.

3.2 Regression model for the natural AMOC variability

Deep convection variations in the North Atlantic are thought to play an important role in determining AMOC low-frequency variability (e.g. Griffies and Bryan, 1997; Hall and Stouffer, 2001; Hawkins and Sutton, 2007; Ortega et al., 2011c). The occurrence of these convection events is influenced by local stochastic forcing from the atmosphere. This section is concerned with understanding how the ocean integrates the anomalous heat fluxes at the main region of deep water formation, and quantifying how the integrated signal contributes to the variance of the overturning.

3.2.1 The role of convection

The regression patterns between the MOI and the surface heat flux (HFL) anomalies in the convection regions are shown in Figure 3.5. Similar patterns emerge for the PERC (not shown), providing evidence of the role of the HFL on convection. Indeed, the largest HFL anomalies are found to the south of Greenland, in the same region as the maximum standard deviations of the PERC (Figure 3.4b). A significant influence of local heat fluxes on the AMOC variability is observed during the 10 years preceding the large overturning anomalies (Figure 3.6). Moreover, the regression patterns of the HFL have similar spatial features for all lead times up to 10 years, and show their maximum regression coefficients when the HFL leads the overturning by 2 years (Figure 3.5a). No clear influence of fresh water fluxes is observed on convection (not shown). Indeed, evaporation is inhibited as a response to the cooling of surface temperature forced by positive (into

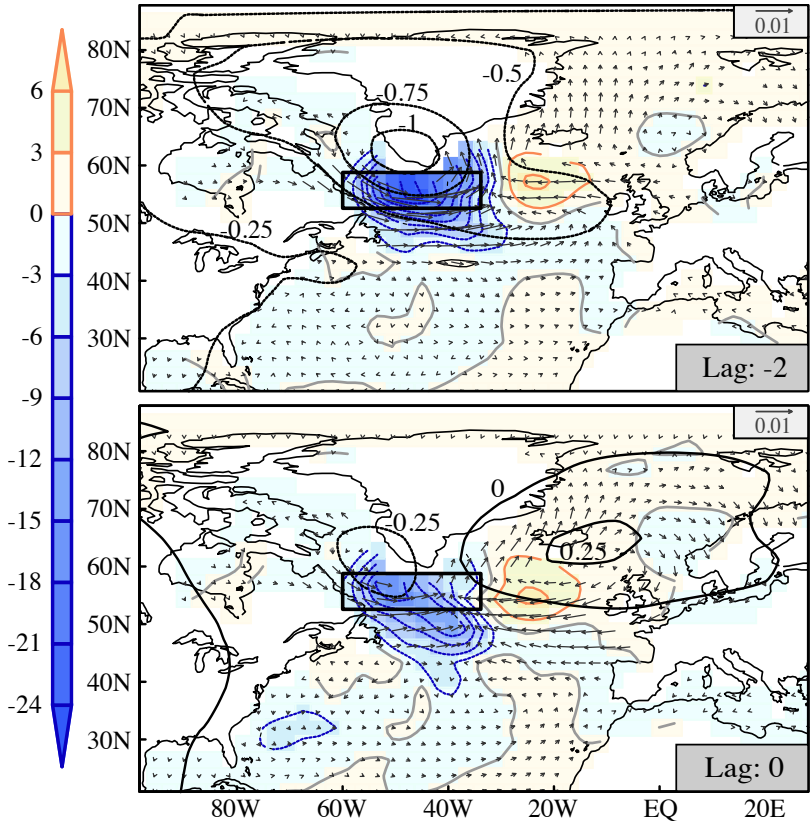

Fig. 3.5: Regression patterns between the normalised MOI and the anomalies of heat flux (shaded, in W/m^2 per std. dev. of the MOI), the wind-stress (vectors, in N/m^2 per std. dev. of the MOI) and the sea level pressure (black contours, in hPa). Two different lags are considered: the heat flux wind-stress and sea level pressure leading by 2 years (top) and all variables in phase with the MOI (bottom). The black rectangle delimits the region where the HFL index is defined.

the ocean) heat fluxes. Large overturning changes seem, therefore, to be triggered by persistent strong heat flux interaction with the atmosphere, favoured by an intensification of northwesterly winds over the Labrador Sea (vectors in Figure 3.5, blue line in Figure 3.6). A similar pattern of heat flux and wind variations leading the overturning by 3 years was found by Delworth and Greatbatch (2000) in a previous version of the GFDL model, which they related to the North At-

lantic Oscillation. In this case, however, the surface forcing is driven locally by negative sea level pressure (SLP) anomalies centred to the south of Greenland (black contours in Figure 3.5). At lag zero (Figure 3.5b) the HFL pattern over the Labrador Sea is weakened, along with the local wind forcing. Simultaneously to the east, a pattern of anomalous easterlies emerges at midlatitudes, centred around 50°N, where the MOI is defined.

3.2.2 Constructing a linear regression model

The local atmospheric influence on convection and thereby on the overturning is represented by the average of the heat flux anomalies to the south of Greenland (black rectangle in Figure 3.5). This timeseries is used to produce a univariate regression model for the overturning circulation,

$$\mathbf{MOI}(t) = \alpha \sum_{i=1}^{L} \omega_i H(t-i) + \xi(t) \tag{3.1}$$

where MOI represents the overturning index to reconstruct, α is the regression coefficient, ω is the weighting function for time integration, H is the predictor (i.e. the heat flux index), ξ accounts for the residuals, i is the lag in years and L is the maximum lag. To ensure that we are only using information prior to the variability being predicted, we use $i > 0$ only.

The main features of the heat flux integration are determined by considering different integration approaches. Since the magnitude of the HFL influence varies with time, three weighting schemes were tested. One is based on the correlation values in Figure 3.6, and the others make use of triangular and Gaussian weighting functions with different slopes and decay rates, respectively. Different time integration periods were also considered. The best univariate model is achieved using a Gaussian weighting function maximum at lag -2 (when the influence of convection is maximum) that decays smoothly up to lag -10 (see Figure 3.6). It coincides with the period with non-negligible correlations between the AMOC and the HFL index (Figure 3.6). This analysis therefore reveals that there is a decadal integration of the heat flux anomalies by the ocean. Using this approach the variance explained by the regression model is 69.6%, almost 20% higher than when no time integration is employed (Table 3.1).

The zero-lag correlation pattern between the residuals from the regression model and the wind stress anomalies (not shown) exhibits a band of mid-latitude anomalous easterlies near the latitude where the MOI is defined, similar to the eastern signal in Figure 3.5b. This is the contribution of the Ekman transport which is unrelated to the first predictor, and will be removed for the construction of the regression model. The signal is isolated by calculating a simple linear

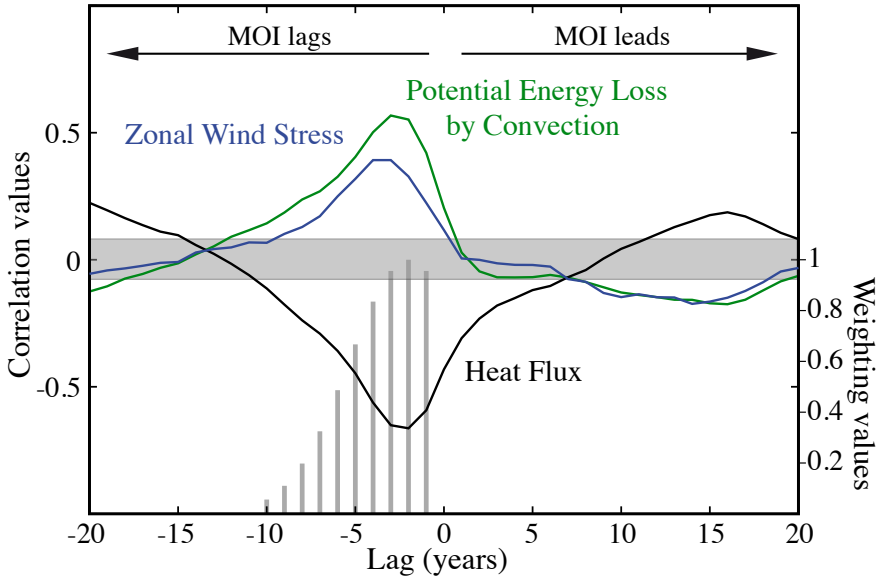

Fig. 3.6: Time-lag correlations between the MOI and the average of ocean and atmospheric variables in the convection region (box in Fig. 3.5). The shaded region delimits the 5% significant domain. The grey vertical bars show the temporal weighting scheme employed to integrate the first predictor (HFL index).

Table 3.1: Variance explained by the regression models using both raw and time integrated predictors. HFL represents the local heat fluxes in the Labrador Sea, while ISD accounts for the influence of density anomalies in the Irminger Sea.

	Raw HFL	Integ. HFL	Integ. HFL + Integ. ISD
Raw MOI	51.0%	69.6%	
No-Ekman MOI	54.8%	74.5%	82.8%

regression between the average of the zonal wind stress at 43° N (latitude with the largest correlations) and the residuals from the univariate model. The resulting series is then filtered out of the raw MOI (dashed line in Figure 3.2a), and the univariate model is recalculated for the new index. As a result, the fraction of variance explained by the predictor increases, reaching a maximum value of 74.5% when the same time integration scheme is considered. Note that this filtering mostly removes interannual variability (Figure 3.2c), and keeps variability

at decadal and multidecadal timescales, that are the timescales of interest for predictability. In the remainder of the text MOI will refer to the Ekman-filtered overturning index.

3.2.3 Validating the univariate model

In order to validate the use of the HFL index as a predictor of the MOI variability, the simulation is divided into two halves and the univariate regression model is recalculated using the first half. The regression coefficients obtained for the initial period are now employed to reconstruct the MOI timeseries for the second part of the simulation. The reconstructed overturning (dashed line in Figure 3.7) is in good agreement with the real (Ekman-filtered) MOI, with a correlation value of 0.85. This same value is obtained if the reconstruction is performed using the regression coefficients from the whole timeseries. Therefore, the regression model is reasonably consistent throughout the whole run. However, the prediction tends to underestimate the variability at shorter timescales, as well as the magnitude of change during the largest overturning variations. A scatterplot analysis of the residuals over the second half of the simulation (solid points in Figure 3.8) reveals that the magnitude of the error is proportional to both the MOI (blue points; correlation coefficient, r = -0.49) and the decadal change preceding that event (yellow points; r = -0.38). If the regression model was consistent, both correlation values should be close to zero. In order to improve the regression model, the contribution of other different processes needs to be explored through an analysis of the residuals.

3.2.4 The bivariate regression model

The aim of this subsection is to analyse the influence of other processes in order to improve the regression model by defining a new predictor that extracts the maximum possible coherent variability from the residuals, whilst ensuring it has a physical basis to avoid overfitting. The relationship between the residuals and the main atmospheric and oceanic variables is explored by means of a time-lag correlation analysis. The largest signal is found for density anomalies in the Irminger Sea (Figure 3.9). Positive correlations are found in the upper ocean (0 to 800 m) to the south of the Greenland-Scotland Ridge, about 4-6 years before the maximum of the overturning. This pool of dense waters appears to propagate westward, where it modifies the background stratification, and then propagates southward towards the Equator. At deeper levels (1000 to 1500 m), a zonal density gradient is established between a pool of dense waters near the Irminger Sea (just south of the Denmark Strait) and a region of lighter waters in

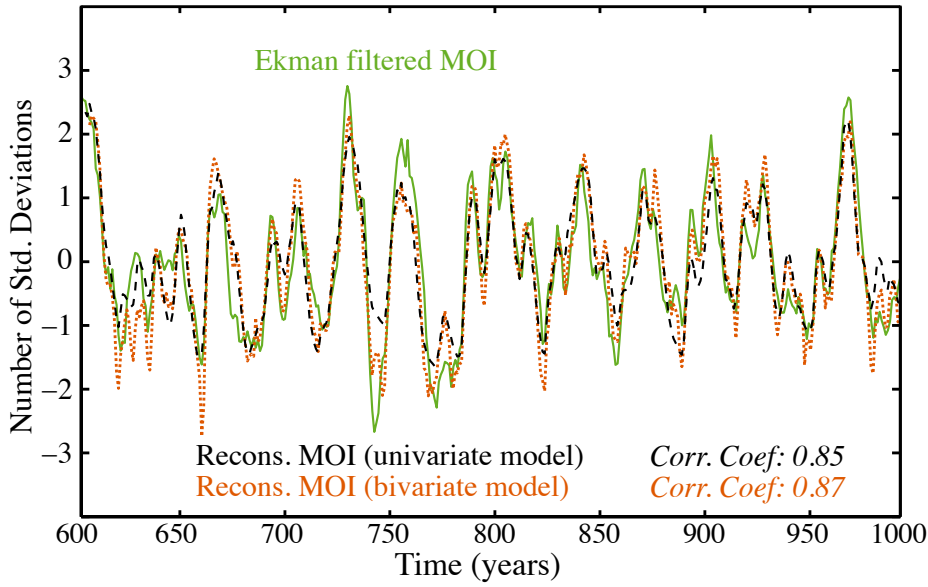

Fig. 3.7: Time series of the true (Ekman-filtered; green) and reconstructed MOI during the second half of the CTRL1 simulation (years 600-1000) for the univariate (black) and bivariate (orange) regression models. The correlations between the reconstructed and the true MOI are in italics.

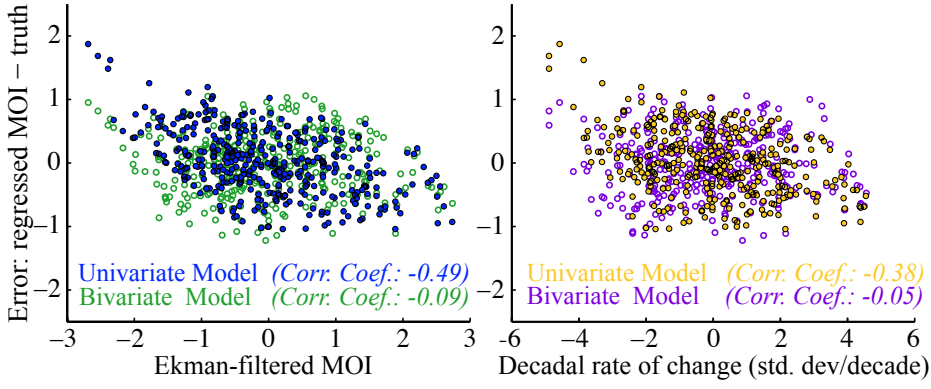

Fig. 3.8: Scatter plots between the residuals from the regression models and both the Ekman-filtered anomalies of the MOI (left) and the decadal rates of change (right). All these results correspond to the second half of the CTRL1 simulation.

the vicinity of the British Isles. The zonal dipole persists as the positive density anomalies propagate along the western boundary. This propagation is reminiscent of the oscillation mechanism described by both Colin de Verdière and Huck (1999) and Te Raa and Dijkstra (2002), in which westward propagation of buoyancy anomalies produces zonal and meridional overturning responses.

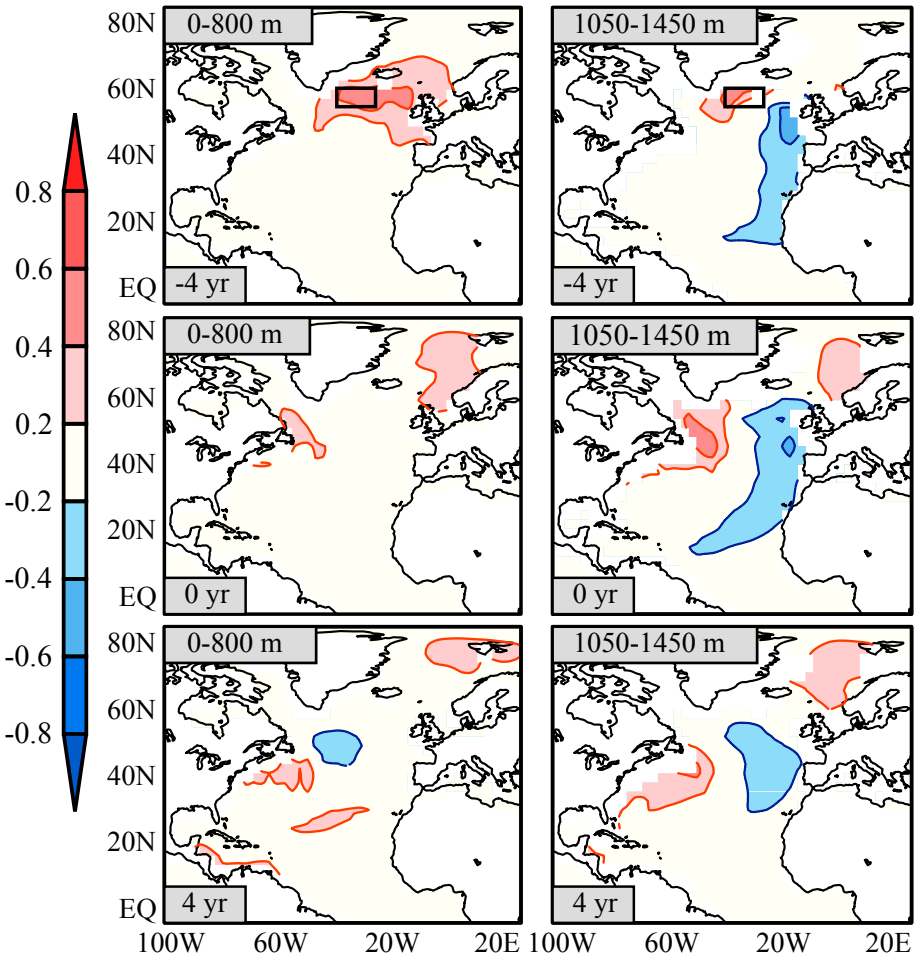

Fig. 3.9: Lagged cross-correlation patterns between the residuals of the univariate model and the mean values of density for two different depth ranges. The black box indicates the region where the second predictor (ISD) is averaged.

A new predictor is defined by averaging the density anomalies in the upper 1500 m of the western Irminger Sea (grey box in Figure 3.9). This new Irminger Sea density index (ISD) is related to an increase of convection from the Irminger Sea to the British Isles (Figure 3.10a), the same region occupied by the upper density anomalies in Figure 3.9. A similar band of dense waters, also related to convection, was identified by Msadek and Frankignoul (2009) in the IPSL model. They found that deep convection is activated by the advection of salty waters, responding to variations in the East Atlantic Pattern. The resulting changes in density led the overturning variations by about 3-5 years. A similar lead time is observed in our model (Figure 3.11). However, the origin of these anomalies is rather different. Simultaneously to the increase of convection, there is an enhancement of the southward flow through the Denmark Strait (Figure 3.10b), and a local cyclonic gyre is formed to the east of Cape Farewell. As a result, cold waters from the Nordic Seas are advected to the east (Figure 3.10c), reaching the regions of convection, where they help to keep the water column destabilised. No influence of salinity anomalies is found in this case (Figure 3.10d).

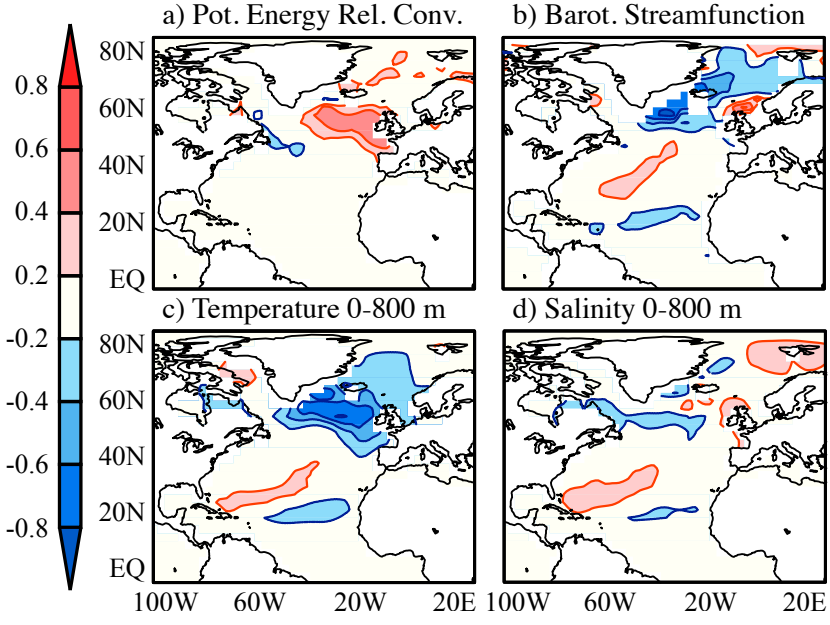

Fig. 3.10: Correlation patterns between the second predictor and four ocean variables: (a) potential energy released by convection, (b) barotropic streamfunction, (c) and (d) temperature and salinity means in the upper 800 m.

The two predictors are now used to build a new bivariate regression model, described by the generic equation,

$$\mathbf{MOI}(t) = \alpha \sum_{i=1}^{L} \omega_i H(t-i) + \beta \sum_{j=1}^{M} \sigma_j I(t-j) + \xi(t) \tag{3.2}$$

where, similarly to Equation 3.1, MOI corresponds to the Ekman-filtered overturning timeseries, α and β are the regression coefficients, ω and σ are the weights used for time integration, H and I are the two predictors (i.e. HFL and ISD respectively), and finally ξ is the term accounting for the residuals of the bivariate model.

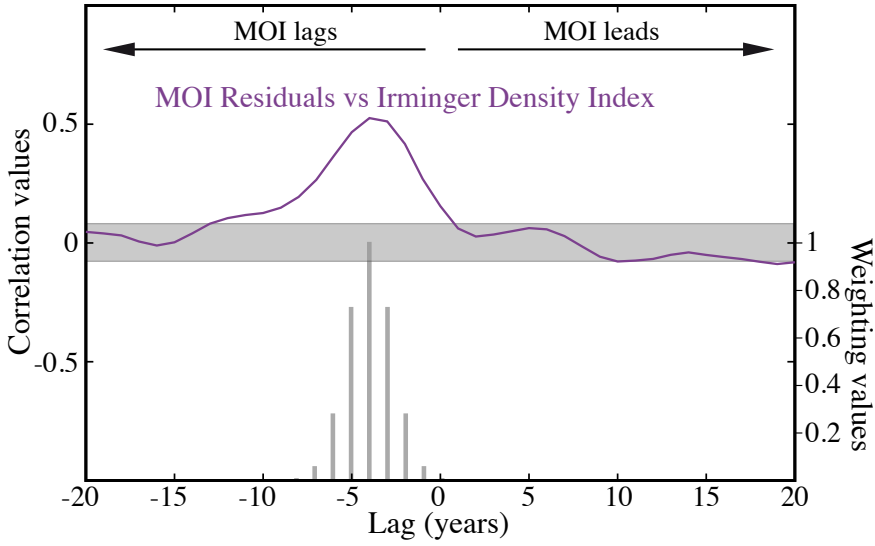

Fig. 3.11: Time-lag correlations between the residuals of the univariate model and the second predictor (ISD; calculated as the average of density at the upper 1500 m of the Irminger Sea; grey box in Fig. 3.9). The shaded region delimits the 5% significant domain. The grey vertical bars show the temporal weighting scheme employed to integrate this predictor.

The same weighting schemes and integration periods as considered for the HFL index are tested again for the ISD index. In this case, the best regression model is again obtained for a Gaussian weighting function, but centred at lag -4 (when the correlations between the residuals from the univariate model and the

ISD index are maximum; Figure 3.11). This Gaussian function decays rather fast as compared to that of the first predictor, thus suggesting a short-time influence of the ISD. As a consequence, the signal of this second predictor is integrated over a shorter period (i.e. 7 years) than for the HFL index. The variance explained by this bivariate model rises to 82.8%, i.e. an increase of more than 8% with respect to the former univariate model.

A significant improvement is also found in the validation process. The bivariate regression model is again recalculated in the initial half of CTRL1, and its regression coefficients are employed to reconstruct the overturning during the second half. The new reconstructed MOI (orange dotted line in Figure 3.7) is slightly better correlated with the true MOI (r = 0.87, instead of 0.85). The magnitude of change of the large overturning variations is generally better represented, although in some cases is clearly overestimated (Figure 3.7), for example at year 670. Perhaps more importantly, the bivariate model is more consistent, since the correlations between the residuals and both the MOI and the decadal change preceding them are clearly smaller (unfilled circles in Figure 3.8). A subsequent analysis of these bivariate residuals shows no clear evidence of another coherent oceanic or atmospheric influence.

3.3 Rapid decadal overturning increases and decreases

3.3.1 Representing rapid decadal overturning changes with the regression model

As a final step, the bivariate model is evaluated during large, rapid decadal changes in the MOI. These events are especially important, as they are likely to produce the largest climate impacts.

The largest decadal changes (both increases and decreases) in the MOI are identified, and their magnitudes are compared in Figure 3.12. There appears to be an asymmetry in the sign of the rapid changes, with positive rapid events (orange line) generally being larger than the negative events (blue line). However, the two largest decadal changes are found to be rapid decreases in the MOI. The reasons for this possible asymmetry are not clear, and merit some further analysis, which will be developed in subsection 3.3.3.

Figure 3.13 collects all 13 of the episodes in which the decadal change is larger in magnitude than 3 standard deviations (i.e. $\sim$ 5 Sv or $\sim$ 30% of the mean MOI, 16.5 Sv). The evolution of both the true (Ekman-filtered), and the reconstructed MOI are shown, along with the leading signal of the two predictors. Since negative HFL variations are associated with increasing overturning events, the sign of

this precursor has been reversed in the plot to ease comparison. Although we cannot expect a precise correspondence between the actual and the predicted MOI timeseries, it is immediately clear that the sign of the change is well reproduced, but the magnitude is generally underestimated. In every event, the sign associated to the HFL is the one expected to explain the MOI variations. In contrast, the role of dense waters in the Irminger Sea is not always important, and its value is found to vary both in magnitude and sign. To conclude, the limitations of the regression model show that the largest decadal rapid events are subject to additional influences beyond the predictors identified herein.

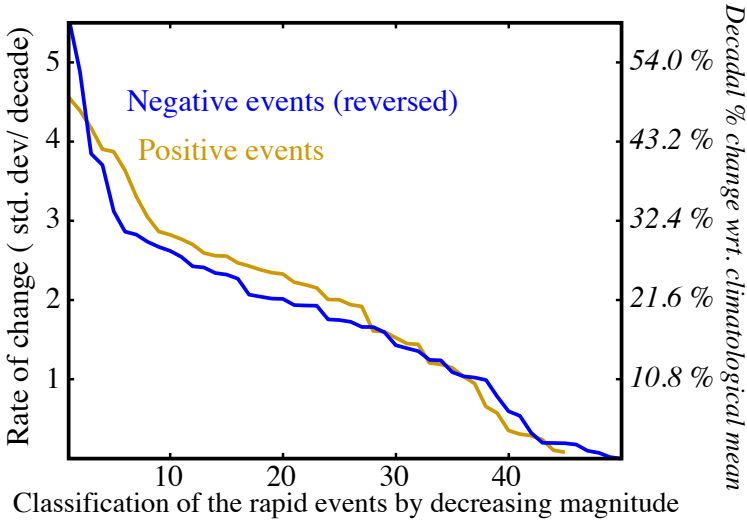

Fig. 3.12: Rate of change of the large, decadal rapid overturning events ordered in decreasing magnitude (in std. dev./ decade). Note that the sign of the negative events has been reversed to allow comparison with the positive events.

3.3.2 Climate impacts of the rapid overturning fluctuations

Given the capability of the regression model to represent the rapid decadal overturning changes it is important to evaluate which are the associated climate impacts accompanying these rapid events in the ECHO-G model, since they could show evidence of regions with some potential predictability. The fingerprints in surface air temperature (SAT) and precipitation are analysed separately for the 8

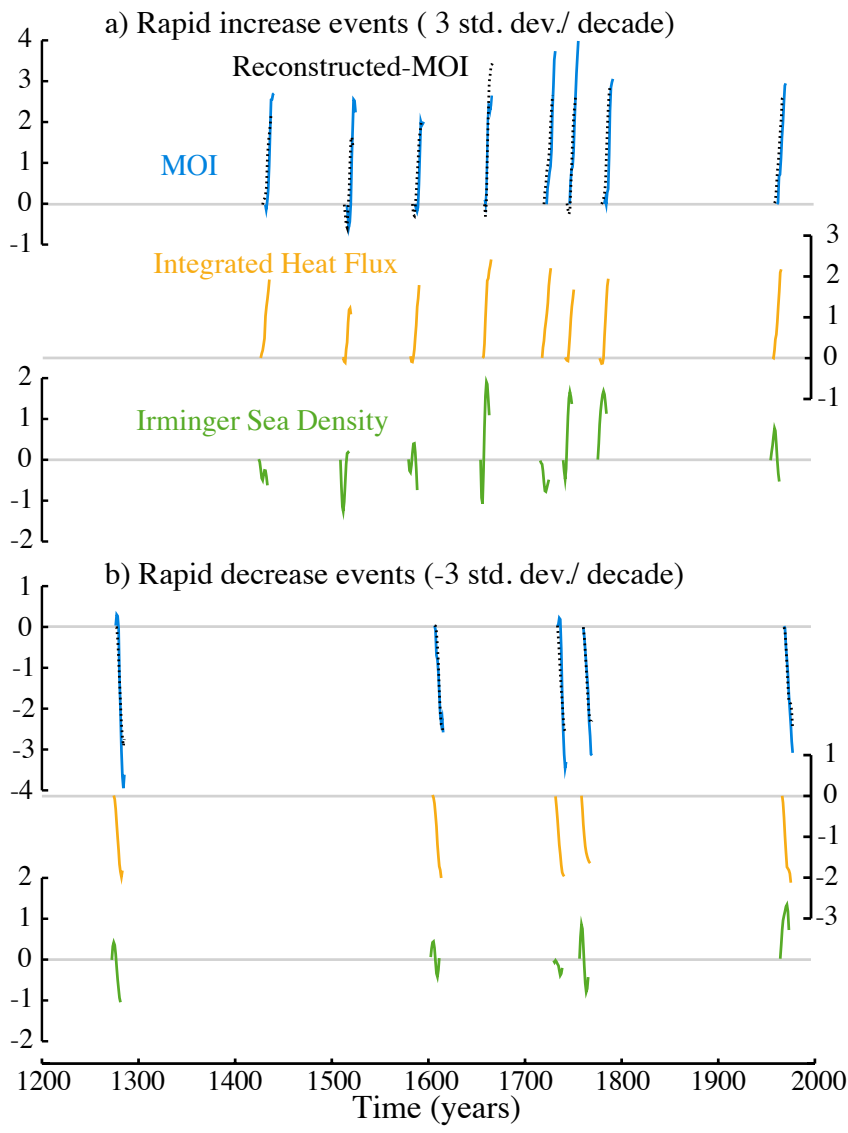

Fig. 3.13: Evolution of the original Ekman-filtered MOI (blue), the reconstructed index (black) and the predictors (yellow and green) during the largest, rapid decadal overturning events (change above 3 std dev./decade, i.e: 5.4 Sv/decade). Note that the HFL sign is reversed to allow a direct comparison with the other variables.

largest AMOC increases and 5 largest decreases (see Figure 3.13), by calculating the difference in means between the three last and first years in all decadal events (Figures 3.14 and 3.15). Significance is assessed by comparing these differences to the percentiles 2.5th and 97.5th of a Monte Carlo ensemble with 1000 random selections of 8 and 5 decadal events respectively for the rapid increases and decreases.

The main response to the rapid decadal AMOC increases is a general warming across Northern Europe with significant positive values of about 1°C over North Europe and western Russia (Figure 3.14a). Similar changes were observed for transitions from weak to strong overturning states in other millennial simulations with the CCSM3 model (Hofer et al., 2011), and the HadCM3 model (Hawkins and Sutton, 2008). Besides the temperature rise at northern high-latitudes there is also a weak but significant temperature drop at the tropical Atlantic, both supporting an increase of the northward meridional heat transport. Other not significant changes are observed near the sinking regions of Labrador (the warming indicating more energy released by convection) and the Ross Sea (the cooling being thereby a sign of lesser convection activity). In terms of precipitation, major changes are localised near the Equator (Figure 3.14b), characterised by a dipole structure with decreased precipitation in the Eastern Pacific, and increased precipitation over the Western Pacific and the Indian ocean. However, these changes are mostly insignificant.

Interestingly, the main climate changes associated to the large decadal overturning decreases (Figure 3.15) are not exactly opposite to those described for the increases. For example, a maximum cooling is observed in the Irminger and Nordic Seas, with negligible influence in Northern Europe (Figure 3.15a). At mid-latitudes, a meaningful moderate warming is observed from western Europe to Asia, establishing a meridional SAT dipole with the tropics. A narrower meridional dipole structure is found for the changes in precipitation (Figure 3.15b), with negative anomalies north of the Equator, and positive values to the south. This picture bears some degree of similarity with the fingerprint of a southward displacement of the ITCZ, as reported in response to a collapse of the AMOC (Vellinga and Wood, 2002; Stouffer et al., 2006). Note that, however, the dipole structure is not clearly supported by the assessment of significance.

The asymmetrical climate response to the rapid increases and decreases points to potential differences in the evolution and the triggering mechanisms of such events. It therefore highlights the necessity of performing separate analyses to capture the particularities of both events, and suggests that the regression models could be improved if the asymmetry between the AMOC increases and decreases was taken into account when the potential predictors were analysed.

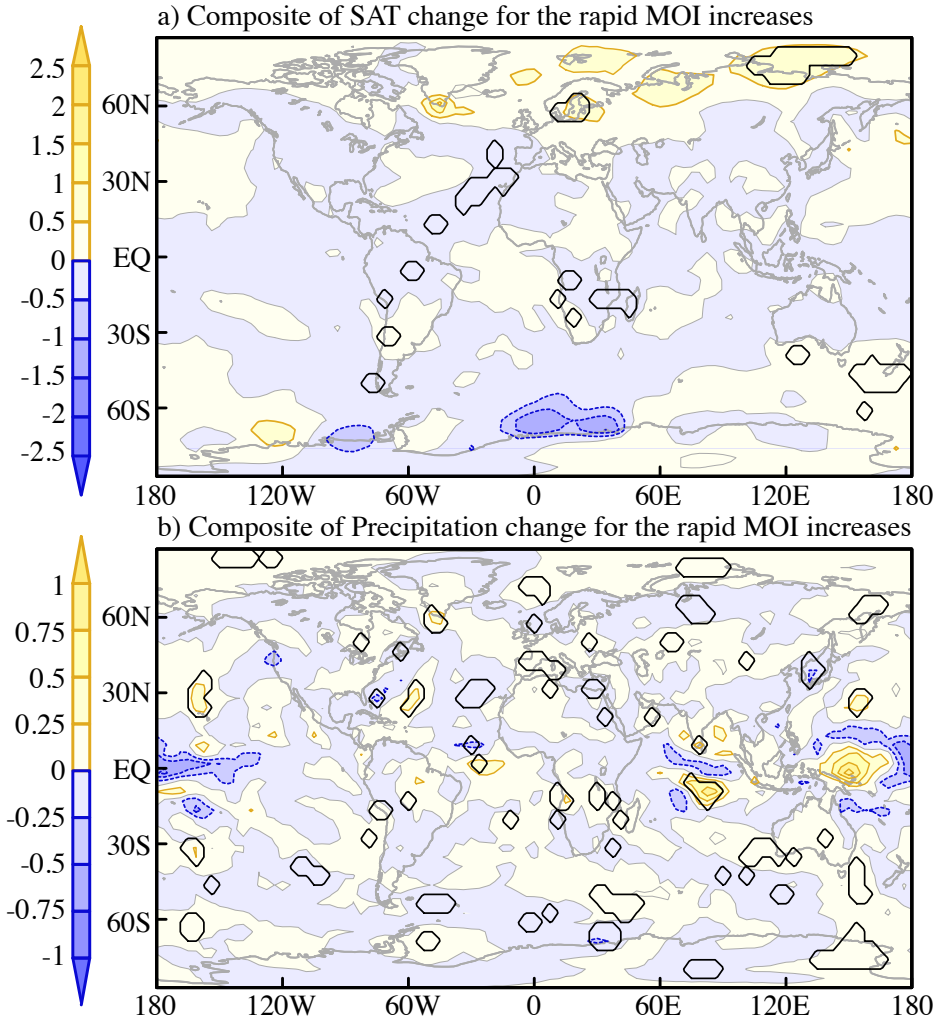

Fig. 3.14: Changes in: a) Surface atmospheric temperature (SAT, in K) and b) Precipitation (in mm/day) between the last three years and the first three years of the *rapid decadal overturning increases* in Fig. 3.13. Black contours indicate significance at the 5% level as compared to the differences of the 2.5 and 97.5 percentiles in a suite of 1000 Monte Carlo random selections of 8 decadal events in CTRL1.

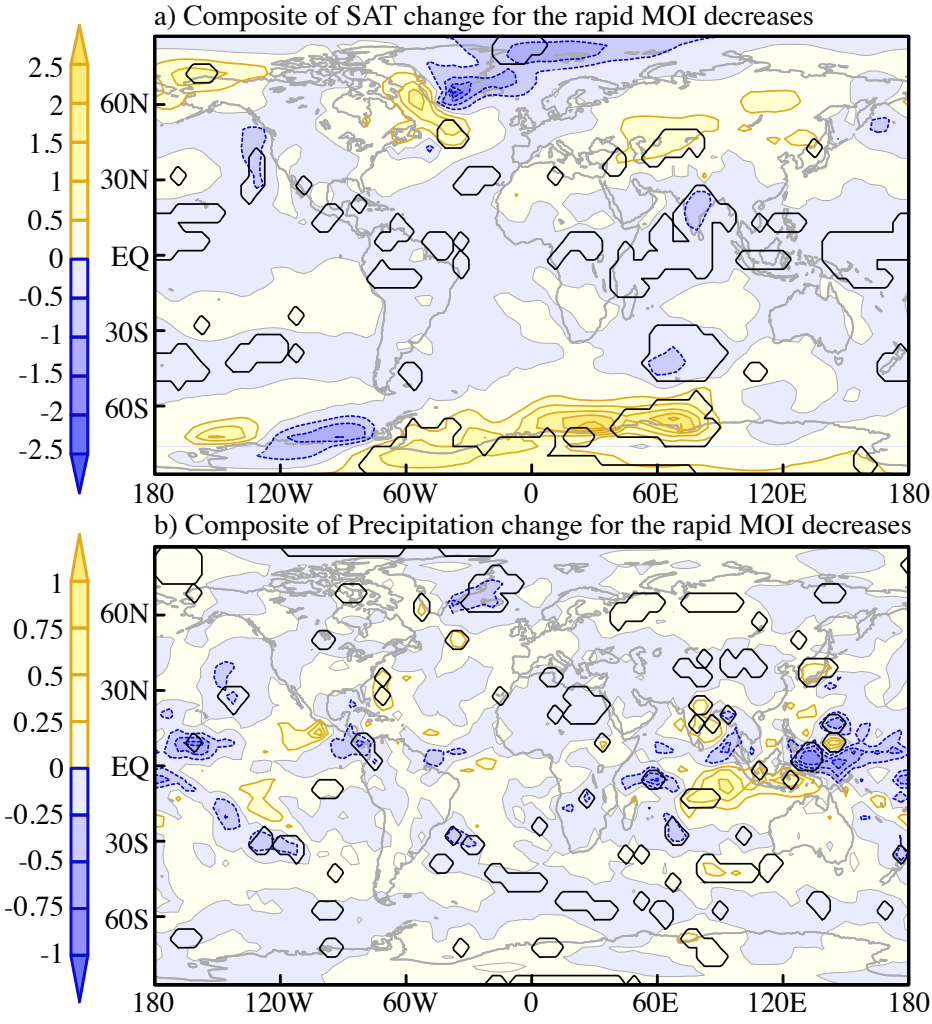

Fig. 3.15: The same as in Fig. 3.14 but for the rapid decadal overturning decreases. In this case, significance is established by comparison with 1000 Monte Carlo random selections of 5 decadal events in CTRL1.

3.3.3 Asymmetry between rapid AMOC increases and decreases

This section aims to understand the reasons for the observed asymmetry between the largest overturning increases and decreases (Figure 3.12). Three specific points deserve our attention: first, why there is an apparent majority of rapid increases relative to the rapid decreases; second, why the two most extreme events are rapid decreases; and third, whether these two aspects of the asymmetry can be accounted for by the two predictors.

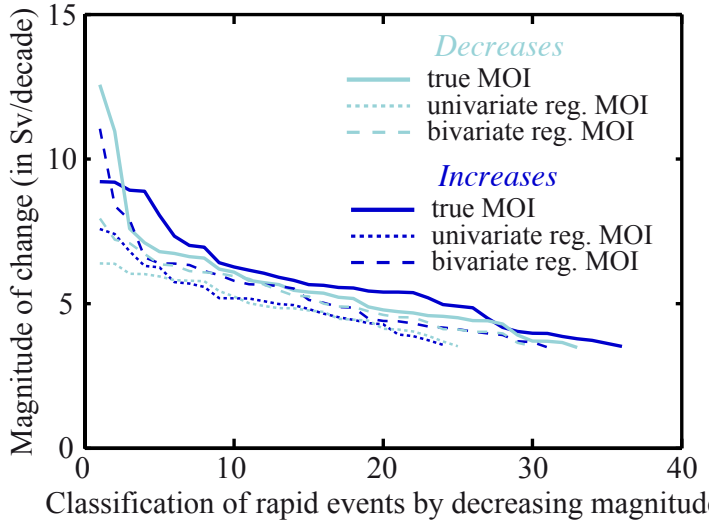

Fig. 3.16: Classification of the top rapid MOI increases and decreases for the original timeseries (solid lines) as well as for the univariate and bivariate regression models (dotted and dashed lines, respectively). Note that the events in the true MOI do not necessarily correspond with those in the regression models.

Since not all the rapid events occur exactly at decadal timescales, a new method for the selection of rapid increases and decreases is now considered. Under the new definition, the length of the rapid events can vary from 6 to 20 years, and their magnitude of change is standardised to units of Sv/decade to better allow for classification (solid lines in Figure 3.16). All the events selected are still characterised by a steep AMOC change. Figure 3.16 shows that under the new selection criteria the two main aspects of the asymmetry are still represented.

To gain further insight on the reasons for the asymmetry and the contribution of each predictor, the rapid AMOC events are now calculated for the univariate

and bivariate regression models. The univariate model itself is able to reproduce the general occurrence of larger rapid increases than decreases (dotted lines in Figure 3.16), thus pointing to a relevant role of the first predictor to explain this aspect of the asymmetry. Indeed, a histogram of the HFL index highlights some skewness to stronger negative values (this being related to positive overturning values) for the yearly and integrated heat-flux anomalies (Figure 3.17a), as well as for their corresponding rapid changes (Figure 3.17b), all consistent with relatively stronger AMOC increases.

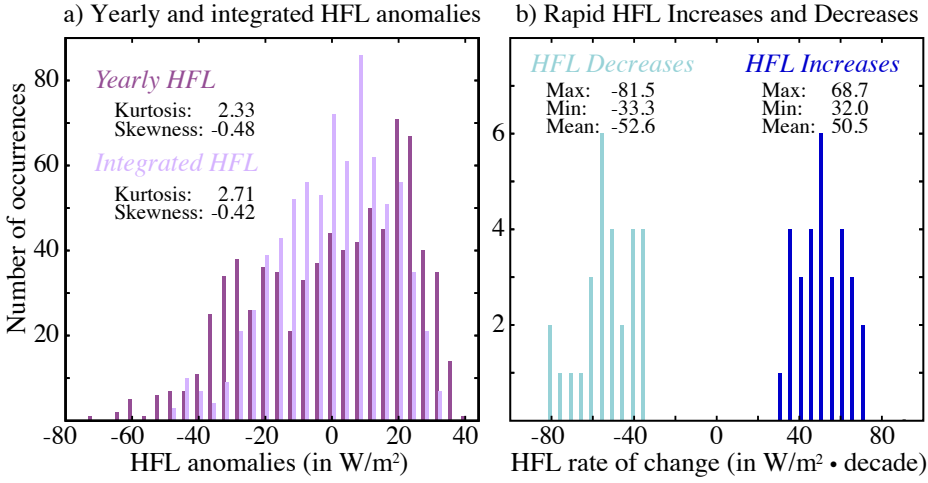

Fig. 3.17: Histograms of a) yearly (green line) and integrated (yellow line) HFL anomalies; b) rapid HFL increases (yellow line) and decreases (green line).

The inclusion of the second predictor produces an overall improvement in the representation of the rapid overturning changes (dashed lines in Figures 3.16), however, it still fails to explain the remarkable magnitude of the two extreme MOI decreases. Moreover, if the focus is set on the precise rapid events selected for the true MOI index (Figure 3.18), the bivariate model is found to misrepresent some particular events well described by the univariate model (e.g. 14th and 17th decreases and 8th and 22nd increases). Therefore, even if the second predictor succeeds to explain more variance of the MOI, it is not optimal for the representation of the rapid AMOC changes.

The analysis reveals that some important contribution to the rapid events is not captured by the bivariate model. Also, as illustrated in the previous subsection, some particular discrepancies are evident in the nature of the rapid increases

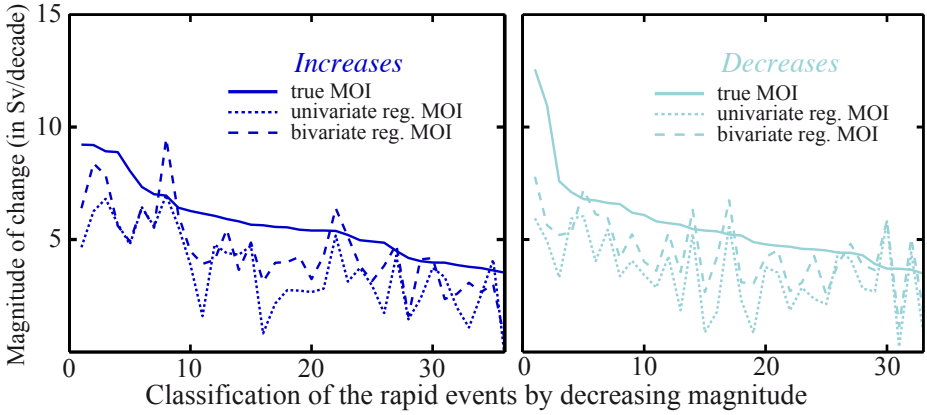

Fig. 3.18: Classification of the top rapid MOI increases and decreases for the original timeseries (solid lines), along with the magnitude of change as represented by the univariate and bivariate regression models (dotted and dashed lines, respectively). Note that in this case, unlike for Fig. 3.16, the timing and length of the rapid events coincides for the true and regressed MOI indices.

and decreases. These results highlight the need for a different approach, in order to better capture the particularities of both types of rapid events. The univariate regression model (which broadly explains some aspects of the asymmetry) could be improved through a separate analysis of the misrepresented rapid MOI increases and decreases. In this way, new predictors can be precisely defined for the characterization of rapid events. In particular, the analysis of the two largest decreases can shed light on the specific conditions determining their occurrence. These analyses, however, would require a comprehensive study of the different events that is beyond the intended extent for this chapter.

3.4 Conclusions

The processes influencing the predictability of decadal variability in the AMOC have been analysed in a long control simulation with the ECHO-G coupled climate model.

Two forerunners of AMOC variability have been identified, related to local processes in the Labrador and Irminger Seas. The first predictor is the anomalous heat flux averaged over a region in the Eastern Labrador Sea, and represents the local stochastic forcing integrated by the ocean. The atmospheric influence

is largest at a lead time of 2 years, but the effective integration by the AMOC is found to extend to lead times up to 10 years. An univariate regression model with this index explains 74.5% of the variance in the AMOC, after the Ekman component has been removed. The analysis of the regression model's residuals allows the identification of a second predictor. The latter is defined as the mean ocean density in a region of the Western Irminger Sea, and is associated with a zonal density gradient at deeper levels, that leads to an enhancement of the western boundary current, and hence the overturning. The buildup of anomalous dense waters in the Irminger Sea precedes the maximum AMOC values by about 6 years. A final bivariate regression model is obtained integrating the first predictor over 10 years, and the second over 7 years, both using gaussian integration schemes. It explains 82.8% of the total Ekman-filtered AMOC variance.

The origin of the dense anomalies in the Irminger Sea appears to be related to the variability of the outflows from the Nordic Seas. Hawkins and Sutton (2008) found that discharges of dense waters through the Denmark Strait preceded the rapid AMOC changes in a long control simulation with the HadCM3 model. Our analysis supports the role of the outflow through the Denmark Strait, and an intensification of the gyre near the Irminger Sea to explain the cold dense waters south of the Sill. It also suggests a further role of local convection in which anomalous surface heat fluxes over the Irminger Sea lead to the formation of density anomalies.

The regression model's performance is assessed for large, rapid AMOC changes (both decadal increases and decreases larger than 3 standard deviations). These are well described by the heat flux variations in the Eastern Labrador Sea, although other processes may also play a role on the onset of these events. Yet, the contribution of Irminger density anomalies is mostly negligible. A possible asymmetry in the sign of large rapid decadal events is noted, with rapid increases being more common than rapid decreases. Climate impacts of such rapid fluctuations also show evidence of some asymmetric behaviour. The dominant feature of the response to the rapid overturning increases is a general warming in the northern extratropics, with major influence over Northern Europe and Russia. This result is in relative good agreement with comparable events in other model simulations (Hawkins and Sutton, 2008; Hofer et al., 2011). In contrast, rapid decadal decreases, which are more likely to occur in the current context of climate change, are associated in the ECHO-G model with a cooling over the Nordic Seas with no influence over Europe, and equatorial precipitation changes reminiscent of a southward change in the ITCZ belt (Vellinga and Wood, 2002).

Identification of new predictors for AMOC variability is important for ocean monitoring strategies. This study supports the key role of the subpolar North Atlantic, and in particular of the Labrador and Irminger Seas as found by many

previous studies, and advises separate analyses of the rapid overturning increases and decreases to better represent their particular features. Further evidence from other models and reconstructions is necessary to better constrain the validity of these results.

Finally, the current study has been performed in a present day control integration with constant radiative forcings. It is not known whether the presence of external forcing variations (e.g. solar activity, volcanic and anthropogenic aerosols, greenhouse gas concentrations) would modify the modes of variability in the ocean, and therefore the validity of our AMOC predictors. In the next chapter, the analysis will be extended to forced simulations of the last millennium as well as scenario simulations, and a comprehensive comparison between the forced and unforced AMOC features will be established.

4

Atlantic Meridional Overturning Circulation variability in the period 1000 to 2100 AD *

¿Quién es el mar? ¿Quién es aquel violento
y antiguo ser que roe los pilares
de la tierra y es uno y muchos mares
y abismo y resplandor y azar y viento?

Jorge Luis Borges. El otro, el mismo. 1964

AMOC variability is an important factor to understand past, present and future climate changes. During the last glacial period, large and abrupt climate changes have been related to fluctuations in the AMOC, either through a transition between two stable circulation modes (generally known as Dansgaard-Oeschger events; Dansgaard et al., 1993), or through a partial or complete AMOC collapse possibly triggered by massive iceberg discharges (known as Heinrich events; Heinrich, 1988; Bond et al., 1992). Future climate projections also predict a slowdown of the AMOC circulation (modulating the global warming signal) by the end of the 21^{st} century (Gregory et al., 2005; Schmittner et al., 2005; Meehl et al., 2007), in this case responding to fresher (due to increased precipitation) and warmer surface water conditions at high-latitudes (Meehl et al., 2007). In previous studies, future climate change projections are assessed either by comparison with control simulations with constant forcings (Gregory et al., 2005), or by using the past 150 years as a reference (Schmittner et al., 2005; Meehl et al., 2007). Extending the previous assessment to a period without remarkable human

* The main contents of this chapter are included in:
Ortega, P., M. Montoya, J. F. González-Rouco, J. Mignot and S. Legutke, 2011: Variability of the Atlantic meridional overturning circulation in the last millennium and two IPCC scenarios. *Clim. Dyn.* Accepted, DOI: 10.1007/s00382-011-1081-6

influence and natural radiative forcing compatible with the present climate would be however desirable. The past two millennia, also known as the "Late Holocene", are characterised by comparably weak changes in the radiative forcing, since important boundary conditions on climate such as the orbital parameters and the global ice mass have not changed substantially (Jones and Mann, 2004). This period, as the whole Holocene, is characterised by considerably smaller AMOC variations than the glacial era (Keigwin and Boyle, 2000). Evidence regarding the influence of natural forcing on the AMOC over the past millennia is controversial (Keigwin and Boyle, 2000; Broecker, 2000; Zorita et al., 2004; Lund et al., 2006; Stendel et al., 2006; Stenchikov et al., 2009; Swingedouw et al., 2010; Ottera et al., 2010). Likewise, the role of AMOC on climate variability is also uncertain, with some proxy reconstructions suggesting an amplifying role of the LIA conditions (Bond et al., 1997; Lund et al., 2006), and others finding no conclusive evidence (Keigwin and Boyle, 2000; Broecker, 2000).

This study intends to shed light on some of the aforementioned gaps, through the analysis of AMOC variability in two forced simulations of the last millennium (FOR1 and FOR2; see Chapter 2) and two future climate change scenario runs (A2 and B2; see Chapter 2). This suite of experiments provides a new perspective by which future projections of the ocean circulation can be placed in a longer time perspective. Also, the mechanisms responsible for the AMOC variability at interannual and longer time-scales are explored, and the corresponding impact of the different forcing factors is evaluated. For comparison, a 1000-year long control run (CTRL2, see Chapter 2) is also analysed.

The chapter is organised as follows: A first temporal and spatial intercomparison among simulations is addressed in Section 4.1. Sections 4.2 and 4.3 describe the main features of AMOC variability at interannual and interdecadal time scales, respectively. The AMOC response to the different forcing factors is presented in Section 4.4. Finally, the main conclusions are summarised in Section 4.5.

4.1 Climatology and temporal evolution of the AMOC

This section provides a first insight into the spatial and temporal features of AMOC variability in the different ECHO-G experiments.

4.1.1 The mean AMOC state

Figure 4.1 shows the mean of the AMOC streamfunction for the three long simulations (CTRL2, FOR1 and FOR2). All experiments exhibit a realistic circula-

tion, with maximum mean values comparable to NADW estimates of 15± 2 Sv (Ganachaud and Wunsch, 2000). The simulated AABW inflow into the Atlantic is in all cases below estimates of 5-8 Sv (Orsi et al., 1999; Ganachaud and Wunsch, 2000; Talley et al., 2003). Also, the NADW cell is generally deeper than indicated by recent observations (Talley et al., 2003) and other model climatologies (e.g. Dong and Sutton, 2005; Mignot and Frankignoul, 2005).

Deep water formation north of the Greenland-Scotland ridge (GSR) is negligible in CTRL2, and accounts for a GSR overflow of 2-3 Sv in FOR1 and FOR2. Yet, its strength is underestimated if compared to observations (6 Sv; Hansen and Østerhus, 2000; Olsen et al., 2008). The discrepancy among simulations points to differences in the properties of water masses in the North Atlantic. Indeed, the reservoir north of the sills is climatologically lighter in CTRL2, both due to fresher and warmer waters, exhibiting also less convective activity (not shown). Similar conditions are also observed in the scenario simulations (A2 and B2) and will be detailed in subsection 4.4.3. In contrast, in the forced experiments the overflow brings dense waters to the subpolar North Atlantic, contributing to a stronger AMOC below 1500 m.

4.1.2 Variability of the AMOC strength

The meridional overturning index (MOI*), first defined by Delworth et al. (1993) as the maximum value attained by the Atlantic meridional overturning streamfunction, is often employed to characterise the AMOC strength, since it is both intuitive and robust against changes in models and simulations (e.g. Delworth et al., 1993; Weaver and Valcke, 1998; Timmermann et al., 1998; Delworth and Greatbatch, 2000; Thorpe et al., 2001; Delworth et al., 2002; Gregory et al., 2005; Mignot and Frankignoul, 2005). In order to focus on decadal to multidecadal variability, Figure 4.2 shows the temporal evolution of a 11-yr running mean of the MOI in the five ECHO-G simulations. In broad terms, AMOC variations in FOR1 and FOR2 are within the range of variability in CTRL2. Besides, FOR1 tends to exhibit larger values than FOR2, as a result of their different initial stratification, given that all other factors are the same (Chapter 2). A common feature to both simulations is a weakening of the AMOC beginning with the industrial era that continues along the scenario simulations (Figure 4.2). By the last decade of the 21^{st} century, the MOI experiences a decrease of 35% in B2, and 42% in A2 relative to the mean preindustrial value in FOR1 (ca. 20 Sv). We will show in subsection 4.4.3 that this decrease is mainly caused by increased precipitation at

* Note that this definition is different to that considered in Chapter 3. Further description of the different overturning indices in literature is developed in the next subsection.

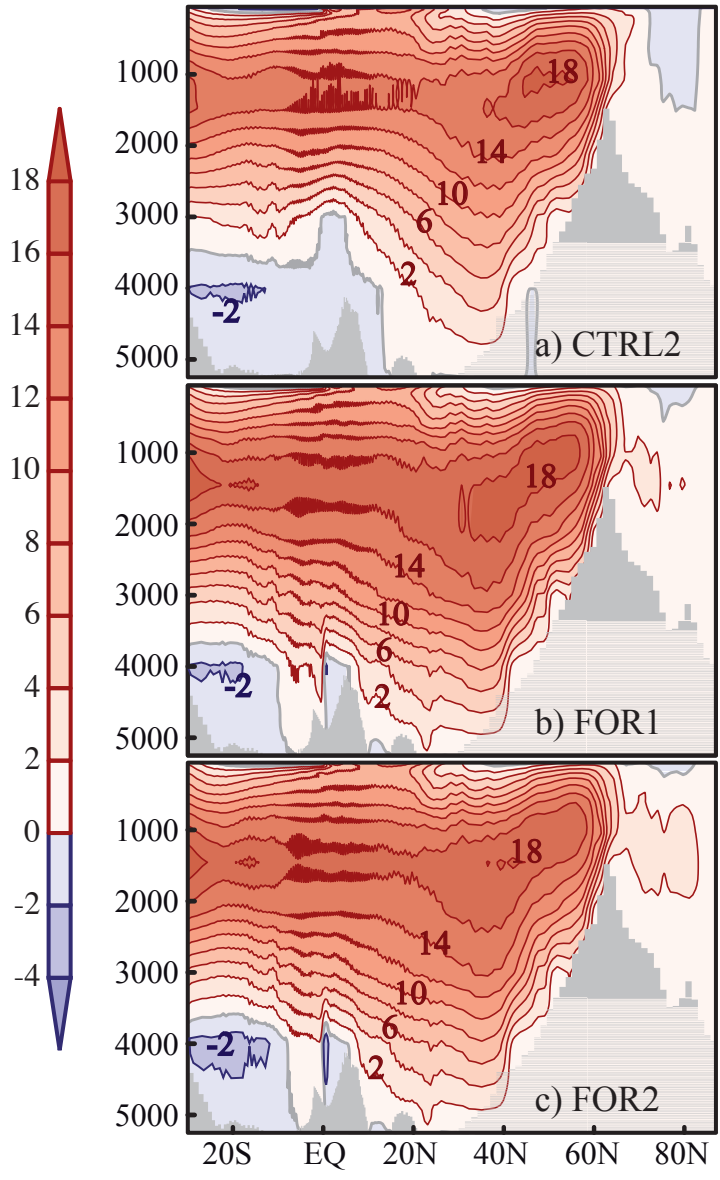

Fig. 4.1: Mean of the AMOC streamfunction (in Sv) for a) CTRL2, b) FOR1 and c) FOR2. Positive values of the streamfunction indicate clockwise circulation. Contour interval is 2 Sv.

high latitudes. The larger decrease in A2 seems reasonable, since this scenario is characterised by stronger emissions. This future response is most probably overestimated due to the lack of sulfate aerosols (Delworth and Dixon, 2006) in all the simulations.

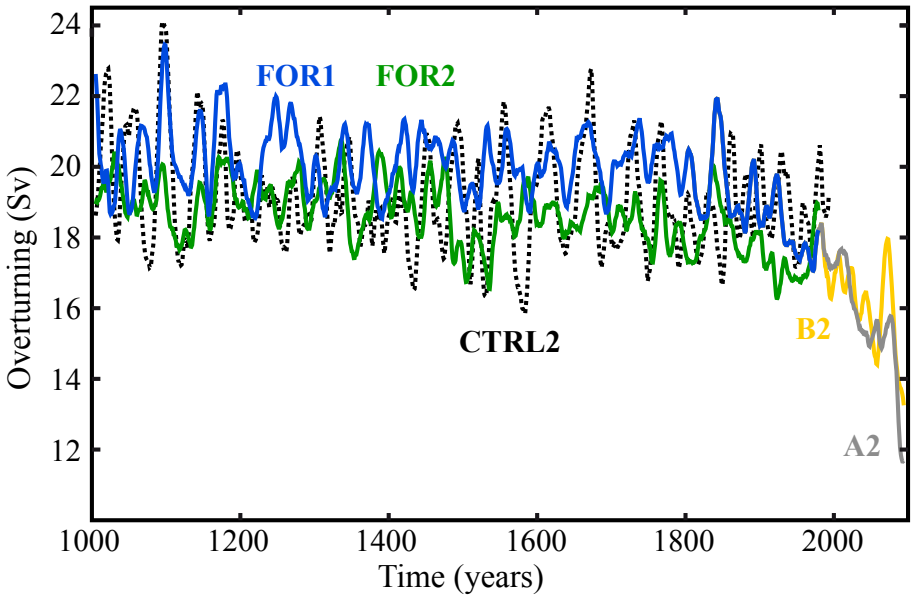

Fig. 4.2: Time series of the MOI (in Sv) in the Atlantic for CTRL2 (black dashed line), FOR1 (blue line), FOR2 (green line), A2 (grey line) and B2 (yellow line). The series are smoothed with an 11 yr running-mean filter.

Fourier spectra of the unfiltered MOI (Figure 4.3a) indicate that the AMOC behaviour is approximately described by a red-noise process in all three millennial simulations (note that the scenarios are excluded). Variance exceeds slightly that of a first order autoregressive process (AR1) at interannual and interdecadal time scales, suggesting that other processes than just the integration of synoptic weather noise by the ocean (Hasselmann, 1976) contribute to variability at these time scales. The peaks of variance are most clear in CTRL2, and less so in the forced runs (particularly at interdecadal timescales). The analysis of AMOC variability at both frequency ranges will be addressed separately in Sections 4.2 and 4.3. Finally, in the lowest frequencies (periods above 100 yr) the CTRL2 run

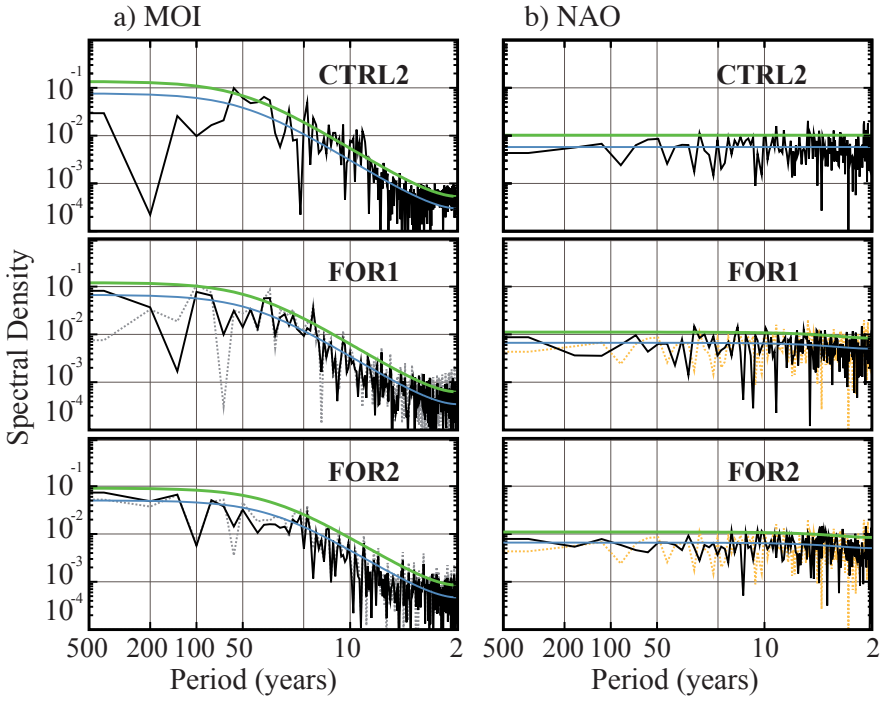

Fig. 4.3: Fourier spectrum of: a) the MOI and b) the NAO series in the simulations: CTRL2 (top), FOR1 (middle) and FOR2 (bottom). Black solid lines represent the spectrum for the complete simulations. In the forced runs, grey dotted lines correspond to the spectrum in the preindustrial period (1000-1800). In the right panel, orange lines reproduce the spectral values for CTRL2, to ease the comparison with the forced runs. Blue lines represent the spectrum of a red noise process with the same first autorregresive coefficient as the complete time-series, and green line sets the 90% confidence interval of this red-noise process.

presents relatively small spectral densities as compared to the forced runs, and also to its corresponding AR1 process. The larger values in FOR1 and FOR2 are possibly an indicator of some modulation from the external forcing at centennial timescales. This increased low-frequency MOI variability is partly explained by the AMOC weakening trend in the period 1800-1990, that accounts respectively for 29 and 8% of the total industrial variance in FOR1 and FOR2. Indeed, if the industrial period is excluded, spectral values in both simulations exhibit a general decrease at periods above 50 years (dotted grey lines in Figure 4.3a).

4.1.3 Analysis of the maximum AMOC location.

As indicated by Vellinga and Wu (2004) and Dong and Sutton (2005), the location at which the AMOC maximum is found varies with time, thus hindering the physical interpretation of the MOI variability. In order to assess the robustness of the MOI, the variability in the location of the maximum streamfunction value in terms of latitude and depth is analysed (Figure 4.4; results are shown only for A2 since those obtained for B2 are qualitatively very similar). In CTRL2 the location of the maximum is quite stable, oscillating in a small band of latitudes around 50°N and mainly confined to the 1050 m depth. Indeed, about one third of the time the temporal maximum occurs at the same location as the long-term mean maximum (47.4°N and 1050 m). In contrast, the forced experiments are characterised by the location of the AMOC maximum varying in a wider range of latitudes as well as depths. This suggests that the external forcing has a clear impact on the position of the maximum, even if both the latitude and depth at which the maxima occur are uncorrelated with the different forcing factors (not shown). Indeed, the position of the maximum exhibits some low-frequency modulation in the forced runs, not so clear in CTRL2. In both forced runs the maxima are found between 10°N and 56°N, while these are concentrated in a narrower latitudinal band in CTRL2. Also, FOR2 seems to exhibit some more latitudinal variability than FOR1. During the first centuries of FOR1 the maximum is more confined to latitudes from 36°N to 56°N, and only around 1800 AD this range seems to broaden. The main discrepancies between FOR1 and FOR2 are observed in depth. In FOR1, the maximum starts varying in a broad range of levels, from 1000 to 2100 m. These variations are shallower in FOR2, probably due to its different initial conditions. Indeed, FOR2 was started from year 1700 AD in FOR1, a period when the position of the maximum starts to become shallower, and varies at similar depths as in FOR2. This shoaling of the maximum continues through the last three centuries of FOR1, and becomes more important during the scenario simulations. In either case, both forced and unforced simulations exhibit changes in depth and latitude that seem to be correlated, with maxima located at lower (higher) latitudes more likely to occur at deeper (shallower) levels. This suggestion is supported by linear correlations between both quantities of -0.57, -0.67 and -0.74 for CTRL2, FOR1+A2 and FOR2, respectively.

Since the MOI is calculated as a maximum value, with its position varying in a wide region of the North Atlantic (Figure 4.4), its short-term variability averages the signal across different locations, thus hampering the identification of the possible mechanisms operating at smaller spatial scales (see Section 4.2). This limitation of the MOI has led some authors to consider alternative overturning indices. Vellinga and Wu (2004) fixed the latitude near the climatological maximum of the AMOC streamfunction to obtain a better representation of variability

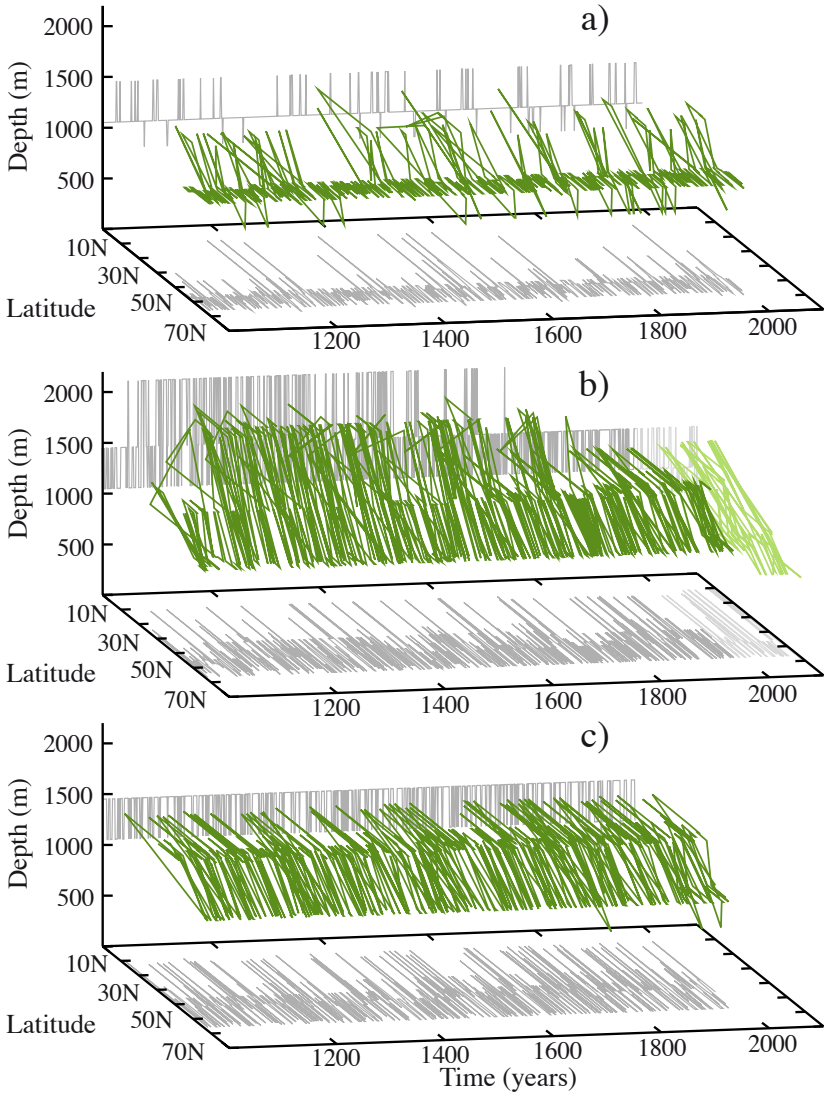

Fig. 4.4: Evolution of the position of the AMOC maximum in: a) CTRL2, b) FOR1+A2, c) FOR2. The green line describes in a three-dimensional plot the temporal variability of the location where the maximum AMOC takes place. The light grey lines represent the projections of the green line on the time-latitude and time-depth planes. Light colors in b) correspond to the evolution during the scenario simulation.

at interannual time scales. Similar definitions, with the overturning strength evaluated at fixed locations, have also been used in an attempt to link the AMOC variability to specific processes in the North Atlantic, such as convection in the Labrador Sea or NAO variability (Eden and Jung, 2001; Eden and Willebrand, 2001; Eden and Greatbatch, 2003) or to gauge its variability at the latitude of the RAPID ocean observation array (e.g. Baehr et al., 2008). Finally, another alternative is the use of empirical orthogonal function (EOF) and principal component (PC) analysis (e.g. Vellinga and Wu, 2004; Msadek and Frankignoul, 2009).

In the following, Sections 4.2 and 4.3 will address separately the high and low frequency variability in the AMOC. To analyse the high-frequency several local indices will be introduced in order to survey the different AMOC responses in the North Atlantic and identify the mechanisms responsible for these variations. In this way the diverseness of the local overturning short-term variability is better represented. The selection will be made within the locations where the AMOC streamfunction maxima have been found to take place in the simulations (Figure 4.4).

4.2 Mechanisms of high-frequency AMOC variability

The main goal of the following two Sections is to identify which mechanisms drive the AMOC variability in the ECHO-G model at high (i.e. interannual) and low (i.e. decadal to centennial) frequencies. Previous studies (Eden and Willebrand, 2001; Vellinga and Wu, 2004; Mignot and Frankignoul, 2005; Cabanes et al., 2008) suggest that surface atmospheric circulation dominates the AMOC interannual variability through changes in Ekman transport. Variance exceeding that of a red noise process in the shorter timescales (2-5 years) of the Fourier spectra (Figure 4.3a) also suggest a role of the atmospheric forcing. Such atmospheric forcing at high-frequencies would explain the fast variations observed in the location of the maximum (Figure 4.4). Thus, a correlation analysis between both the global atmospheric fields of SLP and wind stress, and a set of local overturning indices is performed. In order to sample the regions where the AMOC becomes more intense, only those locations where the AMOC streamfunction reaches a maximum value (Figure 4.4) were considered. The local AMOC time-series at these sites (ranging in number from 24 in CTRL2 to 22 in FOR2 and 30 in FOR1) were selected and high-pass filtered by removing variability at time scales longer than 10 yr. The filter method employed uses least squares coefficients to reduce Gibbs oscillations (Bloomfield, 1976) and is characterised by a sharp transfer window that allows an accurate selection of the different timescales.

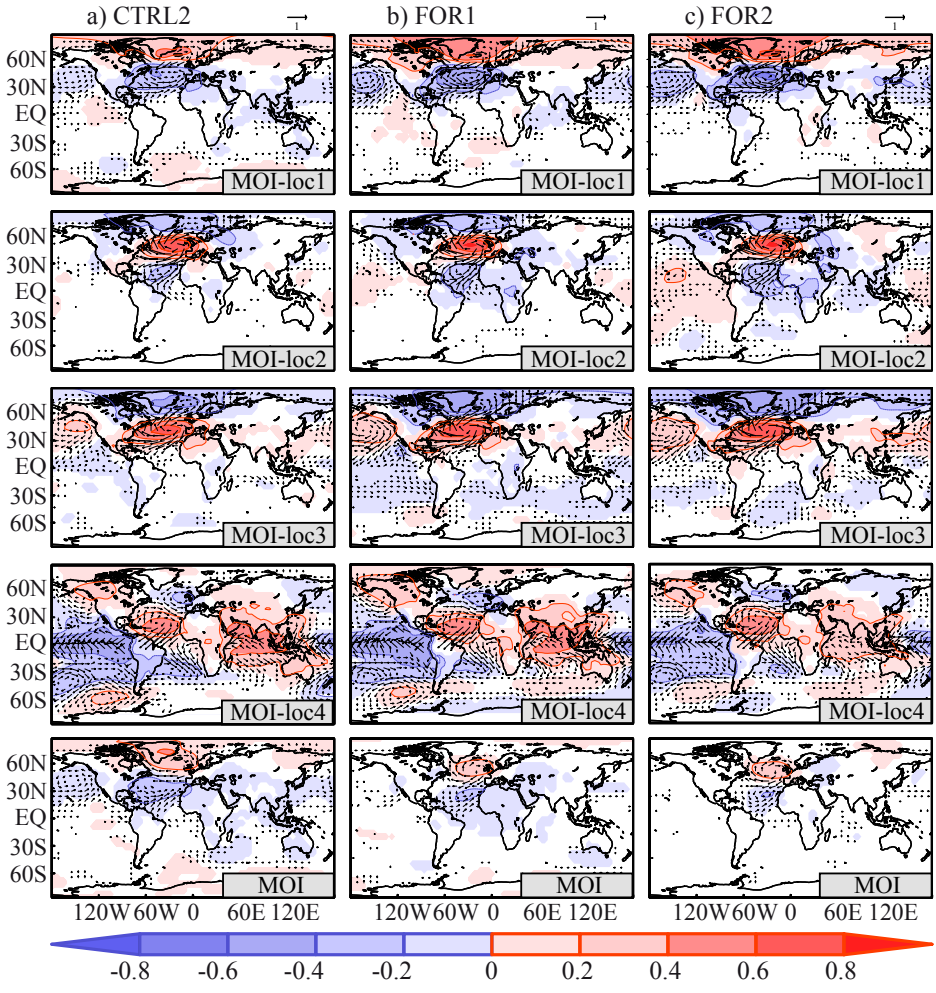

Fig. 4.5: Correlation maps of the local overturning indices (see Table 4.1) with SLP (shaded) and wind stress (vectors) anomalies. Data have been high-pass filtered for time scales below 10 yr. All correlation values are significant at a 0.05 level according to a Student's t test and accounting for the effective sample size by considering autocorrelation.

Table 4.1: Position of the local overturning indices used in Section 4.2

	MOI-loc1	MOI-loc2	MOI-loc3	MOI-loc4
Latitude (° N)	55.8	41.8	33.5	10.0
Depth (m)	1050	1450	2100	1450

Inspection of the correlation maps between the aforementioned surface atmospheric fields and the AMOC indices suggests the local series can be classified into four categories represented by the indices at only four locations (Table 4.1; note that the indices MOI-loc1 to MOI-loc4 are ordered by decreasing latitude). Their associated atmospheric patterns are shown in Figure 4.5. Correlations with the MOI (Figure 4.5, last row) generally exhibit a weaker signal than those with locally defined indices. This result is to be expected due to the integration by the MOI of different local influences across the North Atlantic basin. Here, as in the remainder of the text, statistical significance of all the regression/correlation coefficients is assessed following a Student's t test. The sample size is corrected by taking into account the series autocorrelation, thus reducing the sample degrees of freedom to its effective value (Bretherton et al., 1999). Correlation values are maximum at lag 0, and drop substantially at other lags (not shown), thus showing evidence of a fast overturning response to the atmospheric forcing at high-frequencies.

The opposing phases of a zonally extended NAO-like SLP pattern (e.g. Wallace and Gutzler, 1981) are identified for both MOI-loc1 and MOI-loc3. At midlatitudes, represented by MOI-loc2, the overturning variability is linked to an intense anticyclonic cell centred north of the Azores islands (around 55°N and 30°W) that introduces a west-east gradient over western Europe, and is accompanied to the south by a band of negative pressure anomalies. These are the main features described for the negative phase of the East Atlantic (EA) Pattern by Barnston and Livezey (1987). The negative anomalies across Greenland and the Nordic Seas, as opposed to the positive cell at midlatitudes, indicate that some weak contribution from the NAO may also be present. MOI-loc4 is the only index defined at tropical latitudes and is associated with a large-scale pressure pattern with a noticeable signal in the tropical Pacific, that is likely evidencing the influence of ENSO variability (e.g. Trenberth and Shea, 1987). The model's performance to reproduce both ENSO and NAO variability has been previously analysed in CTRL1 (Min et al., 2005b). Overall, both indices are well represented as compared to observations and other model simulations. The occurrence of ENSO is however too frequent, and its amplitude too large. The main NAO bias is an overestimation of its impact over the Pacific sector. Likewise,

the centers of action of the EA pattern (Figure 4.5, second row) are in general good agreement with those observed in other models (e.g. Fig 3b in Msadek and Frankignoul, 2009). Linear correlations (Table 4.2) support the observed links between the MOI-loc4 and ENSO, between the NAO and both MOI-loc1 and MOI-loc3, and also between MOI-loc2 and the EA timeseries. In addition, all simulations show weaker but significant contributions from the NAO to MOI-loc2 variability, as well as from the EA to the MOI-loc4. Interestingly, all local indices show similar correlation patterns in the three millennial experiments, and also similar correlations with the main teleconnection indices. For the sake of briefness, the analysis in high-frequencies will continue focused exclusively on the CTRL2 run, with results for the other runs leading to similar conclusions.

Table 4.2: Correlations between the high-pass filtered (periods $\leq$ 10 yr) local overturning indices and the indices of the main teleconnection patterns (see also Fig. 4.5). Values in bold represent correlations significant at the 0.05 level according to a Student's t test that takes into account the series autocorrelation to calculate the sample size.

		MOI-loc1	MOI-loc2	MOI-loc3	MOI-loc4
ENSO	CTRL2	-0.06	0.01	0.07	**0.49**
	FOR1	-0.04	-0.02	**0.09**	**0.49**
	FOR2	-0.01	**-0.11**	0.02	**0.38**
NAO	CTRL2	**-0.42**	**0.16**	**0.51**	0.05
	FOR1	**-0.64**	**0.15**	**0.64**	-0.04
	FOR2	**-0.65**	**0.11**	**0.68**	0.07
EA	CTRL2	-0.04	**-0.58**	-0.06	**0.25**
	FOR	0.03	**-0.64**	-0.01	**0.30**
	FOR2	**-0.10**	**-0.59**	0.08	**0.27**

The underlying mechanism for the overturning response to the former teleconnection patterns (i.e. NAO, ENSO and EA) is now explored (Figure 4.6). The large-scale patterns modulate the zonal wind at different latitudes, thereby inducing local changes in the meridional Ekman transport. Figure 4.6 shows the spatial extension of AMOC changes (bottom panels) in the context of the zonal wind variations (top panels) associated with each teleconnection index. Note that, in the Northern Hemisphere, easterlies force northward and westerlies southward meridional transport, while transports are reversed in the Southern Hemisphere. In broad terms, the surface wind forcing is found to generate deep,

latitudinally narrow and relatively local overturning cells. In the case of the NAO (Figure 4.6a), easterlies around 30°N force surface transport to the north, while westerlies near 50°N force southward transport. Convergence of water masses at 43°N results in local downwelling, thus originating two overturning cells of opposite sign. This is consistent with the fact that MOI-loc1 and MOI-loc3 lie in the regions with largest negative and positive anomalies, respectively. This pattern with opposing cells and downwelling near 40°N resembles the instantaneous ocean response to the NAO first described by Eden and Willebrand (2001) and also found in later studies (Vellinga and Wu, 2004; Mignot and Frankignoul, 2005; Deshayes and Frankignoul, 2008). The pattern associated with ENSO (Figure 4.6b) is characterised by a large overturning cell confined to the tropical Atlantic, consistent with the first EOF obtained by Vellinga and Wu (2004) at interannual time scales, which they also relate to El-Niño variability. In this case, the overturning cell is wider in latitude, as a response to the combined effect of westerlies to the south and easterlies to the north of the Equator, both forcing northward meridional mass transport. Obviously, only the index defined in the Tropics (MOI-loc4) is well placed inside the resulting overturning cell. Finally, and similarly to the NAO, the EA pattern is also linked to a dipole of narrow overturning cells (Figure 4.6c), but more displaced to the south than those in Figure 4.6a, given the influence of zonal winds further south. The regions with the largest positive and negative overturning anomalies map over the locations where MOI-loc4 and MOI-loc2 were defined, as expected after correlations in Table 4.2.

Our results confirm the influence of local atmospheric circulation on the AMOC interannual variability. The fact that the results are common in CTRL2 and the forced runs (Figure 6, Table 2) furthermore suggests that at high frequencies changes in external forcing factors have no clear influence on the AMOC variability. In the next Section the prominent features of the AMOC variability on longer time scales are explored.

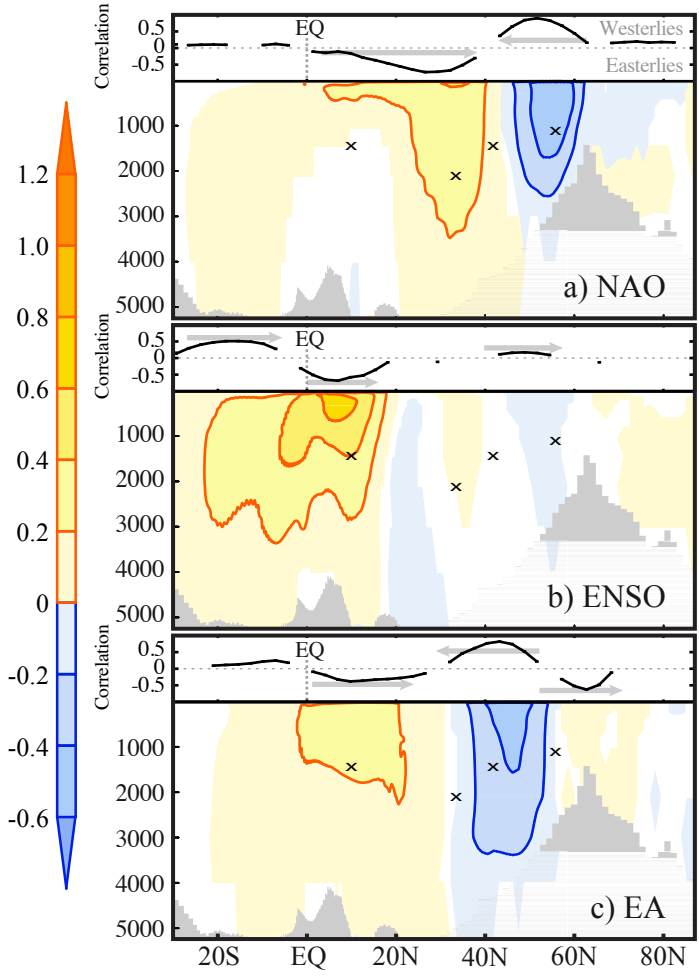

Fig. 4.6: Analysis of high-frequency wind-driven AMOC changes in CTRL2. *Upper panels:* Correlation values of the zonally averaged zonal wind-stress with the indices: a) NAO, defined as the difference between normalised SLP anomalies at the closest gridpoints to Azores and Iceland; b) ENSO, calculated as the 1^{st} PC of SST in the tropical Pacific; c) EA, computed as the 3^{rd} PC of SLP in the North Atlantic. Arrows indicate the direction in which the meridional Ekman transport is produced. *Lower panels:* Regression maps between the AMOC streamfunction (in Sv), and the previous indices. The crosses mark the location where the local overturning indices are defined (note that MOI-loc1 to MOI-loc4 are ordered by decreasing latitude). Data filtering and significance is considered as in Fig. 4.5.

4.3 Low-frequency AMOC variability

This Section focuses on complementary timescales to those considered in Section 4.2, i.e. periods above 10 years. At low frequencies, the MOI is related at lag 0 to overturning variability over the whole Atlantic basin for each of the long simulations (Figure 4.7, third row). Although the highest regression coefficients are found in the NADW formation region, common basin-scale variability is found from the North Atlantic to the Equator, indicating that at these timescales the MOI gauges the variability of the entire AMOC cell.

The development of these basin-scale anomalies begins in the NADW formation region (Figure 4.7, top panels), and takes place gradually over several years, attaining its maximum values at lag 0. Indeed, the low-pass filtered MOI is significantly autocorrelated for lags up to 5-8 years (Figure 4.7, bottom panels). These autocorrelations are also significant for the unfiltered index (not shown), thus supporting a predominant AMOC mode at interdecadal timescales. Similar slowly-developing MOC variations have been observed in the context of some ocean oscillatory modes in other models (e.g. Timmermann et al., 1998; Dong and Sutton, 2005; Hawkins and Sutton, 2007). In the ECHO-G simulations, a thorough understanding of this AMOC mode would require a complete description of the mechanisms and cycles involved that is beyond the scope of this study. In the following, a first insight on the mechanisms behind the AMOC strengthenings is given instead.

At the low-frequencies, most of the mechanisms described (e.g. Timmermann et al., 1998; Dong and Sutton, 2005; Mignot and Frankignoul, 2005; Hawkins and Sutton, 2007) relate the AMOC variations to changes in North Atlantic deep convection. Thus, in order to investigate the mechanism responsible for interdecadal AMOC variability, the link between the MOI and the variability of the mixed layer depth (MLD) in the long simulations is explored (Figure 4.8, left column). The analysis shows that positive MOI variations are preceded by increased activity south of Greenland, with maximum correlation coefficients for a leading time of 4 years. Likewise, recent analyses with both observations and regional modelling (Bacon et al., 2003; Moore, 2003; Pickart et al., 2003) suggest that deep convection events in the Irminger Sea may be forced by a so-called Greenland tip jet that enhances heat loss through both fairly localised air-sea heat flux and strong wind-stress curl. A similar mechanism seems to be taking place in the ECHO-G simulations, in spite of the relatively coarse resolution of this model. Indeed, the correlation maps in Figure 4.8 (right column) show that increased convection is taking place in a context of negative winter SLP anomalies over Greenland, along with intensified westerlies from the Labrador to the Irminger Seas, and increased wind-stress curl southeast of Cape Farewell. This general picture is also compatible with the ocean response to NAO variability

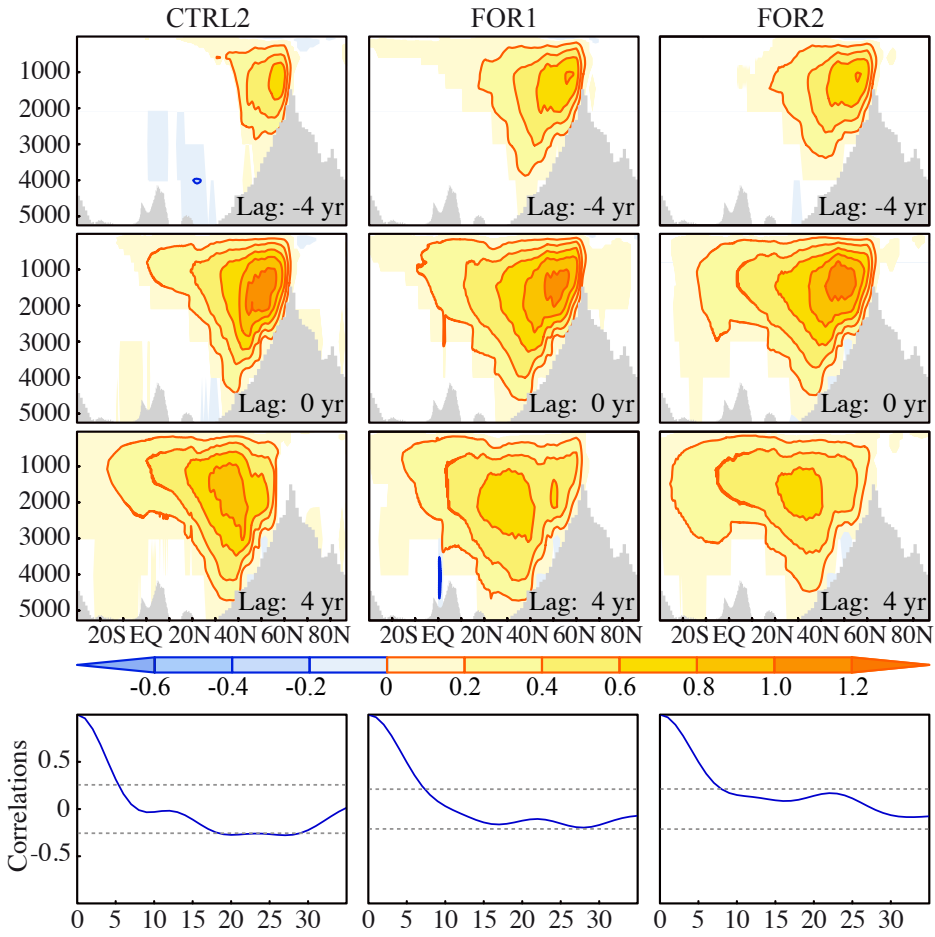

Fig. 4.7: *Top:* Lag-regression maps between the low-pass filtered maximum overturning strength and the anomalies of the AMOC streamfunction (in Sv) in CTRL2 (left), FOR1 (middle) and FOR2 (right). Positive (negative) lags indicate that the streamfunction pattern lags (leads) the MOI timeseries. *Bottom:* Autocorrelation of the low-pass filtered MOI times series (periods above 10 yr). The horizontal dashed lines delimit significance at the 0.05 level. In all panels significance is assessed as in Fig. 4.5.

described by Deshayes and Frankignoul (2008), in which the NAO was found to drive Irminger convection through anomalous Ekman pumping over the region.

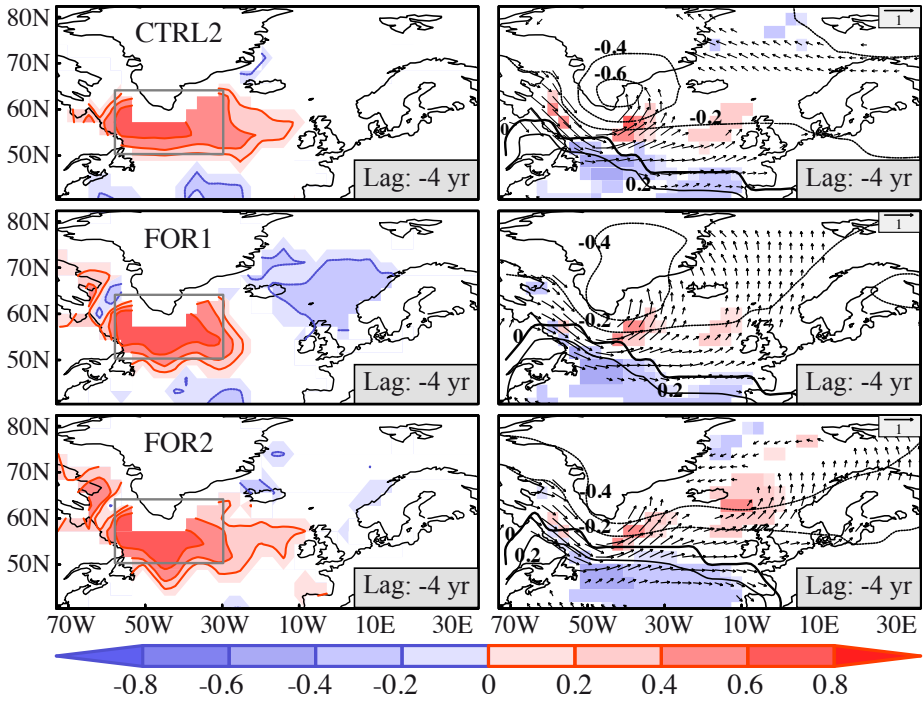

Fig. 4.8: Lag correlation maps between the MOI and: (*left*) the winter (January-February-March) anomalies of the mixed layer depth in the 3 long simulations; (*right*) the winter means of the wind stress (vectors), the wind stress curl (shaded) and the SLP anomalies (contours). Filtering and significance is considered as in Fig. 4.7. The lag-correlations are calculated with the MOI lagging by 4 years, since this lag is associated with the largest correlation coefficients. The grey rectangle encloses the region where variables in Fig. 4.9 are averaged. The contour interval for correlations with the SLP is 0.2.

To identify the precursors for deep water formation the rest of the analysis is performed focusing on convection south of Greenland. Figure 4.9 shows lead-lag cross-correlations between the mean mixed layer depth anomalies in the convection regions near Cape Farewell (grey box in Figure 4.8) and the aver-

ages of other variables in the same region. The MOI is found to lag the changes in convection by 4 years (dashed line in Figure 4.9) in consistency with Figure 4.8. The possible role of different quantities to foster convection is now explored (Figure 4.9). No leading contribution on convection is found for either the averages of heat and freshwater fluxes (both precipitation and evaporation), the surface atmospheric temperature, or the mean ocean temperature and salinity values at different depths (not shown). Most interestingly, variations of the zonal wind-stress do precede by about 1 year the changes in convection.

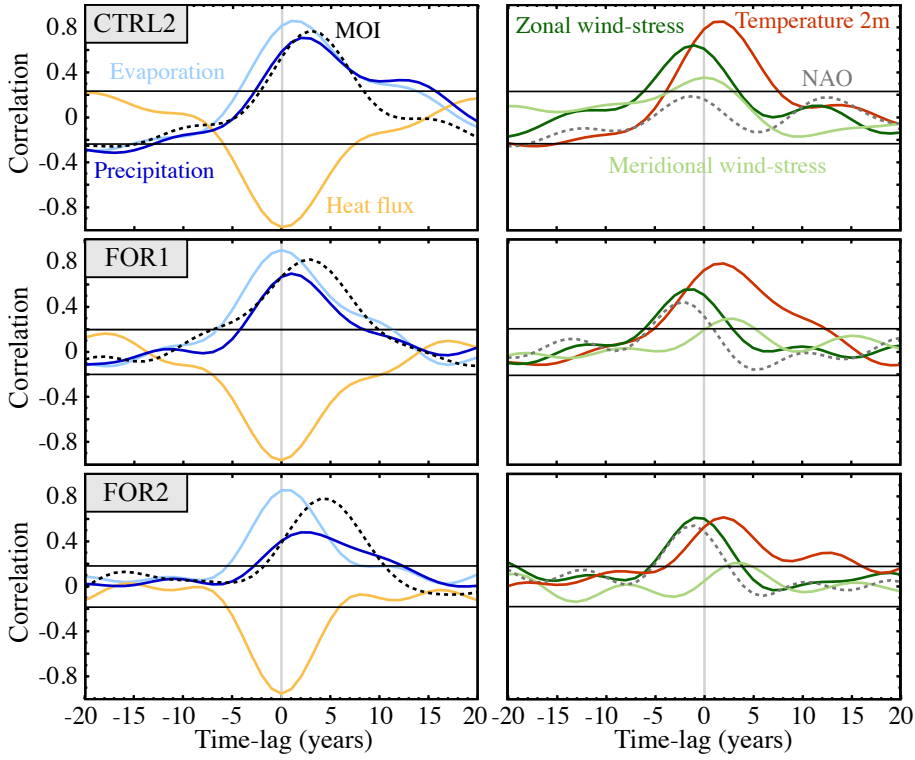

Fig. 4.9: Time-lag correlations of the mean convection depth in Labrador (grey box in Fig. 4.8) with the local averages of the main fluxes (left) and atmospheric variables (right) over the region. Correlations with the MOI and the NAO (dotted black and grey lines, respectively) are also shown. Horizontal black lines delimit significance at the 0.05 level. Filtering and significance are considered as in Fig. 4.7. Positive (negative) lags indicate that convection is leading (lagging).

Hence, the atmosphere appears, again, as the main source of low-frequency changes in convection, which leads in turn the AMOC changes. In the forced runs, these atmospheric variations seem to be ultimately forced by the NAO, with a lead time of 1-2 years (grey dashed line in Figure 4.9, right panels). In the CTRL2 run, the contribution of the NAO is not significant. To understand this different influence the spectral and spatial features of the NAO are investigated. A Fourier analysis of their respective timeseries shows some enhanced low-frequency NAO variability in the forced runs with respect to CTRL2 (black and orange lines in Figure 4.3b). Some differences are also observed in the NAO spatial configuration. The latitudinal SLP gradient is stronger in the forced runs (Figure 4.10), which also shows anomalous low pressures over Greenland. Both changes are accompanied by increased westerlies over the North Atlantic and intensified Greenland tip jet, which has been shown to drive Labrador convection, and thereby the AMOC. Other studies support the role of positive NAO phases to favour deep convection events in both the Labrador (Dickson et al., 1996; Guemas and Salas-Mélia, 2008) and Irminger Seas (Pickart et al., 2003; Deshayes and Frankignoul, 2008). These results suggest spatial SLP changes in FOR1 and FOR2 are being forced through the effect of the external forcing (both natural and anthropogenic) on tropical and subtropical SSTs, which can potentially impact the NAO (e.g. Rodwell et al., 1999; Peng et al., 2005). Given the impact of external forcing on atmospheric variability and the NAO in particular, and by extension its possible modulation of AMOC variability in FOR1 and FOR2, the following Section investigates the specific AMOC response to each forcing factor.

4.4 AMOC response to the external forcing

While most models predict a slowdown of the overturning strength in response to increasing GHG concentrations (Schmittner et al., 2005; Schneider et al., 2007), the effect of the comparatively moderate radiative forcing (i.e. volcanic aerosols and solar irradiance) on the AMOC variability has received less attention and is less clear (e.g. Zorita et al., 2004; Stendel et al., 2006; Stenchikov et al., 2009; Swingedouw et al., 2010; Ottera et al., 2010).

A preliminary analysis, focusing on the preindustrial era to omit the predominant effect of greenhouse gases is carried out in order to investigate the linear relationships between the natural forcing factors and the MOI. Neither the solar irradiance nor the radiative effect of volcanic aerosols are significantly correlated with the MOI, either at lag 0 (Table 4.3) or at other lead-lag times (not shown). Moreover, the effective solar constant, that accounts for the combined effect of both forcing factors, appears also unrelated to the changes in the MOI. Similar results, excluding a significant linear response of the AMOC to both the slowly

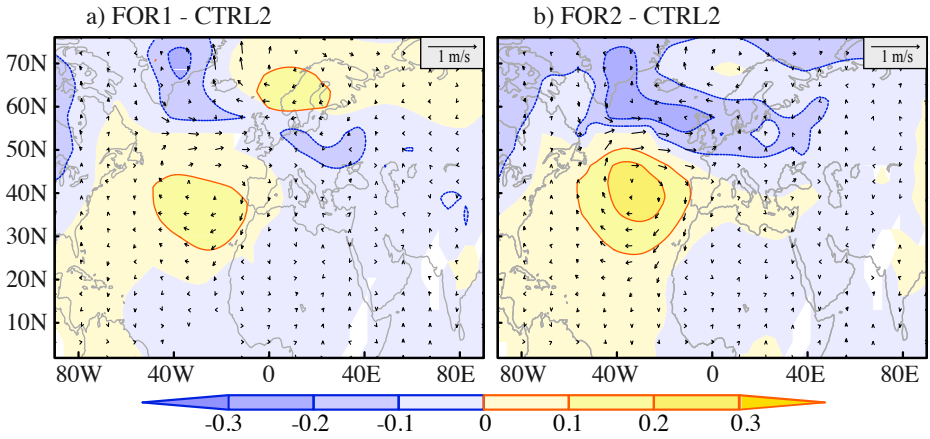

Fig. 4.10: Differences between the NAO regression patterns in: a) FOR1 and CTRL2; b) FOR2 and CTRL2. For each run, NAO is regressed with the anomalies of SLP (shaded, in hPa) and the surface wind (vectors, in m/s), and significance is assessed as in Fig. 4.5.

changing radiative forcing and the fast-varying volcanic aerosols, are also described by Hofer et al. (2011) for several transient simulations covering the last millennium.

Table 4.3: Correlations between the natural forcing and the MOI during the preindustrial period (1200-1850). Note that none of these values is significant at the 0.05 level according to a Student's t test that takes into account the series autocorrelation to calculate the sample size.

	Volcanic forc.	Solar forc.	Sol+Volc. forc.
FOR1	0.08	0.02	0.08
FOR2	-0.04	0.10	-0.01

There is, however, an obvious need to improve the analysis, taking also into account the particularities of each forcing factor. The main changes of the AMOC and other ocean quantities related in response to each natural and anthropogenic forcing factor are investigated separately in the following subsections.

4.4.1 Impact of solar irradiance

Studies addressing the impact of solar variability analyse the climate conditions during the Little Ice Age and, in particular, the Maunder Minimum (Rind et al., 2004; Zorita et al., 2004). These are periods characterised by a weak insolation (Figure 2.2), but also remarkable volcanic activity. The actual role of the AMOC during this period remains unclear, with some studies showing little sensitivity (e.g. Zorita et al., 2004; Stendel et al., 2006), while others suggest a weakening (Cubasch et al., 1997; Broecker, 2000; Lund et al., 2006; Sedláček and Mysak, 2009a,b) or even a strengthening of the AMOC during low solar forcing conditions (Swingedouw et al., 2010). In contrast, there is more consensus regarding the main atmospheric conditions in the North Atlantic. Models show a general tendency to produce negative NAO phases during periods of low radiative forcing (Shindell et al., 2001; Rind et al., 2004; Zorita et al., 2004; Gouirand et al., 2007b; Swingedouw et al., 2010) that may have an impact on the ocean. Indeed, Zorita et al. (2004) show that these predominant low NAO phases lead to a weakening of the Gulf stream through a modulation of the wind-stress forcing (Zorita et al., 2004).

In the ECHO-G simulations, estimates of solar irradiance (Figure 2.2) show a remarkable drop in solar activity from the MCA (ca. AD 1100-1300) to the beginning of the LIA (ca. AD 1400-1600). Although both periods are also punctuated by the effect volcanism, the main radiative difference can be assumed to be solar related. The significance of the AMOC changes associated to this decrease in total insolation is established by comparison with natural unforced variability. The AMOC change from the LIA to the MCA is studied by calculating the differences between the 200 year long periods defined above. Its significance is analysed by randomly extracting 1000 comparable non-overlapping periods of 200 yrs in CTRL2 and calculating their respective differences. This provides a metric of the largest possible change related to solar forcing in the forced simulations compared to internal variability in CTRL2. Only those values above the 97.5th or below the 2.5th percentiles are shown (Figure 4.11a.). Overall, the AMOC changes tend to be insignificant at the surface and also near the DWF region. The largest significant values are located at depth near the Equator, although with opposite sign in FOR1 and FOR2. At this location remarkable changes in both temperature and salinity are also observed (not shown). Since the deep ocean needs long time to reach thermal and haline adjustment, the different starting conditions in FOR1 (relatively warm) and FOR2 (relatively cold) can therefore explain the opposite AMOC changes in depth, pointing to too short a spin up period to achieve equilibrium at large depths. All these findings are difficult to reconcile with a meaningful solar impact on the AMOC.

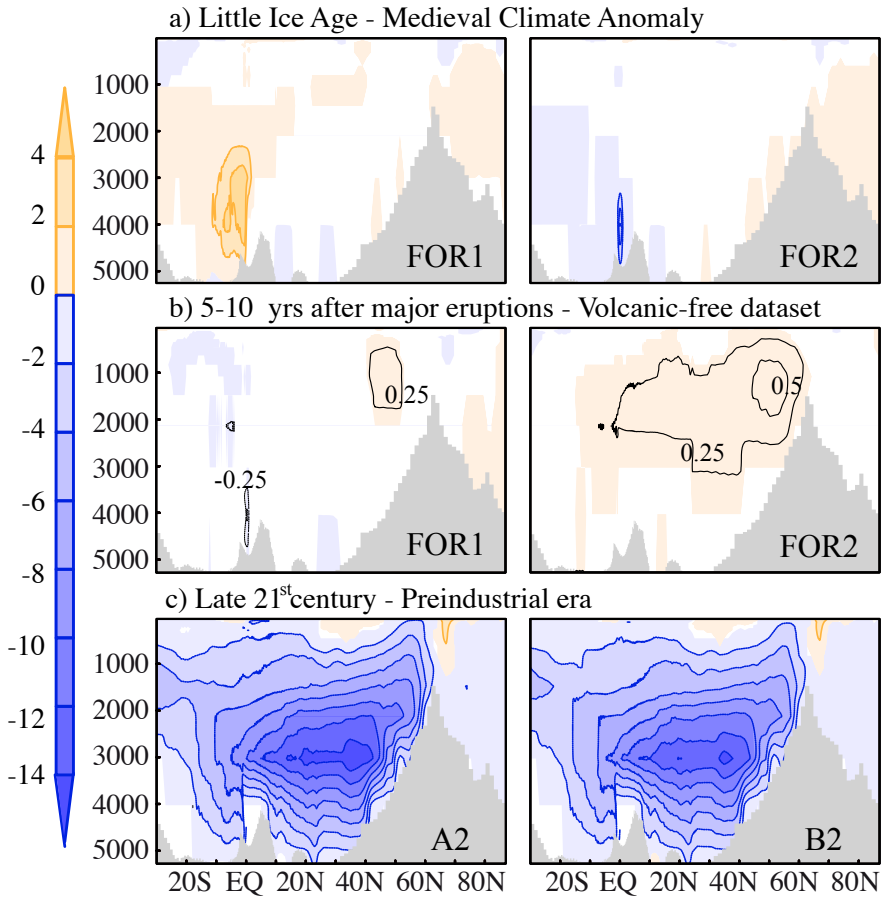

Fig. 4.11: Composites of the AMOC (in Sv) calculated as a) The difference in means between the Little Ice Age (1400-1600) and the Medieval Climate Anomaly (1100-1300), b) The average of preindustrial anomalies from years 5 to 10 after the 15 largest preindustrial eruptions, c) The difference in means between the late 21^{st} century (2070-2100) and the preindustrial era (1100-1850). Composites are shown for FOR1 (left) and FOR2 (right) in a) and b), and for both A2 (left) and B2 (right) with respect to FOR1 in c). Black contours in b) account for AMOC changes in increments of 0.25 Sv. Significance is assessed at the 0.05% level by comparing with the 2.5 and 97.5 percentiles in three different ensembles: a) 1000 pairs of non-overlapping 200 year long periods in CTRL2, b) 1000 random selections of 15 years from a preindustrial volcanic-free dataset, c) the 721 different 31 year long periods throughout the preindustrial era.

The general ocean response to the solar forcing is also explored. To isolate the signal of solar variability, disregarding the contribution from volcanoes, the following study is based on different linear regressions with the standardised solar irradiance (Figure 4.12). The sign of the solar index has been reversed to show results corresponding to a decrease in the solar activity (as occurred during the LIA). This new approach produces similar results for the AMOC to those in Figure 4.11a (not shown). The reasons for the poor AMOC response to solar forcing are investigated through the analysis of other ocean quantities.

In both runs, surface salinity increases in the Arctic following an increase of the sea ice thickness that removes in turn fresh-water from the surface (Figure 4.12a). However, the changes in salinity are rather weak and occur far from the Labrador and Irminger Seas, the region in the model that dominates deep water formation. The main response to the radiative cooling is observed for the SSTs (Figure 4.12b), which shows a global pattern of negative anomalies, more intense in the Tropics. Yet, the anomalies in the vicinity of the Labrador Sea are also negligible. The most conspicuous disagreement between simulations is related to the atmospheric response (Figure 4.12c). While FOR1 exhibits no significant changes, FOR2 shows a SLP pattern that has some resemblance to a negative phase of the NAO, introducing anomalous easterlies near Cape Farewell. However, the changes in wind-stress are not intense enough to affect Labrador and Irminger Sea convection, as becomes apparent in Figure 4.12d. As a result, significant changes of winter convection are weak and mainly localised in the Norwegian Seas. This explains the little sensitivity of the AMOC to the solar variability, and in particular the fact that we find no response at the LIA. A similar picture arises for the ocean lagging the solar variations for up to 20 years (not shown).

4.4.2 Influence of volcanic activity

Unlike the solar irradiance changes, that range from decadal to multi-centennial timescales during the last millennium, volcanic aerosols have a relatively short-lived strong impact on the radiative forcing. The associated cooling signal can penetrate deep into the ocean, influencing the ocean thermal structure, and potentially producing low-frequency changes on global quantities, such as the ocean heat content, or the thermal expansion (Gleckler et al., 2006a,b). The particular ocean response to the 1815 Tambora and 1991 Pinatubo eruptions has been assessed by Stenchikov et al. (2009) using the GFDL model. Besides long-lasting changes in the ocean heat content and steric height, both major eruptions have been found to produce a 10% increase in the strength of the AMOC, triggered by enhanced convection favoured by denser conditions in the upper ocean. An

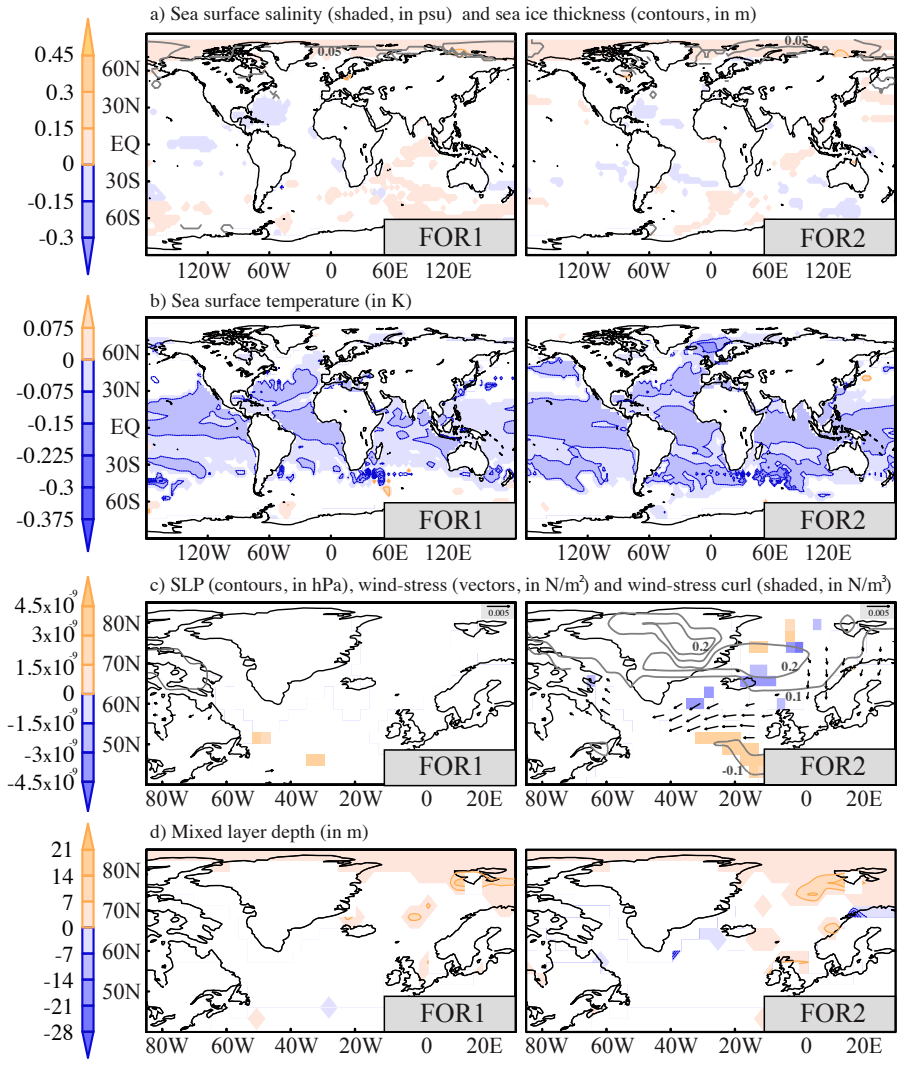

Fig. 4.12: Linear regressions during the preindustrial period (1200-1850) between the negative and standardised index of solar irradiance and the oceanic variables: a) annual sea surface salinity (shaded, in psu) and winter sea ice thickness (contours, in m), b) annual SST (in K), c) annual SLP (contours, in hPa), wind stress (vectors, in N/m^2) and wind stress curl (shaded, in N/m^3), d) winter mixed layer depth (in m). Significance is assessed as in Fig. 4.5. Solar irradiance was reversed to show the patterns corresponding to a decrease in solar activity.

overall AMOC increase is also observed in response to large tropical eruptions in the Bergen climate model (Ottera et al., 2010).

The non-linear episodic influence of volcanoes cannot be properly captured by the regression analysis applied to solar variability. Hence, a composite analysis is employed instead. The overall effect of volcanoes is characterised during the 15 largest preindustrial eruptions, their radiative forcing being at least half as large as for the 1815 AD Tambora eruption. To represent the periods without volcanic forcing, a volcanic-free dataset is defined that includes all the 237 years not preceded by a volcanic eruption in the previous decade. This latter choice is motivated by the fact that the analysis reveals that the volcanic fingerprint is almost negligible 10 years after the eruptions in both FOR1 and FOR2.

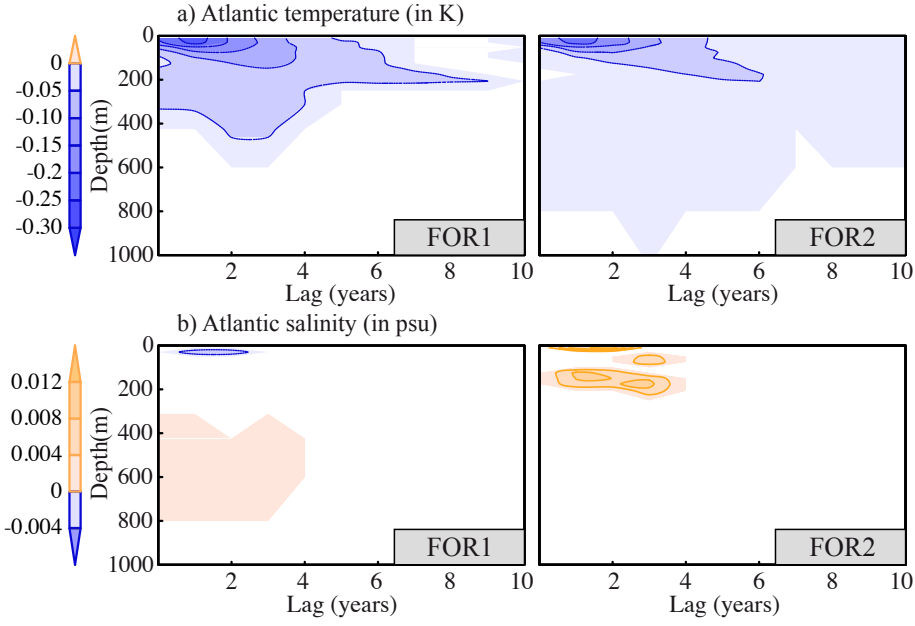

Fig. 4.13: Composites of the averaged preindustrial anomalies following the onset of the 15 largest preindustrial eruptions. The depth profiles of the following variables are explored: a) Atlantic mean temperature (in K), b) Atlantic salinity (in psu). Significance is assessed as in Fig. 4.11b.

The composite maps in Figures 4.11b, 4.13 and 4.14 are calculated as the average of preindustrial anomalies in the volcanic dataset, using a Monte Carlo

test to assess significance. The reference Monte Carlo ensemble is computed by random selection of 15 years from the volcanic-free dataset. 1000 different realizations are performed. As in the previous subsection, composite values are not significant if they fall within percentiles 2.5th and 97.5th of the ensemble. Figure 4.11b shows the averaged AMOC response from years 5 to 10 after the volcanic eruptions. Similarly to Stenchikov et al. (2009) and Ottera et al. (2010), and in contrast with the linear correlations in Table 4.3, a small but significant increase of the AMOC is found in the NADW formation region. Moreover, in the case of FOR2, positive streamfunction values up to 0.5 Sv are found all across the Atlantic basin. The analysis of other quantities help to understand how they develop.

The depth penetration of the volcanic signal is evaluated for temperature and salinity. Figure 4.13a shows that the cooling in the Atlantic ocean reaches down to 600 m in FOR1 and 1000 m in FOR2, with the largest significant values in the upper 200 m. The impact on salinity is clearly smaller, and mainly localised in the upper 50 m (4.13b). In terms of latitude, the cooling is more important near the subtropics (Figure 4.14a), with the most persistent negative anomalies occurring north of 55°N. North Atlantic convection is favoured by increased upper salinity, mainly caused by a rise in sea ice thickness at high latitudes (Figure 4.14b). Both cooling and salinification contribute to denser conditions near the surface, thus leading to a slight increase in mixed layer depth both in the Nordic Seas (north of 63°N, Figure 4.14c), and, to a lesser extent, in the Labrador and Irminger Seas (south of 63°N, Figure 4.14c), which may explain the small strengthening of the AMOC. Unlike in Ottera et al. (2010), there is no significant NAO response to volcanoes (not shown), and therefore no wind-stress contribution to convection (vectors in Figure 4.14c). This may explain the smaller AMOC changes in the ECHO-G model.

4.4.3 The fingerprint of increasing GHGs.

The large sensitivity of climate models to increasing GHGs emerges from the fact that its radiative effect is both strong (unlike for the solar forcing) and long-lasting (unlike for volcanic aerosols). Most climate change projections are characterised by a decrease in surface density in the North Atlantic, due to the combined effect of increased precipitation and surface warming (Rahmstorf and Ganopolski, 1999; Cubasch et al., 2001; Gregory et al., 2005; Meehl et al., 2007). In response to the lighter waters NADW formation is weakened, and therefore the AMOC.

The impact of increasing GHG concentrations is analysed computing the difference in means between the last 31 years of the future projections (when the

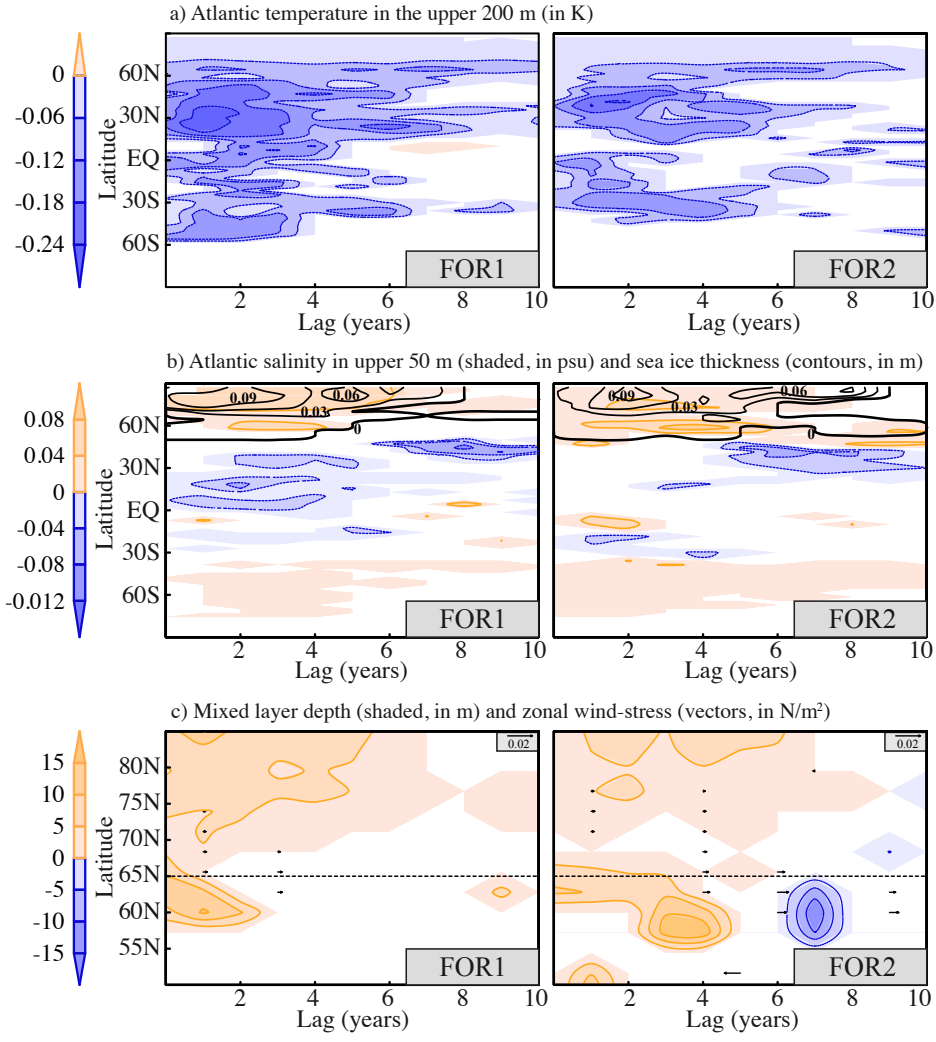

Fig. 4.14: The same as in Fig. 4.13 but for the following zonally averaged variables: a) Atlantic temperature upper 200 m (in K), b) Atlantic salinity upper 50 m (shaded, in psu) and Sea Ice Thickness (black contours, in m), c) Mixed layer depth (shaded, in m) and zonal wind-stress (vectors, in N/m^2). The black dashed lines in c) indicate the latitude of the sills, thus separating the two main regions of convection.

GHG forcing is larger) and the preindustrial era, that can be assumed to incorporate only natural forcing changes. Significance is assessed by comparing these differences to the percentiles 2.5th and 97.5th of a new preindustrial ensemble. This time, each member is calculated as the average of the preindustrial anomalies in a period of 31 years. There is a total of 721 different such periods throughout the preindustrial era. Due to the strong forcing, most of the differences turn out to be significant (Figures 4.11c, 4.15 and 4.16). By the end of the 21*st* century both scenario simulations (A2 and B2) show a substantial weakening of the AMOC cell with respect to the mean preindustrial values (Figure 4.11c). This weakening is more prominent in the deep ocean, with a maximum decrease of ~ 14 Sv around 3000 m depth that leads to a shoaling of the whole AMOC cell that is compatible with results from other climate change simulations (Manabe and Stouffer, 1994; Schaeffer et al., 2004; Bryan et al., 2006; Drijfhout et al., 2008). Also relevant is a slowdown of the GSR overflow.

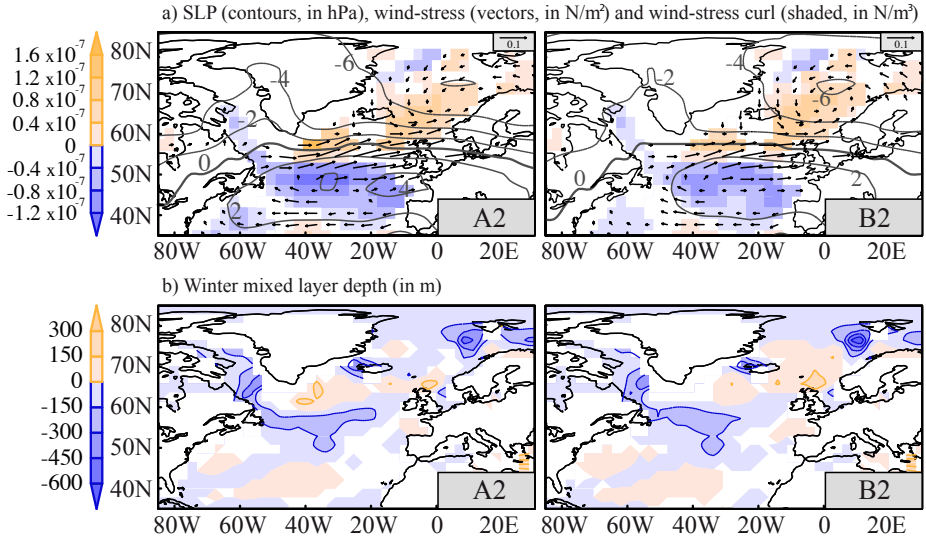

Fig. 4.15: Difference between the climatological mean of different quantities in the period 2070-2100 of the future scenarios A2 (left) and B2 (right) and the preindustrial era (1100-1850) in FOR1. The variables explored are: a) SLP (contours, in hPa), wind-stress (vectors, in N/m^2) and wind-stress curl (shaded, in N/m^3), b) winter mixed layer depth (in m). The zero lines are represented as a thick contours. Significance is assessed like in Fig. 4.11c.

To understand these changes, other quantities are investigated. The main response in SLP is shown in Figure 4.15a, characterised by a dipole-like structure that resembles a positive phase of the NAO. Other global warming runs also predict a positive increase in the NAO with increasing GHG concentrations (Stephenson et al., 2006; Meehl et al., 2007). As already shown in Section 4.2, positive NAO phases go along with increased Ekman pumping and zonal wind stress south of Cape Farewell, both countering the weakening effect of the lighter surface conditions on convection activity. As a result, there is a small increase in the mixed layer depth at the Western Irminger Sea (Figure 4.15b). Other regions, like the Inner Labrador or the Nordic Seas, show a general weakening of convection (Figure 4.15b). However, these changes seem insufficient to explain the major reduction in the AMOC strength.

We turn our attention to the basin-scale changes in density, separating the contributions from temperature and salinity. Under climate change conditions the Atlantic ocean experiences a general warming which translates into negative density anomalies all across the basin, more important in the GIN Seas and at tropical latitudes (Figure 4.16a). However, the main changes in density are largely related to salinity (Figure 4.16b). In the Tropics, surface salinity increases through reduced precipitation and enhanced evaporation (Figure 4.16c), canceling out the effect of the local warming on density. Note that positive freshwater fluxes (from the atmosphere to the ocean) are related to reduced evaporation and increased snow melt and precipitation. In contrast, North Atlantic salinity decreases considerably in response to a general increase in precipitation, a local decrease of evaporation near 50° N, and a lesser contribution from snow melt at higher latitudes. In the GIN seas, the combined effect of both salinity and temperature adds up to produce a local drop in density. The lighter waters north of the sill, plus the small net changes in the Tropics result in a sizable reduction of the meridional density gradient (black contours in Figures 4.16a,b), that favours a weakening of the GSR overflow as well as of the AMOC (Thorpe et al., 2001). Therefore, results highlight the crucial role of salinity and the water cycle to drive the major changes in the Atlantic.

4.5 Conclusions

The present chapter focuses on the analysis of the AMOC variability in an unforced present-day control run, two forced runs for the last millennium, and two IPCC scenarios. The evolution of the MOI throughout the millennial simulations evidences that most of the AMOC variability takes place at multidecadal time scales both in the control and the forced runs. The main mechanisms responsible for the overturning variability in two different time scales have been identified

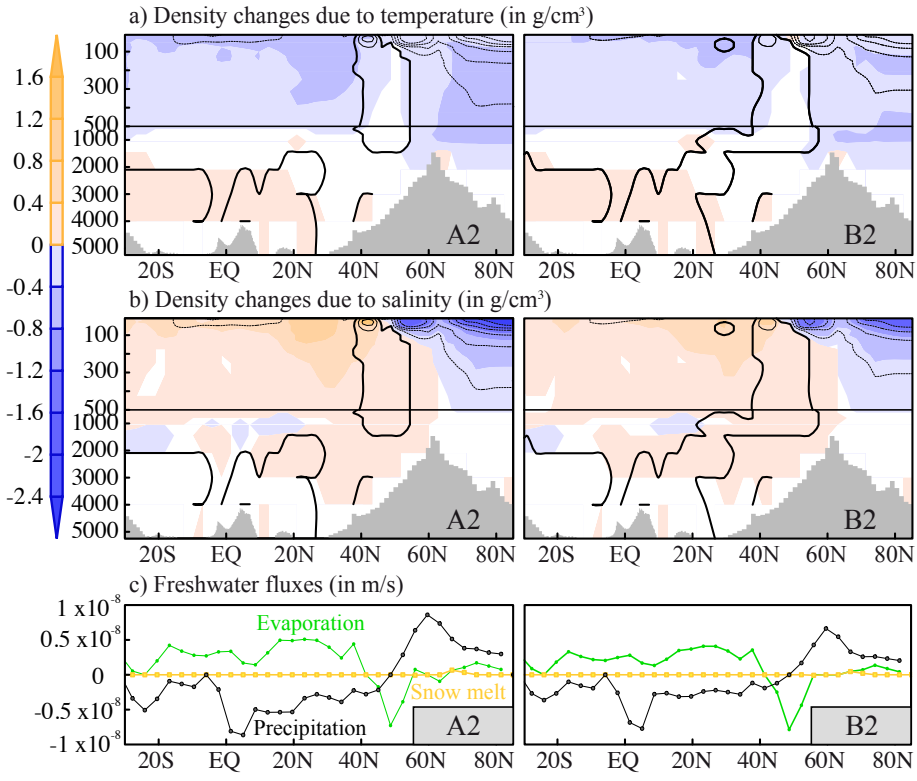

Fig. 4.16: The same as in Fig. 4.16 but for the density changes in depth (in g/cm^2) due to a) temperature and b) salinity. To understand these later changes we show c) freshwater fluxes (in m/s) related to precipitation, evaporation and snow melt. Note that positive precipitation and snow melt relate to freshwater fluxes from the atmosphere to the ocean, while positive evaporation relates to freshwater fluxes from the ocean to the atmosphere. Black contours in panels a,b account for total changes in density (contour interval is 0.4 g/cm^2).

and analysed. In the high-frequency the local overturning variability is found to be forced by different wind regimes at different latitudes, largely driven by three well-known teleconnection patterns: ENSO, NAO, EA. The analysis in the low frequencies underlines the role of Labrador and Irminger convection in the North Atlantic deep water formation, and thereby in the variability of the overturning circulation. The delayed influence of the NAO in the forced runs, leading convec-

tion changes by one year, is in line with other model simulations (Delworth and Greatbatch, 2000; Eden and Willebrand, 2001; Bentsen et al., 2004; Guemas and Salas-Mélia, 2008) and observational analyses (Dickson et al., 1996; Curry et al., 1998). The balance of evidence from available modelling and observational studies suggests that both heat fluxes changes and wind-stress variations are important means of conveying NAO variability to influence AMOC variations in a wide range of frequencies. Although our results emphasise more the role of wind-stress changes, anomalous heat flux forcing can also play an important contribution as suggested in other studies (Delworth and Greatbatch, 2000; Eden and Willebrand, 2001). The importance of persistent anomalous heat fluxes for AMOC variability and predictability in the ECHO-G model was previously analysed in Chapter 3.

The influence of the radiative forcing has been also evaluated. Among the three forcing factors considered, only the GHG concentrations have a strong impact on the AMOC strength. The two forced simulations exhibit a substantial decrease in the overturning strength starting in the Industrial Era and continuing in the future scenario simulations (Figure 4.2), well below the range of natural AMOC variability simulated for the past millennium and the control simulation. This final weakening is associated with a reduced meridional density gradient and with decreased convection in the North Atlantic, both mainly responding to changes in the atmospheric water transport. In contrast, the forcing due to insolation and volcanic aerosols produces minor changes in salinity and moderate shallow changes in temperature. In the case of solar irradiance, these changes occur far from the Labrador and Irminger convection regions, and thereby the impact on the AMOC is negligible. More interestingly, the upper cooling following the main volcanic eruptions is accompanied by a rise in surface salinity, both therefore contributing to a small general increase of convection in the North Atlantic. This produces a minor strengthening of the AMOC cell, in particular if compared to results from other models (Stenchikov et al., 2009; Ottera et al., 2010).

5

World ocean heat content variability in the last millennium and two IPCC scenarios*

Plus tard, c'est un océan, une mer noire sur laquelle tu navigues, comme si ton nez était l'arête, ou plutôt l'étrave d'un gigantesque paquebot...

L'eau t'entoure de toutes parts, mer noire, immobile, extraordinairement plate, même pas phosphorescente, et pourtant, tu as l'impression que tu pourrais découvrir chaque détail, le moindre nuage s'il y avait un ciel, la plus petite terre s'il y avait un horizon. Mais il n'y a que la mer, (et tu es tout entier étrave creusant sans effort, sans bruit, sans vibration, les traces blanches et profondes de ton passage, comme un soc de charrue retournant un champ).

George Perec. Un homme qui dort. 1967

A manifest proof of human-made influence on climate is the recent warming of the world oceans (Levitus et al., 2001), its prominent features being only reproduced by models when anthropogenic GHG forcing is considered (Levitus et al., 2001; Crowley et al., 2003; Gregory et al., 2004; Barnett et al., 2005; Delworth et al., 2005; Palmer et al., 2009). The positive trend in upper ocean heat content is robust to all the observational datasets and processing methods (Lyman et al., 2010; Trenberth, 2010). These same observational estimates report a flattening of the OHC trend since 2003, despite the steady increase in GHG concentrations and net radiation at the top of the atmosphere (Trenberth and Fasullo, 2010). This

* The main contents of this chapter are included in:
Ortega, P., J. F. González-Rouco, M. Montoya and H. Beltrami, 2011: Variability of the ocean heat content during the last millennium. An assessment with the ECHO-g Model. In preparation.

slowdown of the upper ocean warming probably indicates a significant impact of other external and internal sources on the OHC. In the 20th century, two other prominent factors besides the GHG rise are known to have had a noticeable contribution to the global OHC integral. Both anthropogenic, and to a lesser extent, volcanic aerosols have partly offset the ocean warming resulting from increasing GHG concentrations (Delworth et al., 2005). Furthermore, the influence of volcanoes is particularly important to explain the observed decadal OHC changes (Domingues et al., 2008). Besides the changes in radiative forcing, other processes related to internal natural variability can potentially modulate the upper OHC variability in the next decades, through increased heat flux exchange with the atmosphere and also through enhanced heat transfer to deeper ocean levels (Katsman and van Oldenborgh, 2011). A clear example is the AMOC, which is responsible for heat redistribution in the Atlantic Ocean and also has an impact on its decadal upper temperature variability (e.g. Knight et al., 2005). Likewise, other modes of atmospheric and ocean variability can influence OHC. Levitus et al. (2005b), for instance, propose a reversal of polarity in the PDO to explain the observed interdecadal OHC variability from 1956 to 2003. Also in the Pacific ocean, Willis et al. (2004) report a potential influence of strong ENSO-related events on the global OHC budget at interannual timescales. However, these latter analyses are prior to the identification of important instrumentation problems in the OHC estimates resulting, among other features, in an overestimation of its interdecadal variability (Levitus et al., 2009), and should be therefore confirmed in the new corrected climatologies (Domingues et al., 2008; Ishii and Kimoto, 2009; Levitus et al., 2009).

The aim of this study is to improve our understanding on the processes and factors influencing OHC variability, through the analysis and comparison of both simulations and observations. The experiments employed herein are therefore the same already used for the analysis of AMOC in Chapter 4 and described in Chapter 2: two forced simulations of the last millennium (FOR1 and FOR2), two future climate change scenario runs (A2 and B2), and a long control simulation (CTRL2). As for the analysis of the AMOC (see Chapter 4), this approach places the recent ocean warming within the range of past OHC variability. Of particular interest is the comparison with the OHC change during the MCA to the LIA transition. Additionally, an observational dataset of OHC variations for the period 1955-2010 is also considered (updated version of estimates in Levitus et al., 2009). This set of model experiments and observations allows for an evaluation of the prominent features of OHC variability during the instrumental period. Afterwards, the analysis is extended to the last millennium to evaluate the impact

of both the forcing and internal climate variability on the OHC variations from interannual to secular timescales.

The chapter is structured as follows: in Section 5.1 simulations are compared to OHC observations and other proxy reconstructions in the last millennium. The impact of the external forcing on OHC variability is addressed in Section 5.2. Likewise, Section 5.3 deals with the contribution of different modes of climate variability to global and local OHC. To conclude, Section 5.4 summarises the major findings of this study.

5.1 Temporal evolution of ocean heat content and thermal expansion

This sections describes the major aspects of OHC temporal variability, as represented by the ECHO-G simulations during both the observational period and the last thousand years. In each case, simulated variability is compared with the available observational (instrumental or proxy) evidence.

5.1.1 OHC variability in the observational period

Estimates of ocean heat content are calculated from global records of upper ocean temperature. This computation requires reliable and globally distributed subsurface instrumental data, as well as the use of different interpolation and regridding techniques. Since 1950, the spatial coverage of temperature measurements has steadily improved, and new data sources have become available (e.g. moored buoys, ARGO floats, bathythermograph measurements). The integration of these data is open to important uncertainties, since it is sensitive to the records considered and the different methodologies applied, such as the mapping and bias correction techniques (Gregory et al., 2004; Lyman et al., 2010). This has lead to the publication of somewhat different OHC estimations by different groups and institutions (Domingues et al., 2008; Ishii and Kimoto, 2009; Levitus et al., 2009), the major discrepancies concerning the representation of interannual OHC variability (Lyman et al., 2010).

Our analysis will be therefore focused on the long-term trends, and the representation of decadal OHC variability. For this study, observational estimates (OBS) are computed through gridded NODC-OCL temperature fields from the surface to 700 m depth[†]. An earlier estimate of these OHC anomalies is presented in Levitus et al. (2009). In the ECHO-G simulations, OHC anomalies are computed in the upper 700 m of the ocean, for direct comparison with observations.

[†] http://www.nodc.noaa.gov/OC5/indprod.html

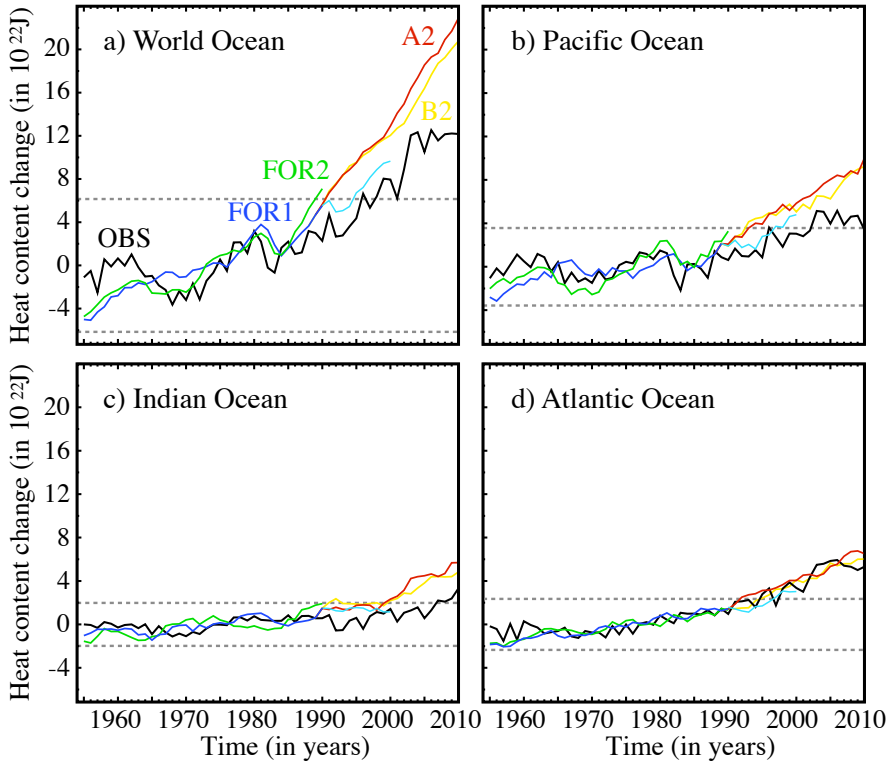

Fig. 5.1: Evolution of heat content anomalies (in 10^{22}J) in the upper 700 m of the: a) World ocean; b-d) Pacific, Indian and Atlantic oceans, respectively. Observed OHC is computed from temperature profiles of the Ocean Climate Laboratory at NODC in the period 1955-2010 (OBS). Simulated OHC anomalies are shown for the forced simulations FOR1 and FOR2 from 1955 to 1990, and for the scenario runs A2 and B2 from 1991 to 2010. Besides, FOR1 has been extended to year 2000 (light blue line), thus also incorporating Pinatubo's eruption. Horizontal dashed lines represent a threshold of ± 2 standard deviations from the long-term variability in CTRL2. The reference period for the anomalies is 1960-1990.

The global integral of these anomalies is shown in Figure 5.1a. To cover the whole observational period (1955-2010) with the forced simulations, the first 20 years of the future scenario runs are shown after 1990. Since A2 and B2 assume zero volcanic activity and keep solar irradiance constant from year 1990 AD, they both miss the natural external influences. In order to take into account a more

recent history of these forcings, FOR1 has been extended to year 2000, now also including the influence of Pinatubo's eruption (in 1991 AD). Note that OHC oscillates within the range of CTRL2 variability (dashed horizontal lines in Figure 5.1) from 1955 to 1990, and goes beyond these values afterwards.

Observed and simulated trends are now compared separately before and after 1990 (Table 5.1). All forced simulations overestimate the global OHC trends, especially from 1955 to 1990, the period with largest observed decadal OHC variability. This overestimation can be arguably attributed to the lack of sulphate aerosols in the forced simulations, that can offset the GHG warming up to a 50% (Delworth et al., 2005). By basins, trends are mostly overestimated in the Pacific (that dominates the warming due to its larger extension) and Indian oceans, and show a good agreement in the Atlantic (Figure 5.1b-d and Table 5.1), probably indicating that some internal variability process is compensating the offset in the Atlantic warming trend.

Table 5.1: Linear trends of the ocean heat content (in 10^{22}J/yr) during the periods 1955-1990 and 1991-2010 in the World ocean, and the three main basins.

		World Ocean	Pacific Ocean	Indian Ocean	Atlantic Ocean
1955-1990	OBS	**0.11**	0.03	0.02	0.06
	FOR1	**0.24**	0.09	0.05	0.10
	FOR2	**0.26**	0.11	0.07	0.08
1991-2010	OBS	**0.57**	0.20	0.14	0.23
	A2	**0.86**	0.36	0.25	0.25
	B2	**0.72**	0.30	0.17	0.26

To better illustrate interdecadal variability, OHC curves are replotted in terms of heat content by unit area (Figure 5.2). The corresponding changes in the total radiative forcing (RF), and the equivalent radiative forcing of each factor are also shown to shed light on their individual role (lower panels in Figure 5.2). Globally, forced simulations are able to partly reproduce the low-frequency OHC modulation in observations, associated to the cooling effect of volcanoes. Both simulations and observations evidence that most decadal variability occurs in the Pacific and Indian oceans, while the Atlantic ocean warms almost linearly. Discrepancies in the low-frequency among FOR1, FOR2 and OBS (blue, green and black curves in Figure 5.2) point to potential influences of natural climate variability in the Pacific and Indian basins, superimposed to the GHG-driven trend and the volcanic modulation. The global integral shows better agreement

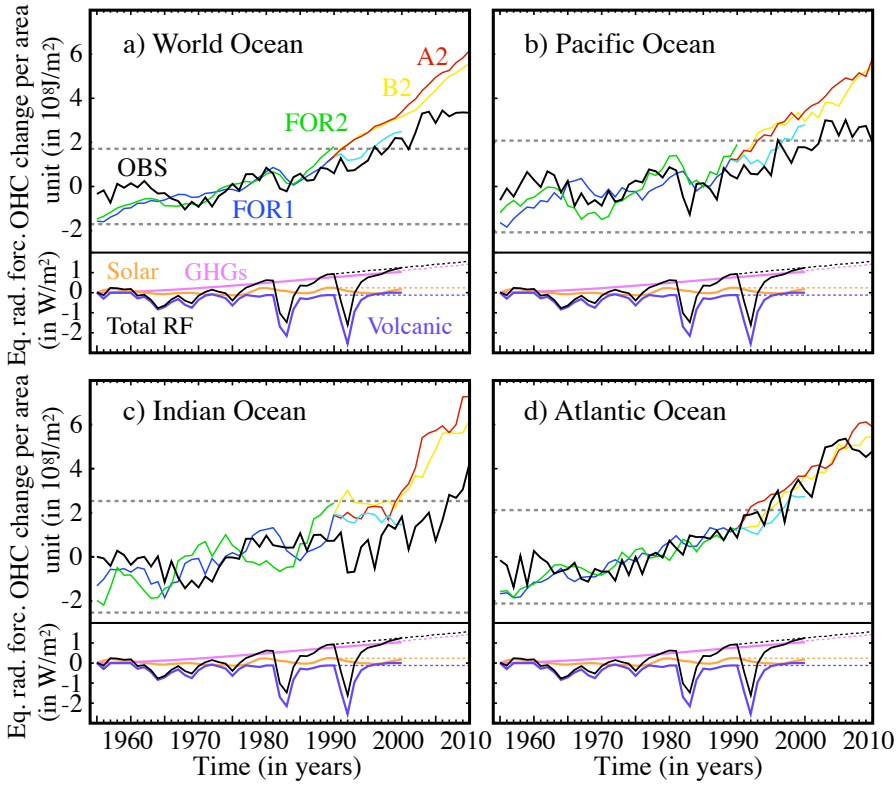

Fig. 5.2: The same as in Fig. 5.1 but the heat content changes are normalised per unit area (in $10^8 J/m^2$). Below each panel, estimates of the different radiative forcings are shown, expressed as changes with respect to year 1955. Dotted lines correspond to projections of the radiative forcing in the scenario simulation A2.

since local effects are partly canceled out. Overall, the forcing explains about 70% of the simulated and observed OHC variance, either globally or by basins (Table 5.2). However, the large variance explained is mainly related to the steep warming trend after year 1990 (Table 5.3).

To assess the reasons for the different degree of agreement between observational and simulated trends before and after 1990, the spatial distribution of recent trends is now explored in Figure 5.3. From 1955-1990 (Figure 5.3, left column), a weak general warming is observed in the three datasets, subject to different local influences in the Atlantic and Pacific oceans, with simulations only showing marginal agreement with observations. From 1991 onwards (Figure 5.3,

Table 5.2: OHC variance explained by the total equivalent radiative forcing in whole ocean and the three major basins during the period 1955-2010.

	World Ocean	Pacific Ocean	Indian Ocean	Atlantic Ocean
OBS	**68%**	67%	42%	63%
FOR1+A2	**69%**	66%	66%	70%
FOR1+B2	**67%**	63%	68%	64%

Table 5.3: The same as in Table 5.2 but for the periods 1955-1990 and 1991-2010.

		World Ocean	Pacific Ocean	Indian Ocean	Atlantic Ocean
1955-1990	OBS	**33%**	32%	20%	11%
	FOR1	**12%**	4%	22%	14%
	FOR2	**23%**	23%	27%	4%
1991-2010	OBS	**84%**	61%	69%	76%
	A2	**99%**	98%	90%	97%
	B2	**99%**	95%	86%	95%

right column), the location of observed and simulated trends is in better accordance, with larger tendencies in the North Atlantic and western Pacific, and a rather uniform warming in the Indian basin. Note that observations show opposite trends in both the Atlantic and Pacific oceans with respect to the first period, that could be compatible with shifts in the tendencies of the PDO and the AMO indices among both periods. These contributions of natural variability will be further analysed in Section 5.3. Finally, during the last 90 years of the scenario simulations (Figure 5.4) a worldwide warming pattern emerges, with larger trends at high latitudes of the Northern Hemisphere. Yet, the local cooling south of Greenland persists, in line with the reported weakening of the AMOC cell, resulting in lesser downward heat transport (see Chapter 4).

The results suggest both a predominant influence of the forcing, most important from 1990, along with some impact of internal climate variability, able to produce important OHC changes at least at local scales. For that reason, a separate analysis follows, first focused on the fingerprints of the external forcing (Section 5.2), and later investigating the influence of other processes of natural variability (Section 5.3). Due to the limited time span of the observational period, the use of the millennial simulations allows for a better understanding and

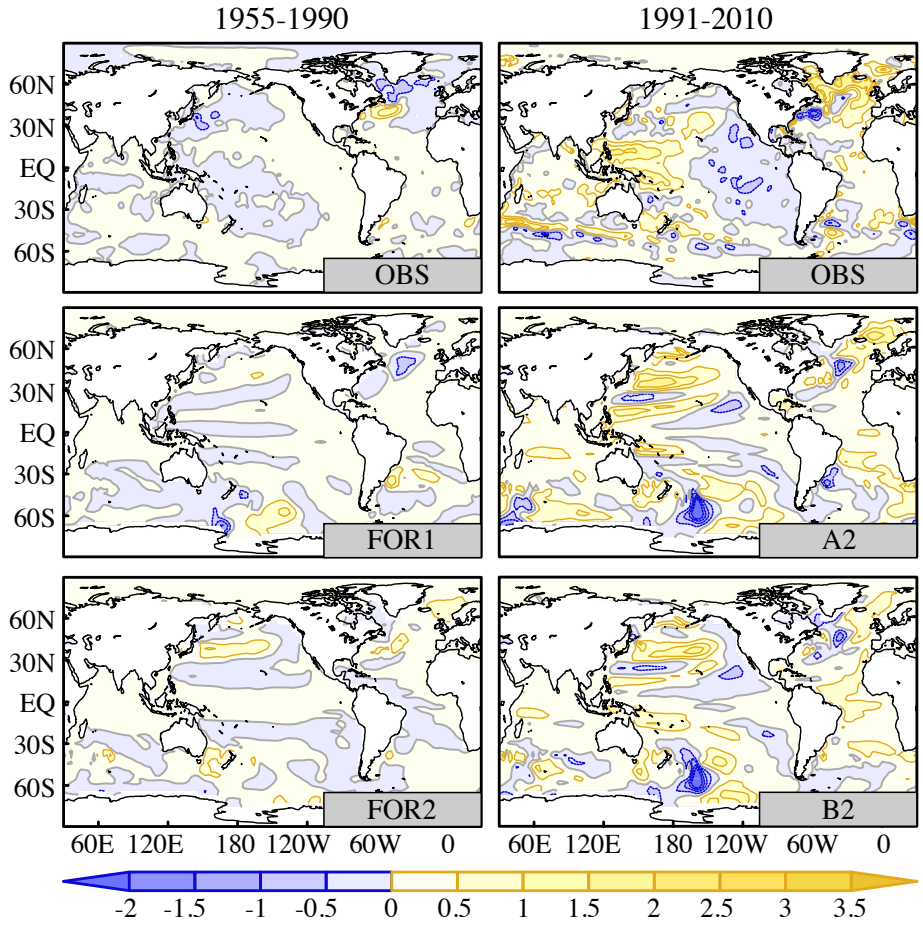

Fig. 5.3: Linear trends of the observed (top panel) and simulated (lower panels) OHC (in $10^8 J/m^2 yr$) in the upper 700 of the ocean for the periods 1955-1990 (left) and 1991-2010 (right).

quantification of their respective roles. The simulated OHC variability is next assessed for the last millennium.

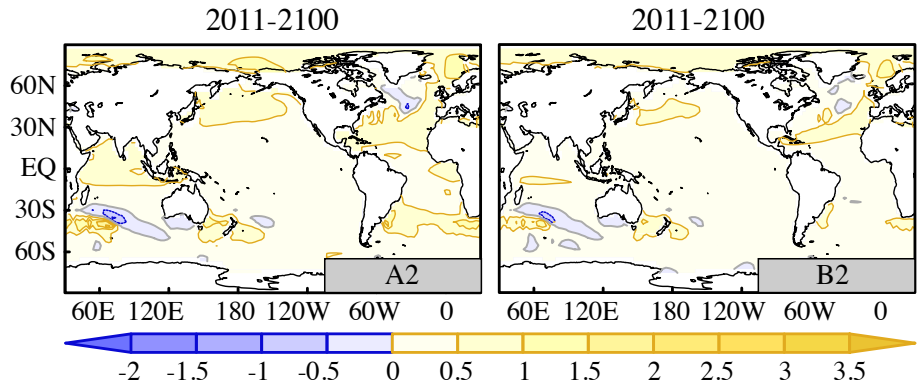

Fig. 5.4: The same as in Fig. 5.3 but for A2 (left) and B2 (right) in the period 2011-2100.

5.1.2 Thermosteric sea level and ocean heat content throughout the last millennium

Ocean heat content, when integrated over deep ocean levels, is a good indicator of decadal changes in the radiation balance at the top of the atmosphere (Palmer et al., 2011). Model simulations, however, can be subject to initial instabilities in the deep ocean, that would artificially mask the oceanic response to the radiative forcing. In fact, the ECHO-G simulations show important temperature trends at intermediate and bottom waters (Figure 5.5). In FOR1, due to its initial conditions (see Chapter 2), the ocean starts anomalously warm at 1000 m depth, and only the shallowest layers exhibit certain modulation by the external forcing. Likewise, CTRL2 shows opposite and long-lasting trends above and below 2000 m, probably indicating a permanent drift in the ocean. For the rest of the analysis, this model-dependent drift in ocean temperature is removed from the forced runs.

OHC in the upper 700 m shows a comparable evolution in FOR1 and FOR2 since 1700AD (Figure 5.6a), while substantially smaller variability occurs in CTRL2 (dotted black line). Prior to this year, FOR1 is clearly influenced by its warm starting conditions. For this reason, analyses covering the last millennium will be only addressed with FOR2. It cannot be established whether some residual artificial trends are still present in FOR2. Since the influence of the initial trends is negligible during the last three centuries, FOR1 will be used together with the A2 and B2 scenario runs for studies in the observational period.

To our knowledge, there are no direct proxies for the OHC variability in the last millennium. There are, instead, long-term observations (Jevrejeva et al.,

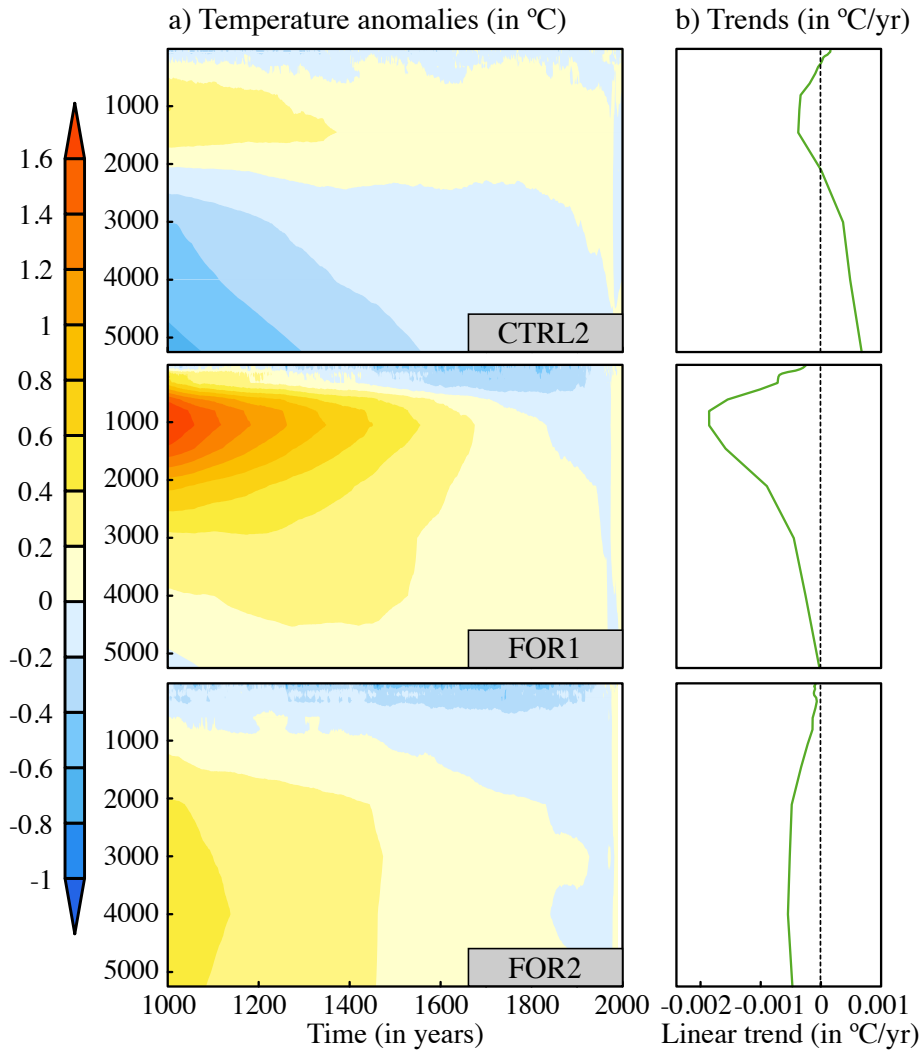

Fig. 5.5: a) Hovmoller plot (depth vs time) of the anomalous global temperature (in °C) for CTRL2, FOR1 and FOR2. The reference period is 1960-1990. b) Long-term trends of the ocean temperature means at different depths.

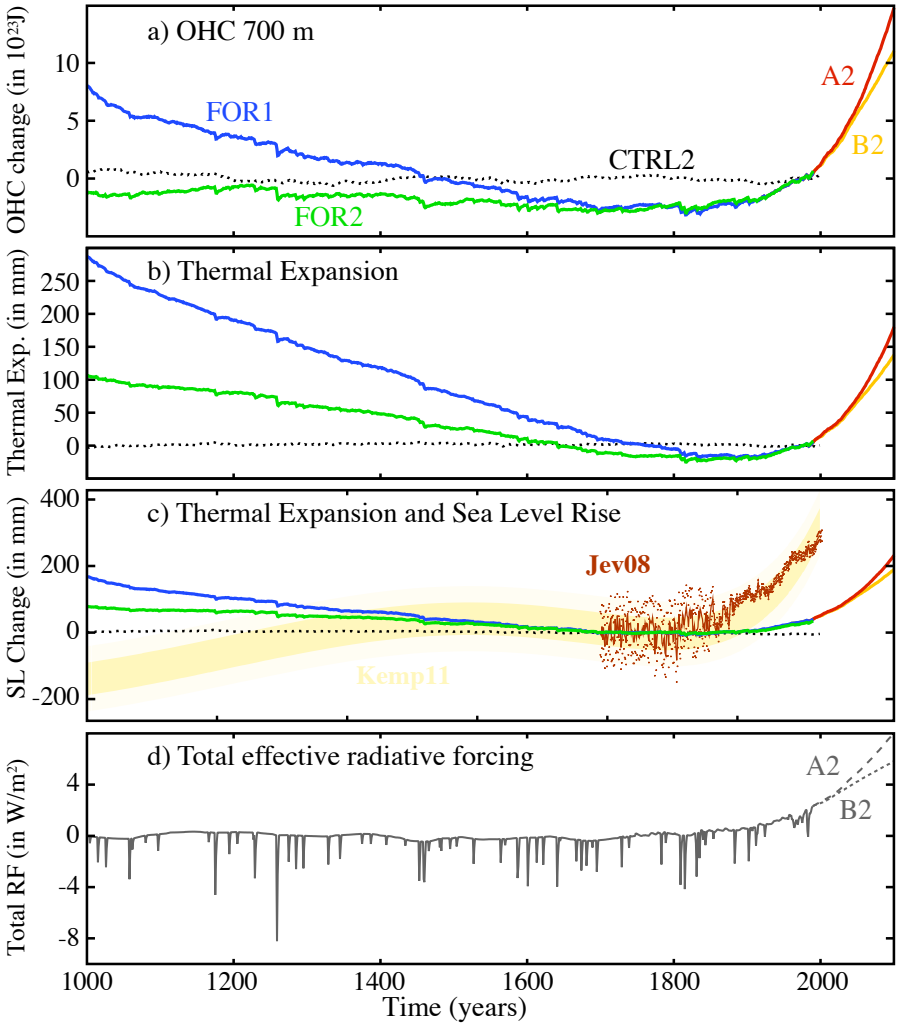

Fig. 5.6: a) Anomalies of global ocean heat content in the upper 700 m (in 10^{23}J) wrt the period 1960-1990; b) Anomalies of the thermal expansion in the whole depth of the ocean (in mm) for the same period; c) Detrended thermal expansion anomalies wrt the period 1700-1800 (see text for details); d) Effective radiative forcing applied to the forced simulations (in W/m^2). For comparison, sea level rise changes estimated from tide gauges (brown line; Jevrejeva et al., 2008a) and an idealized summary curve from proxy reconstructions with salt-marsh sediments in North Carolina (yellow filled curve; Kemp et al., 2011).

2008a) and paleoclimate reconstructions (Kemp et al., 2011) of past sea level (SL) changes in the last two thousand years. These records can provide a good benchmark to evaluate the realism of the initial trends in the simulations, since the thermosteric contribution to SL variability responds directly to changes in the OHC. Given that estimates of SL change represent the global ocean, thermal expansion is computed for the whole ocean depth in the simulations. However, it should be noted that other contributions to SL variability, like the melting of land glaciers and polar ice caps, are not represented in the ECHO-G model and cannot be included.

Thermal expansion in both forced simulations shows a strong drift from initial conditions (Figure 5.6b), fueled by the trends in the deeper ocean. The effect of this drift can be partly corrected by comparing with the SL data. The longest instrumental SL record is computed from tide gauge observations since 1700 AD (Jevrejeva et al., 2008a, hereafter Jev08). These estimates show evidence that acceleration of sea level rise began about 200 years ago, and was preceded by a century of comparatively flattened SL variations (brown line in Figure 5.6c). A local reconstruction from salt-marsh sediments in North Carolina (Kemp et al., 2011, hereafter Kemp11) is in reasonable agreement with estimates in Jev08, and shows stable SL variability in the same period. This record is summarised in an idealised manner by the yellow filled curve in Figure 5.6c. It is therefore plausible that all components of sea level rise (SLR), and in particular the thermal expansion, leveled off during the 18th century. Hence, under this assumption, to correct the effect of initial trends in the later centuries of the forced runs, thermal expansion is flattened in the period 1700-1800 by removing the corresponding simulated trends. In this way, the rate of observed SLR and simulated thermal expansion can be compared in the last two centuries.

Before the 17^{th} century, both the simulated thermal expansion and the SL proxies of Kemp11 show comparable downward trends from 1500 onwards, but exhibit a clear mismatch in the earlier centuries. Indeed, proxies give evidence of a steady SLR since 1000 AD while the forced simulations show a sustained decrease in thermal expansion. None of these trends is observed in our estimates of the total radiative forcing (Figure 5.6d). It should be kept in mind that the SL curve shown for Kemp11 is idealised, and represents local changes in North Carolina. It is not clear to what extent this proxy represents the global SL changes. Likewise, the analysis suggest that in the simulations the effect of the initial trends is still noticeable before 1700 AD.

In the last two centuries the drift has been corrected, and thermal expansion only accounts for about a sixth of the total sea level rise in the last two centuries (Table 5.4). It is not clear, however, if this contribution is underestimated by the model. While some observational studies suggest a leading contribution from

thermal expansion on sea level (Bindoff et al., 2007; Domingues et al., 2008), others point to a dominant role of melting processes (Miller and Douglas, 2004; Jevrejeva et al., 2008b). In the period 1955-2000 of the ECHO-G simulations, thermal expansion would account for a third of the recent observed sea level rise (Figure 5.7 and Table 5.4). This trend is notably overestimated by the model since it is almost twice as large as the trend for the observed thermal expansion (computed from temperatures in OBS), probably due to the missing contribution of anthropogenic aerosols. During the scenario simulations, the rate of thermal expansion is accelerated by about a factor of three with respect to the period 1955-2000 (Table 5.4). Although the corresponding trend for the SLR cannot be estimated by the model, the evaluation for the 19^{th} and 20^{th} centuries suggested a thermosteric contribution of about one sixth. This result, however, is difficult to reconcile with future projections in the fourth IPCC assessment report (Meehl et al., 2007), in which thermal expansion is expected to explain 70 to 75% of the total sea level rise by the end of the 21^{st} century. In order to improve our understanding on the direct role of ocean warming to SLR, the mass increase due to land ice melting needs to be better constrained.

Table 5.4: Linear trends in sea level (in mm/yr) and thermal expansion (in mm/yr) for the whole ocean in the periods 1955-2000, 1800-2000 and 2000-2100.

	Thermal expansion				Sea Level Rise
	OBS	FOR1	FOR1+A2	FOR1+B2	Jev08
1800-2000		0.24	0.24	0.24	1.38
1955-2000	0.26	0.46	0.53	0.52	1.55
2000-2100			1.78	1.41	

On the following, the focus is placed on the OHC in the upper 700 m, to minimise the effect of the model drift. At this depth, the OHC (Figure 5.6a) clearly responds to variations in the net radiative forcing (Figure 5.6d). The main aspects of this influence are discussed in the next section.

5.2 Fingerprint of external forcing on ocean heat content

This section analyses the main temporal and spatial features of the upper OHC response to the external forcing. A first assessment is performed in the instrumental period.

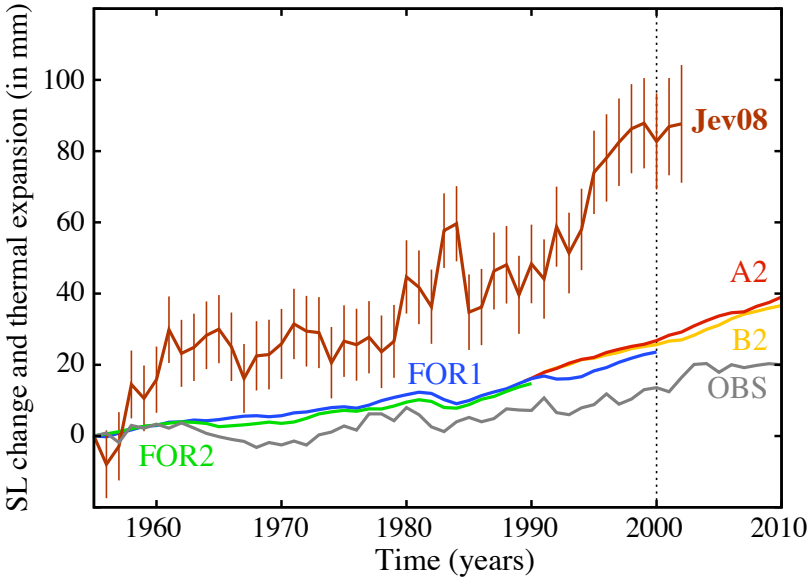

Fig. 5.7: Sea level rise from year 1955 in tide gauge observations (brown lines; Jevrejeva et al., 2008a), and thermosteric changes in FOR1 and FOR2 (blue and green lines, respectively), the scenario simulations A2 and B2 (red and orange lines, respectively) and observations (grey line; computed with temperature fields from NODC-OCL). The vertical dotted line sets the period where linear trends in Table 5.4 are calculated.

5.2.1 Quantifying recent forcing impacts

The last 55 years have witnessed relevant changes in the radiative forcing, mainly associated to an acceleration of both GHG and sulphate aerosols emission rates and the occurrence of three major volcanic eruptions (Mt. Agung in 1963; El Chichón in 1983 and Pinatubo in 1991) and five complete solar cycles. In response to these changes, the world ocean has experienced a remarkable warming trend, modulated to some extent at decadal timescales (see Section 5.1 and Figure 5.2). In this context, however, impact and attribution studies are constrained by the short time span of the observational records. Particular caution should be taken since physically unrelated quantities can coincidentally vary at comparable timescales. To ensure that no artificial relationship emerges in our analysis, a statistical significance test is employed that takes into account the serial au-

tocorrelation to correct for the effective sample size (same approach followed in Chapter 4).

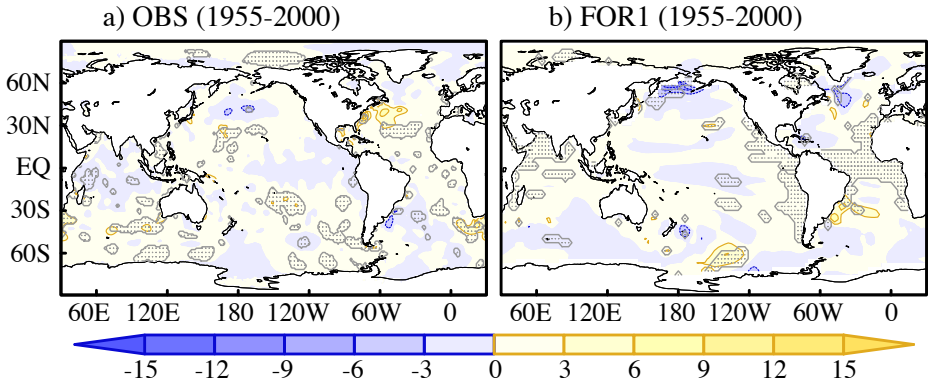

Fig. 5.8: Regression patterns between the anomalies of OHC in the upper 700 m (in $10^8 J/m^2$) and the standardised total radiative forcing in Fig. 5.2 during the period 1955-2000 of: a) the observations, b) the extended FOR1 run. Dotted areas enclose values significant at a 0.05% level according to a Student's t test that takes into account the series autocorrelation to correct the sample size.

Also, in order to maximise the signal of the oceanic response, the analysis in the observational period is exclusively focused on the effect of the total radiative forcing. The period considered for the analysis is 1955-2000, to include the latest changes in solar and volcanic forcing used for the extended FOR1 run. Figure 5.8 shows the regression patterns between the total radiative forcing in this experiment (see Figure 5.2) and the observed and simulated OHC changes in the upper 700 m. Both plots exhibit an overall warming pattern and some noticeable local coolings. Yet, there is a general disagreement in the regions where these changes are significant. The validity of these results will be assessed by extending the analysis to the whole FOR2 run, the millennial simulation with steadier initial conditions. This will allow to provide further insight on the particular role of each forcing factor.

5.2.2 Influence of the forcing in the last thousand years.

Within the last millennium, the pattern of response to an increase in the total radiative forcing (Figure 5.9a) corresponds to a generalised warming of the upper ocean, with larger values in the extratropics, and some local coolings in regions

of deep water formation, like the Labrador and Weddell Seas. Unlike in the observational period, most of these changes are significant, especially northward of 40°S.

Considering the individual effect of different factors, only the GHGs have a widespread impact. In particular, they have a significant effect in the Tropics (Figure 5.9b) and the convection regions, being also associated to the largest regression coefficients. In contrast, the fingerprint of solar variability (5.9c) is a mild response mainly localised at midlatitudes in the three major basins. Regression values with the effective solar constant (Figure 5.9d) are considerably lower, as it also includes the non-linear episodic influence of volcanic eruptions. The impact of volcanoes is evaluated instead through a composite analysis focused on the top 25 and 10 preindustrial eruptions, to distinguish a moderate and a strong impact. The composite averages the differences in OHC occurring between the 5 years following and the 5 years preceding the corresponding volcanic eruptions, and assesses their significance by comparing with the 2.5 and 97.5 percentiles of a Monte Carlo ensemble, consisting of 1000 analogous differences in CTRL2. As for the solar irradiance, the largest OHC changes take place in the extratropics (Figure 5.9e-f). The pattern of cooling is similar in both composite analyses, with no remarkable spatial differences. As expected, larger negative anomalies are observed for the strongest eruptions (Figure 5.9f).

To understand the reasons for the different latitudinal OHC response to the forcing and the larger sensitivity in the extratropics, the contribution of heat fluxes at the surface is now explored. First, the long-term mean and standard deviation of these fluxes are characterised (Figure 5.10). In climatological terms (Figure 5.10, left), the net surface heat flux is positive (i.e. into the ocean) near the Equator, the region receiving more solar (shortwave) radiation, and negative (i.e. to the atmosphere) along the warm waters of the western boundary currents and in the deep convection regions, due to increased latent and sensible heat flux. The same regions are associated to the most important heat flux variations (Figure 5.10, right). In particular, the largest changes are found for the shortwave radiative forcing in the Equatorial Pacific, and for the latent and sensible heat fluxes in the convection sites of Labrador and the Southern Ocean. The variability of the incoming shortwave radiation is linked to changes in the total cloud cover, that is characterised by comparatively small climatological values near the Tropics (Figure 5.11, left), but attains large standard deviation values over the tropical Pacific (Figure 5.11, right). It cannot be established, however, if these variations respond to internal climate processes or are directly driven by radiative changes. A regression analysis is thereby considered to isolate the actual influence of the total radiative forcing (Figure 5.12). Regarding the cloud coverage, the main changes associated to a RF increase consist of a general cloud

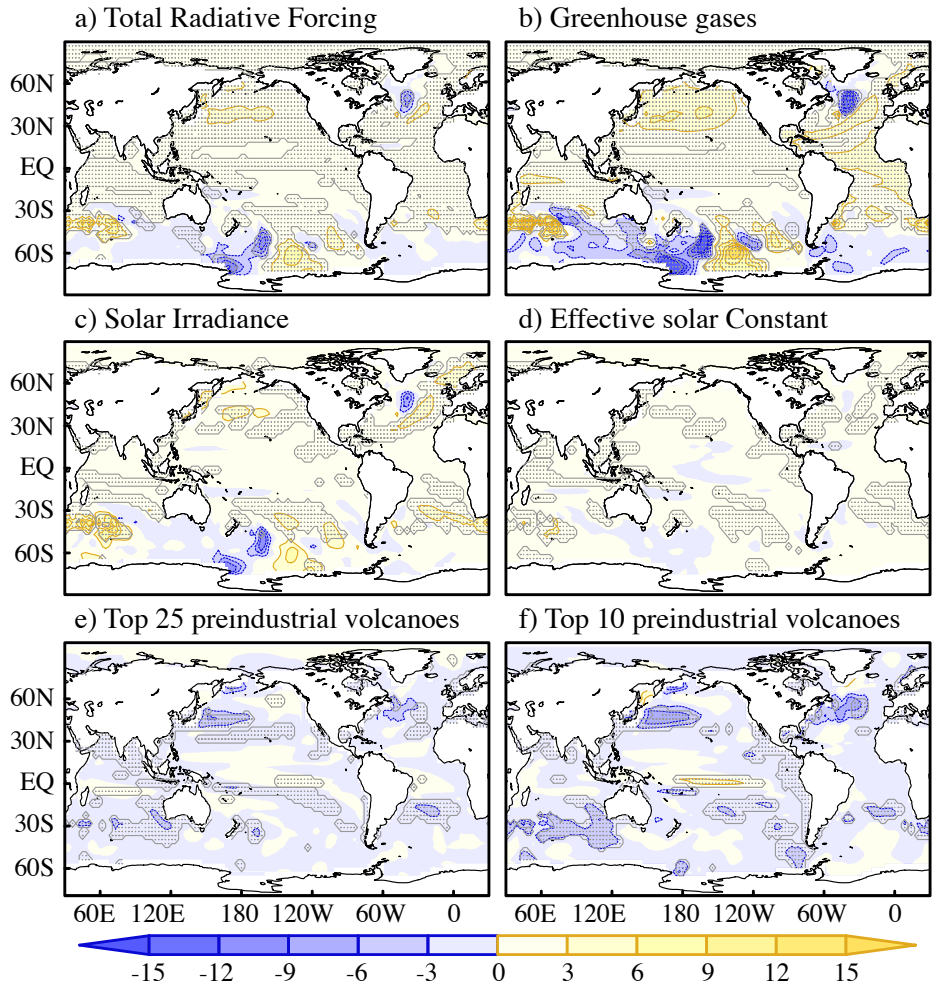

Fig. 5.9: a-d) Regression patterns in FOR2 between the anomalies of OHC in the upper 700 m (in $10^8 J/m^2$) and the standardised series of the total radiative forcing, the equivalent forcing of GHGs, the solar irradiance and the effective solar constant, respectively. Significance is addressed as in Fig. 5.8. e-f) Composite of the OHC differences between the 5 years following and 5 years preceding the top 10 and 25 largest preindustrial eruptions. Significance is established at the 0.05 level through a Monte Carlo test based on 1000 random selections in CTRL2.

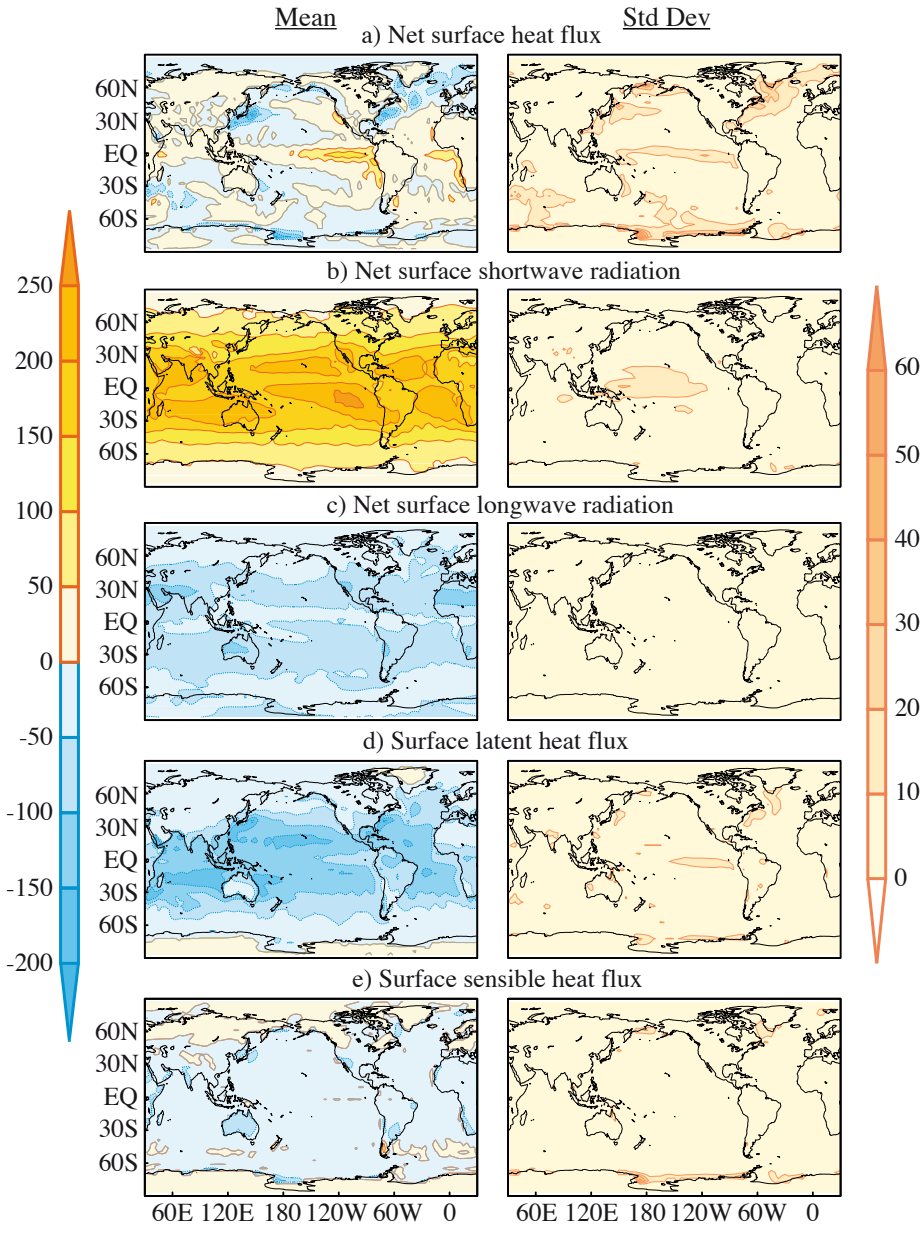

Fig. 5.10: Climatological mean (left) and standard deviation (right) of the different contributions to the net surface heat flux (in W/m^2) in FOR2.

reduction at extratropical latitudes and a remarkable increase over the Ross Sea. These changes clearly correlate with variations in shortwave radiation. At midlatitudes cloud cover decreases leading to increased solar radiation at the surface, while at high latitudes the incoming radiation is reduced in response to the larger cloud fraction (Figure 5.12c). However, the effect of the latter negative shortwave anomalies is offset by the opposite contribution of outgoing longwave radiation, and both latent and sensible heat fluxes (Figure 5.12c-e).

Adding up all the different influences, there is a worldwide net surface warming following the increases of the RF (Figure 5.12b), with larger values in the regions of deep convection and also in the extratropics. In the convection regions the surface warming is not directly attributable to a thermal response to the radiative forcing but it is rather a result of the vertical mixing, since the water column experiences a net cooling (Figure 5.9a). In the rest of the ocean the warming is observed both at the surface and integrated in depth, the OHC increase being therefore related to the downward penetration of the net positive heat flux into the ocean. Besides, the larger response at midlatitudes is likely linked to a local increase of solar radiation at the surface that responds to a significant reduction of cloud coverage. Indeed, the rest of contributions to the net surface heat flux do not reproduce this different latitudinal response.

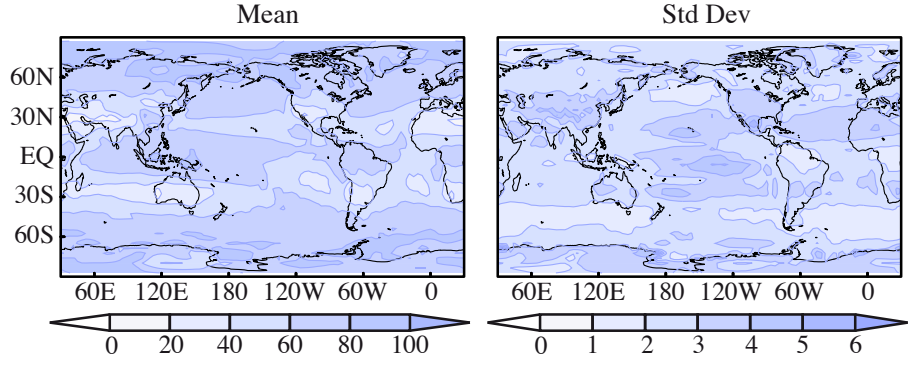

Fig. 5.11: Climatological mean (left) and standard deviation (right) of the total cloud cover (in %) in FOR2.

We turn now our attention to the temporal features associated to the influence of the different radiative forcings. A cross-wavelet analysis (Grinsted et al., 2004) is used to investigate the spectral coherence between the OHC and the different forcings throughout the last millennium. The total equivalent radiative forcing is

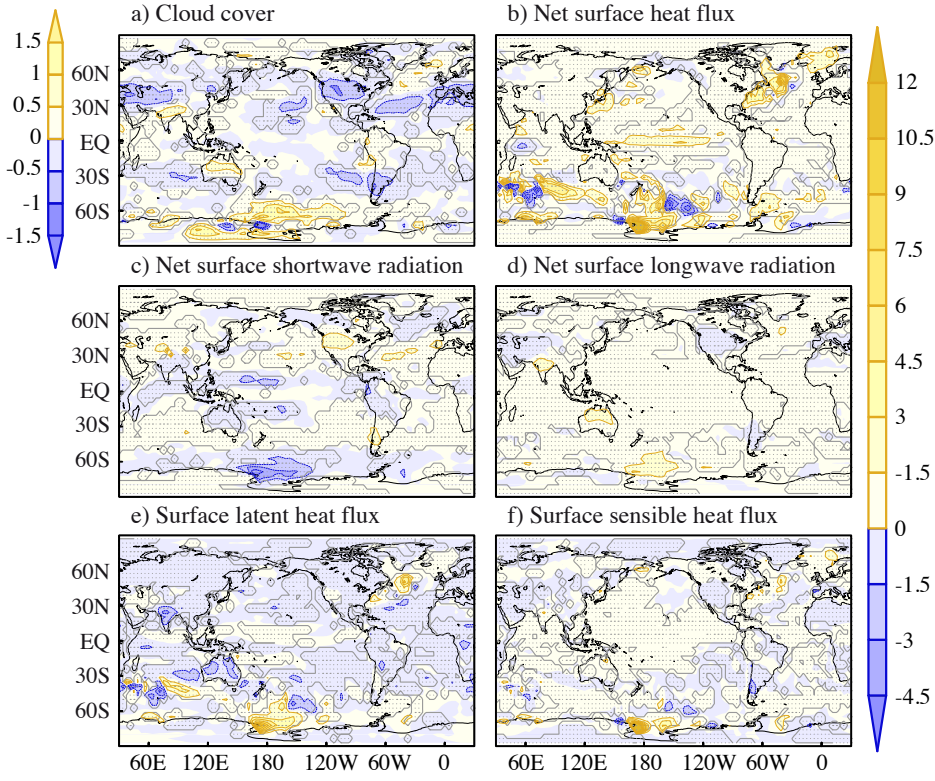

Fig. 5.12: In-phase regression patterns in FOR2 between the standardised total radiative forcing and a) the total cloud cover (in %), b-f) the different components of the net surface heat flux (in W/m^2).

found to lead (since arrows have a small northward component) OHC variability at multiple timescales, mostly from decadal to secular (Figure 5.13). In the preindustrial period, most of this influence comes from volcanoes, as highlighted by the good agreement between the cross-wavelet spectra in Figures 5.13 and 5.14a. Indeed, coherence at interannual timescales is only present when radiative forcing is punctuated by the effect of volcanism. Besides, the influence of volcanic aerosols is also relevant at lower-frequencies. Strong volcanoes impact as a step down signal on the OHC curve (Figure 5.14a, upper panel), as it has been already described in other forced simulations (Gleckler et al., 2006a; Gregory et al., 2006; Gregory, 2010). This influence, in periods of intense volcanism (e.g. 1150 to 1300 AD or 1550 to 1700AD), can dominate the OHC variability at multidecadal and

even secular timescales. Solar variability (Figure 5.14b), in contrast, shows some short intervals of coherence with the OHC at interdecadal timescales (periods of 10 to 32 years). In the last few centuries of the millennium, the slowly-varying GHGs share part of the OHC secular variability, and also some multidecadal variability after the beginning of the industrial era (Figure 5.14c).

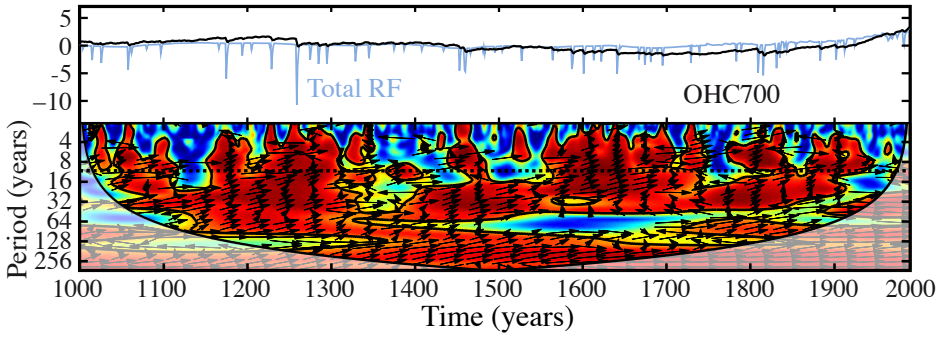

Fig. 5.13: *Top:* Standardised time series of the total radiative forcing and the OHC in the upper 700 m in the FOR2 simulation. *Bottom:* Cross-wavelet spectrum between both time series. The black contours enclose areas where the coherence is significant at a 5% level according to a Monte Carlo test. The arrows indicate the phase of their interrelationship ('westerlies' account for phase zero). Note that positive phases (represented by northward arrows) correspond to the forcing leading the OHC changes. The cone of influence (thick black curve) accounts for the region the edge effects become important. The horizontal dotted line highlights the frequency corresponding to a 10 yr timescale.

So far, the analysis has been centred on the instantaneous OHC response to the external forcing factors. Correlations in Figure 5.15 illustrate their influence at other lags. For the total radiative forcing, significant correlations are found for lead times from 50 to 0 years, and maximum values when it leads the OHC changes by 1-2 years. This maximum impact is associated to the short-lived influence of volcanoes (blue line). In contrast, the slowly varying solar and GHG forcings show maximum correlations for lead times of 20 and 70 years, respectively. This delayed response points to a gradual accumulation of the energy going into the ocean, whose timescale is set by slow vertical diffusion processes.

At higher-frequencies, and in particular at interannual timescales, coherence with the radiative forcing is limited (Fig 5.13) and only the volcanic forcing can explain some OHC variability. Hence, this is the range of frequencies at which

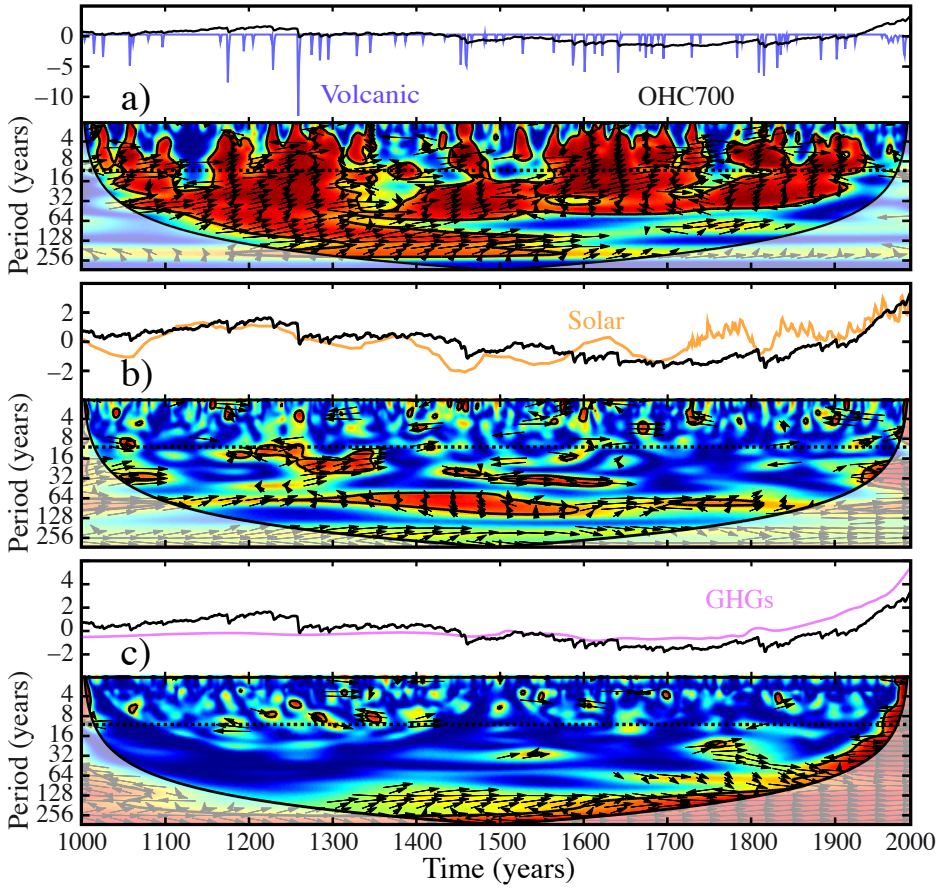

Fig. 5.14: The same as in Fig. 5.13 but for OHC700 and: a) The standardised volcanic forcing; b) The standardised solar irradiance; c) the standardised effective GHG forcing.

internal variability is bound to account for a larger fraction of OHC variability, especially during periods of low volcanic activity (e.g. 1300-1450 AD). The next section develops a comprehensive analysis of its potential impacts.

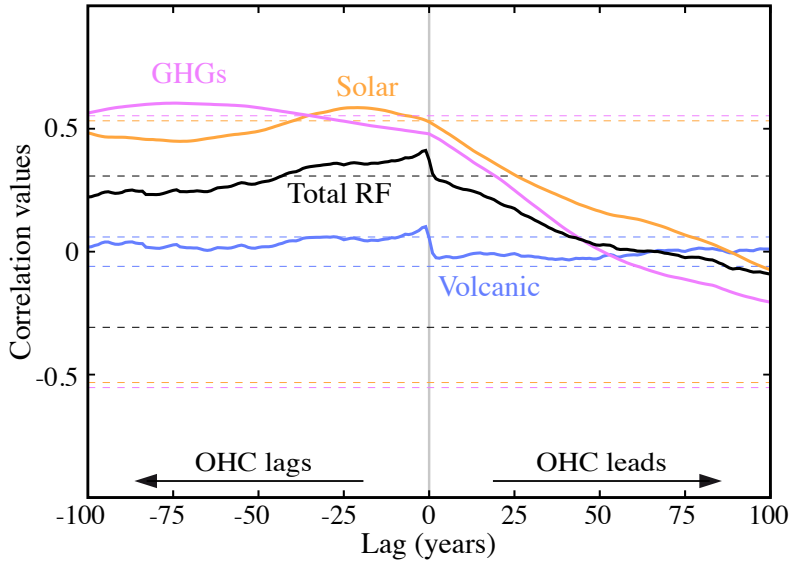

Fig. 5.15: Time-lag correlations in FOR2 between the OHC in the upper 700 m and the different radiative forcings. The thin colored horizontal lines represent the threshold value for significance associated to each forcing. Significance is assessed as in Fig. 5.8.

5.3 Contributions to OHC change from internal climate variability

5.3.1 Influence of internal variability over the last 55 years

Previous sections suggest a potential role of internal modes of variability to locally modulate the upper ocean warming trends in the observational period. Globally, internal climate variability has been proposed to explain part of the interannual OHC changes during the last millennium, especially during periods of low volcanic activity. Other works also support the influence of different modes of climate variability on the OHC. For example, there is particular evidence that ENSO-related variability has produced noticeable interannual OHC changes during the observational period (Willis et al., 2004). Thereby, other climate modes involving large-scale SST changes, such as the AMO or the PDO, can also potentially affect, locally or globally, the OHC budget. Besides, it is also known that predominant atmospheric patterns, such as the NAO, can locally alter the air-sea heat fluxes

at the ocean surface and trigger deep convection events (Pickart et al., 2003), thus also contributing to heat exchange with the deep ocean.

A first evaluation of the influence of modes of climate variability on the observed and simulated OHC is performed in the whole instrumental period (e.g. 1955-2010). For this analysis, three well-known modes of SST variability are explored, namely, ENSO (represented by El Niño 3.4 index), PDO and AMO, along with the NAO. All the observed climate indices are obtained from NOAA/OAR/ESRL Physical Sciences Division[‡]. In the forced simulations, the climate indices are calculated following their respective definitions. ENSO corresponds to El Niño 3.4 index, defined as the mean SST value from 5°S to 5°N and 170° to 120°W (Trenberth, 1997). The PDO index is derived as the leading PC of monthly SST anomalies in the North Pacific Ocean, poleward of 20°N (Mantua et al., 1997). And finally, the AMO is defined as the detrended average of Atlantic SST anomalies north of the Equator (Enfield et al., 2001). For the calculation of all these indices, the local SST anomalies are calculated with respect to the global SST mean, thus filtering out the influence of the global warming signal and only representing the internal natural variability (Zhang et al., 1997). Finally, the NAO is calculated as the leading mode of SLP anomalies in the North Atlantic (Wallace and Gutzler, 1981).

The corresponding OHC fingerprints are illustrated in the regression patterns of Figure 5.16. Both the observed ENSO and PDO indices show similar patterns, with the former showing stronger equatorial anomalies, and the latter larger impact in the North Pacific. Generally, both patterns are associated with an eastern warming and a western cooling of the upper Pacific ocean that could explain the local shift in OHC trends from 1955-1990 to 1991-2010 (see Figure 5.3). In contrast, in the model the zonal dipole structure is only observed at the Equator for the ENSO index, and at the North Pacific for the PDO, suggesting that the model cannot capture the coupling between both modes (Newman et al., 2003). Regarding the AMO, it relates in the observations to positive OHC anomalies over the whole Atlantic, but shows no significant changes in FOR1+A2. This probably indicates that, given the limited time period, no relevant changes of this index are taking place in the simulations. The most significant impact of the NAO in the observations is a cooling over the Labrador and Irminger Seas, that is partly reproduced in the simulations. These also simulate an OHC increase at midlatitudes, similar to the one already described in response to the radiative forcing (Figure 5.9). Therefore, this imprint is more probably associated to the recent changes in the forcing, which may be also having an impact on the NAO. Besides, the final tendency to negative NAO values in the observations can explain the remarkable warming of the North Atlantic since year 1990 (see Figure

[‡] http://www.esrl.noaa.gov/psd/data/climateindices/list/

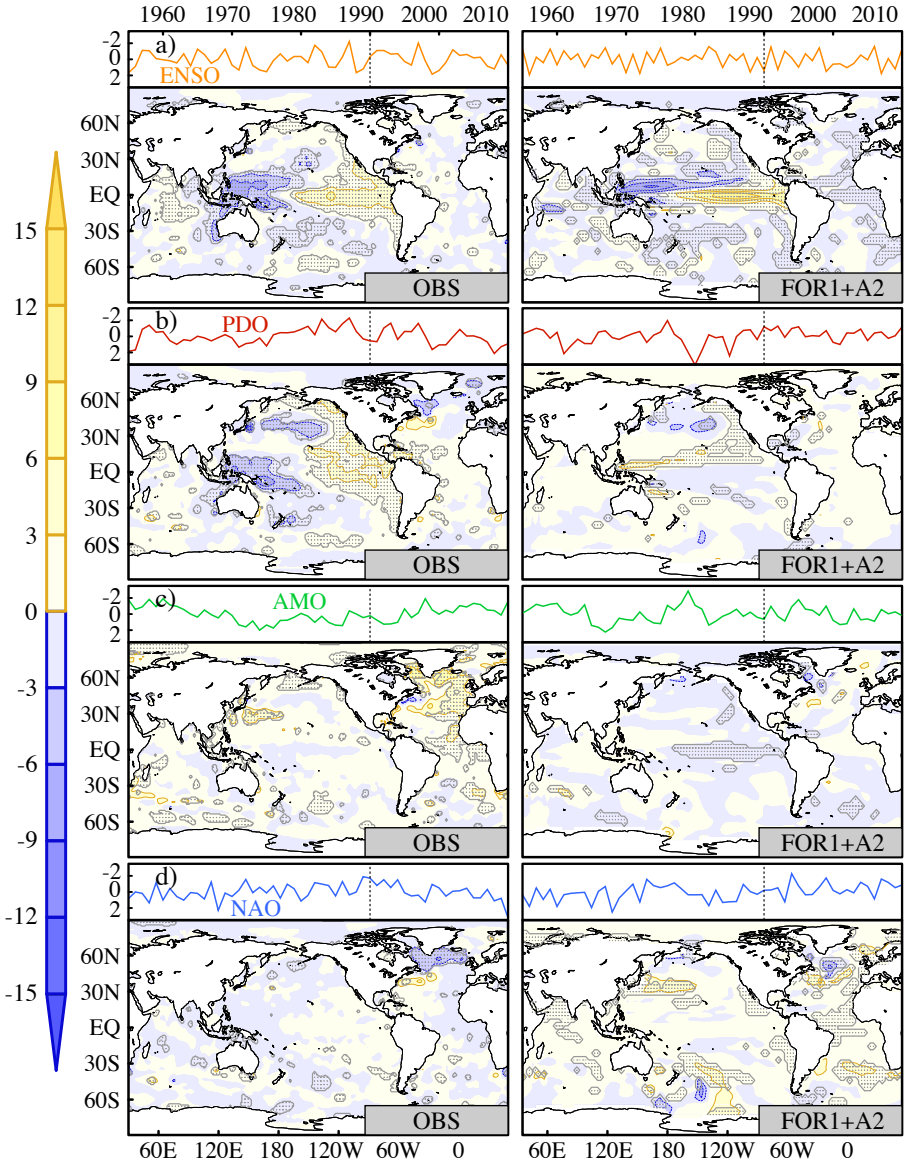

Fig. 5.16: *Top:* Observed (left) and simulated (right) standardised indices of: a) niño3.4; b) PDO; c) AMO; d) NAO. *Bottom:* Regression patterns between the anomalies of upper OHC (in $10^8 J/m^2$) and the same indices above. The calculation period is 1955-2010. Significance is addressed as in Fig. 5.8.

5.3). The analysis is on the following extended to the last thousand years, to better determine the spatial impacts associated to the previous modes and the predominant timescales of their influence.

5.3.2 Modes of climate variability and OHC in the last millenium

The regression patterns in Figure 5.16 are now calculated for the complete FOR2 simulation (Figure 5.17). The patterns corresponding to ENSO and the PDO are similar to those described during the observational period. Besides, the AMO is now related to a general warming in the North Atlantic, more in line with the OHC pattern described for the observations. It also shows a local cooling in the Labrador Sea and some positive OHC anomalies in the North Pacific, near the region where the PDO occurs. Similar features are also observed in the pattern of the NAO (Figure 5.17d). This suggests a link between the three modes in the model. Indeed, the AMO is known to be related to changes in the AMOC (Knight et al., 2005), which were found to be driven in the forced runs by changes in the NAO (see Chapter 4). Also, the interrelationship between the NAO and the Arctic Oscillation (AO) may explain an atmospheric influence over the North Pacific, and thereby on the PDO. The lead-lag relationship at low-frequencies between the previous indices in the model is explored in Figure 5.18. The NAO leads the AMO and PDO changes by 2 and 4 years, respectively. Furthermore, the radiative forcing is found to have a leading role on the NAO, which lags the total RF changes by about 1 year.

The influence of these modes in the OHC variations is now explored in a temporal and spectral perspective. For this, a cross-wavelet analysis is again employed (Figure 5.19). In the previous analysis of the forcings, that have a worldwide impact on the upper OHC, the coherence was established with respect to the global OHC integral. In this case, however, the different modes produce more localised influences, and thereby the coherence is investigated locally. Each index is compared with the OHC average in the region where its influence is originally taking place (dotted rectangles in Figure 5.17). For example, for ENSO, the OHC is averaged in the Equatorial Pacific. Both timeseries (i.e. ENSO and the OHC average) show a high degree of coherence at interannual timescales, and also relative good agreement from decadal to multidecadal timescales. Although in some particular periods (e.g. 1100-1300) coherence is damped above decadal timescales, overall ENSO explains most of OHC variability in the region. In contrast, both the PDO and AMO show a limited influence in the interannual OHC variability at their respective centers of action. Furthermore, both indices show alternating periods of good and poor coherence with the local OHC at multidecadal timescales. The fact that the phase of the relationships (arrows in Figure 5.19) remains stable throughout the whole simulation, with ‘easterlies’

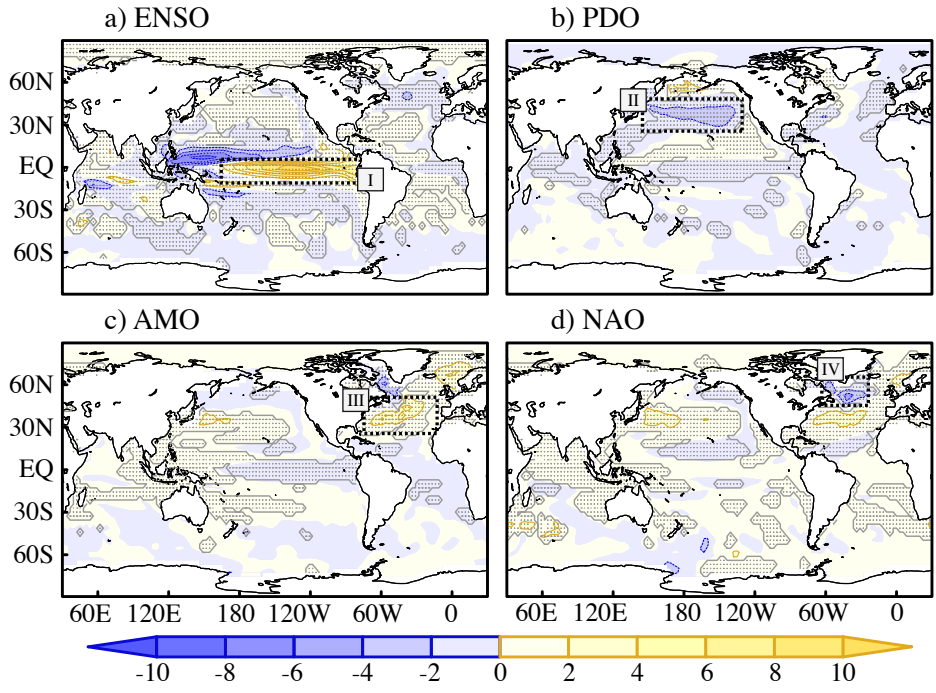

Fig. 5.17: Regression patterns between the anomalies of OHC in the upper 700 m (in $10^8 J/m^2$) and the standardised indices in the whole FOR2 simulation: a) niño3.4; b) PDO; c) AMO; d) NAO. Significance is addressed as in Fig. 5.8. The black dotted rectangles delimit the regions assessed in the cross-wavelet analysis of Fig. 5.19.

in Figure 5.19b accounting for a North Pacific cooling and 'westerlies' in Figure 5.19c representing a mid-latitude North Atlantic warming, both compatible with the corresponding OHC patterns in Figure 5.17, points to a real but intermittent modulation of the OHC by both indices. The reasons for this discontinuous influence are not clear to us, although some impact of the radiative forcing cannot be excluded. Indeed, Figure 5.9 showed that OHC in both regions, unlike in the equatorial latitudes, is particularly sensitive to changes in the radiative forcings. Finally, the NAO shows a good degree of coherence, although subject to some intermittences, with interannual and interdecadal OHC variability in the Labrador Sea. Interestingly, the phase of this relationship changes at different timescales. For periods up to 30 years, the 'easterlies' indicate a direct association between the NAO and a cooling over the Labrador Sea, as expected given the leading role

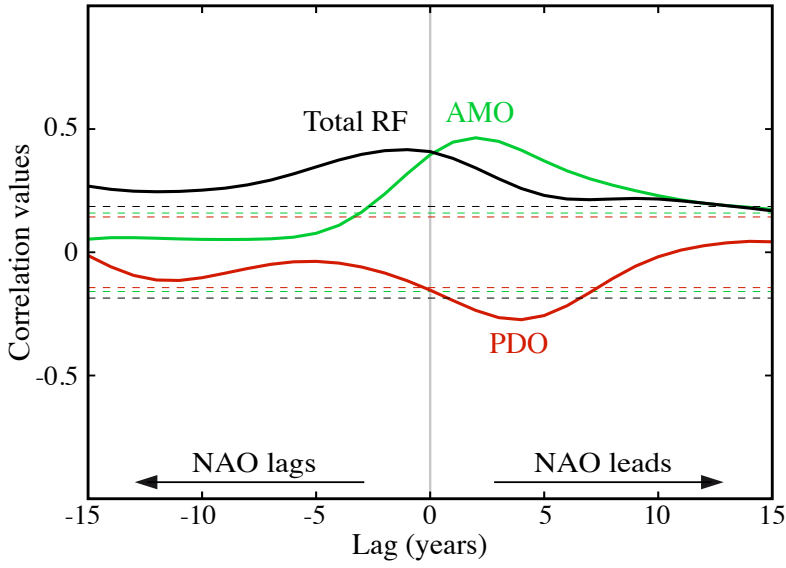

Fig. 5.18: Time-lag correlations between the decadally filtered indices of the NAO and the following timeseries: the PDO (red line), the AMO (green line) and the total radiative forcing (black line). The thin colored horizontal lines represent the threshold value for significance associated to each series. Significance is addressed as in Fig. 5.8.

of the NAO on the AMOC already discussed in Chapter 4. Besides, at longer timescales some periods (e.g. 1300-1500) give evidence of the contrary relationship. As the NAO has been found to respond to variations in the total radiative forcing (Figure 5.18), the Labrador warming observed at low frequencies could be actually attributed to the direct influence of this forcing.

5.4 Conclusions

The main aspects of the upper OHC variability, and its response to the external forcing and internal modes of climate variability have been assessed in a suite of observations and model simulations covering the period 1000 to 2100 AD.

Simulations are first evaluated in the instrumental period. Overall, the model overestimates the warming trend and underestimates the decadal OHC variability. The misrepresentation of trends is explained to some extent by the lack of

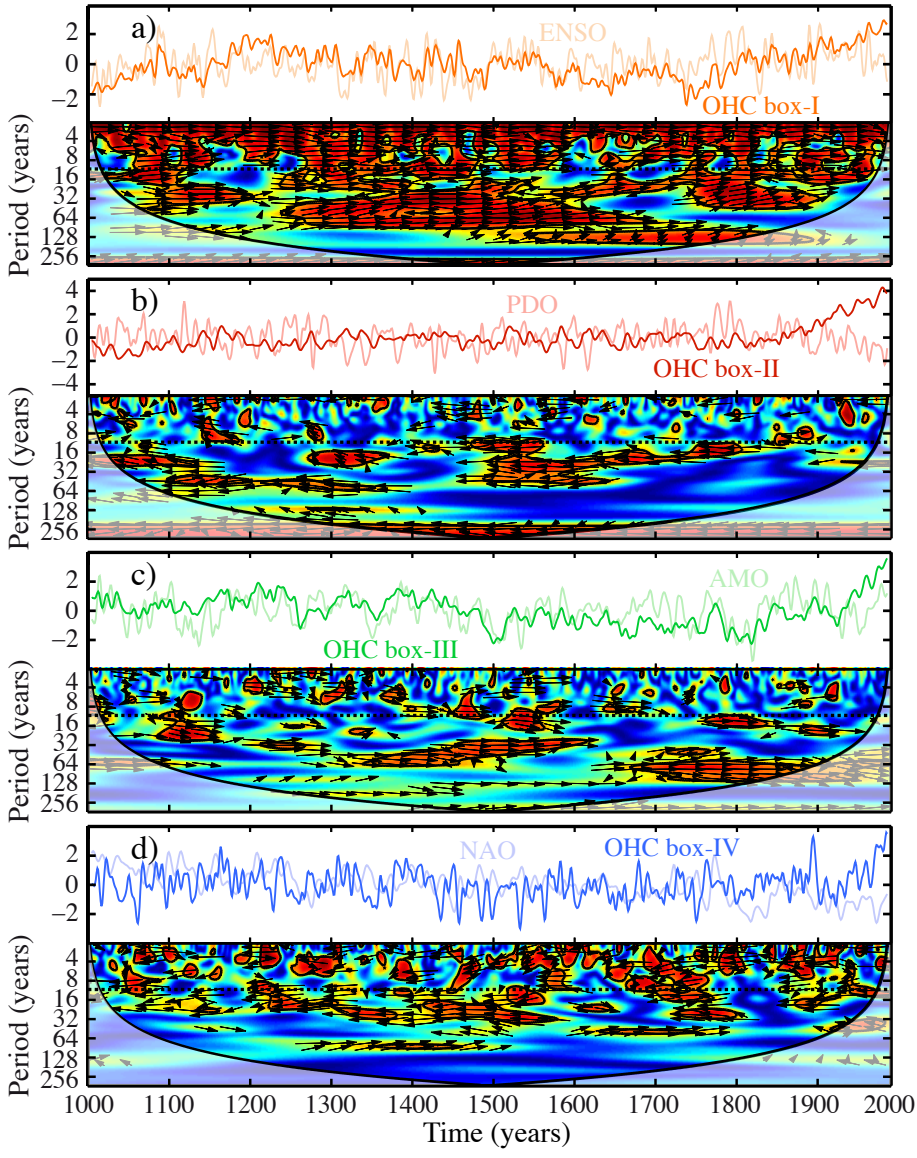

Fig. 5.19: The same as in Fig. 5.13 but between the standardised indices of ENSO, PDO, AMO and NAO and the OHC averages in the corresponding boxes defined in Fig. 5.17. In the top panels timeseries are detrended decadally to ease comparison at interdecadal timescales.

sulphate aerosols in the simulations, whose cooling effect is known to partially offset the GHG-driven warming (Delworth et al., 2005). The agreement at decadal timescales could also be improved, as indicated by Gregory et al. (2004), by establishing the OHC comparison within the mask of well-observed regions in the ocean. The spatial distribution and intensity of the upper warming trends have changed from 1955-2010 to 1991-2010. These changes respond, respectively, to a sustained increase of the net radiative forcing (mostly associated to an acceleration of GHG emissions) and a shift in the values of the PDO and AMO indices.

During the last millennium, the simulated OHC is subject to the effect of initial drifts. To assess the importance of these trends, the simulations have been compared with several reconstructions of SL variability, the only proxy available with a direct relationship with the OHC. Since the model is not able to reproduce the changes in the melting of land ice sheets, only the thermosteric component has been considered. The comparison with the SL proxies has allowed for a drift correction since year 1700. Besides, the model suggests that thermal expansion has only contributed to one sixth of the total observed sea level rise in the last 200 years. Also, to minimise the effect of the drift, the subsequent analysis concerning the OHC throughout the last millennium is focused on the upper 700 m of the FOR2 simulation.

The spatial imprint of the radiative forcing has been explored. All the individual forcings show a similar impact, with larger effect at extratropical latitudes. This larger response at midlatitudes is partly explained by a local reduction in cloud cover, thus allowing a larger fraction of solar radiation to reach the ocean surface. Other contributions to the net surface heat flux, such as the outgoing longwave radiation or the sensible and latent heat fluxes do not reproduce this different latitudinal response. In the preindustrial era, most of the forced OHC variability is associated to volcanism, with some solar contribution at interdecadal timescales (periods from 10 to 30 years). After 1850, low-frequency OHC variability is mainly responding to the increased GHG concentrations, and the influence of volcanic activity remains important at decadal and intradecadal timescales. Interestingly, the ocean shows a delayed response to all the radiative forcings, with the largest impacts occurring about 2, 20 and 70 years after the changes in volcanic, solar and GHG forcing, respectively.

Finally, the contributions from several natural modes of climate variability has been determined. The influence of ENSO is mainly localised in the Equatorial Pacific, where it dominates the local OHC variability from interannual to multidecadal timescales. This predominant role of ENSO to drive local OHC variability at all timescales is in line with a major contribution of internal variability in the Tropics, and a largest impact of the external forcing at extratropical latitudes.

Likewise, positive PDO and AMO indices relate respectively to a cooling in the North Pacific, and warming at midlatitudes in the North Atlantic, both modes contributing discontinuously to OHC variability at multidecadal timescales. The NAO, in the model and observations, produces a cooling over the Labrador Sea, that in the simulations gives rise to a strengthening of the AMOC cell. This impact takes place from interannual to interdecadal timescales. To conclude, the fact that natural modes of climate variability, such as ENSO, PDO or AMO can impact the OHC globally or locally is important in the coming decades, since they can temporarily mitigate or intensify the ocean warming signal, and also can locally modulate the global sea level rise.

6

Conclusions and discussion

De la mar al percepto,
del percepto al concepto,
del concepto a la idea,
–¡oh, la linda tarea! –,
de la idea a la mar.
¡Y otra vez a empezar!

Antonio Machado. Campos de Castilla. 1912

This thesis has assessed the main aspects of ocean variability and predictability at millennial timescales, with particular emphasis on the processes governing the strength of the Atlantic meridional overturning circulation, and also on the contributions to the variability of ocean heat content and thermal expansion throughout the last millennium. The work has been structured in three different but related topics, each explored in one specific chapter.

A summary of the main findings and specific conclusions of the different analyses in this work has been detailed at the end of the corresponding chapters. Also, throughout this thesis, some general issues emerged that are important for the interpretation of the results. In Section 6.1 both the main findings and their respective caveats are highlighted (in italics) and discussed in depth. Finally, an insight into the open questions for future work is given in Section 6.2.

6.1 Conclusions

Predictability of deep water formation, and thereby of the AMOC, can be largely controlled by the integration of heat fluxes in the North Atlantic. A regression model for the AMOC strength has been developed in CTRL1, based on two different predictors. The first is associated to persistent air-sea heat fluxes over the Eastern Labrador Sea. This local influence is integrated for the 10 years preceding the MOI changes. This index alone is able to explain more than 70% of the Ekman-filtered MOI variance. The second forerunner explains about an extra 10% of variance and is related to a buildup of positive density anomalies in the Western Irminger region, in turn related to changes in the outflows from the Nordic Seas, and the gyre in the vicinity of the Irminger Sea.

Predictive regression models based on the indices previously defined can reproduce the most important rapid MOI increases and decreases. However, different methods for the selection of predictors taking into account the asymmetric occurrence of such events can improve the performance of the prediction model. In CTRL1, the large, rapid AMOC changes are well described by the first predictor, although their magnitude tends to be underestimated. In contrast, the contribution of the second predictor is usually negligible. This indicates that other processes not included in the model may be more important for the onset of these rapid events. Also, the analysis has shown evidence of some asymmetric behaviour in the occurrence and impacts of the large decadal MOI increases and decreases. Therefore, a separate analysis of the largest increases and decreases is recommended to identify new predictors for the regression model.

The wind can play a major role in driving the AMOC variability at high and low frequencies. In the ECHO-G simulations, interannual AMOC variability is largely influenced by changes in the Ekman transport associated to three well-known modes of climate variability: ENSO, EA and NAO. Likewise, from decadal to secular timescales, AMOC variability responds to changes in Labrador convection, favoured in turn by a wind-driven cooling over the region. In the forced millennial simulations the wind changes, similar to those observed during the occurrence of tip-jet events south of Cape Farewell (Pickart et al., 2003), are ultimately forced by changes in the NAO, with a lead time of 1-2 years. Furthermore, the NAO produces a local decrease in the OHC, reproduced both in the simulations and the observations.

Natural modes of climate variability can produce remarkable local changes in the upper OHC. Besides the effect of the NAO, already described above, ENSO and PDO variability relate respectively to a tropical warming and extratropi-

cal cooling in the Pacific ocean, while the AMO is associated to a general OHC increase at midlatitudes in the North Atlantic. However, there are significant differences in the predominant timescales of the previous impacts. While ENSO dominates the local OHC variability at all frequencies, both the PDO and AMO show intermittent impacts on the OHC, mostly at multidecadal timescales.

The mechanisms and interactions can be specific to the model and experiments considered, and thereby need to be interpreted within the model biases and shortcomings. Inferences about the particular regions, the specific mechanisms and their corresponding timescales would require further evidence from other models and paleo-reconstructions. In the ECHO-G model the representation of ocean dynamics and thereby of deep water formation is limited both by the coarse resolution and by the fact that it is not eddy-resolving. The model misrepresents quantities as the overflow over the Greenland-Scotland Ridge (0-3 Sv, Figures 3.1 and 4.1), or the intensity of the subpolar gyre (∼15 Sv), both below the range of observational estimates of 6 Sv (Olsen et al., 2008) and 25 to 40 Sv (Clarke, 1984; Reynaud et al., 1995; Bacon, 1997), respectively. In particular, the realism of the overflows is constrained by the inaccurate representation of ocean topography (e.g. Roberts and Wood, 1997). Likewise, deep convection is generally weak in the North Atlantic as compared to observations (Marshall and Schott, 1999), and locally overestimated over the Central Irminger Sea. As a result of the different unresolved processes, the typical timescales of the mechanisms described herein might be rather long. Indeed, latitudinal propagation of overturning anomalies is significantly faster in eddy-permitting models, due to a better representation of fast boundary waves (Getzlaff et al., 2005). Despite all these uncertainties, our results are physically consistent, and thereby illustrate processes and mechanisms with a potential contribution to real ocean variability.

The influence of initial conditions can hinder the analysis of forced simulations, in particular when the deep ocean is involved. This effect is especially clear in FOR1, that starts unusually warm due to too short a spin-down period insufficient to bring the model to an equilibrium state with the forcing conditions in 1000 AD. In quantities with an evident initial drift, the target period for the analysis has been shortened accordingly. In the particular case of the ocean heat content, given the persistent effect of the starting conditions in FOR1, the whole analysis at millennial timescales has leaned on the FOR2 simulation, which proved to start with a steadier ocean state.

Changes in the model version employed can also introduce significant differences in the simulated climatology and internal variability. Two different CTRL

simulations have been used in this study, run under different versions of the ECHO-G model. The notable discrepancies in the respective longterm mean ocean states call for caution when extrapolating the results and mechanisms in Chapter 3 to Chapter 4. For example, Figure 6.1a shows evidence of a stronger AMOC cell in CTRL2, associated to an intensification of the GSR overflow. Also, remarkable differences are observed in the convection regions (Figure 6.1b), with less convective activity south of Greenland, and enhanced activity in the Inner Labrador, the Irminger and the Nordic Seas. Therefore, potential changes in the driving mechanisms of the AMOC, both spatial (e.g. the deep convection sites) and temporal (e.g. integration period of heat flux anomalies), should be expected from CTRL1 to CTRL2.

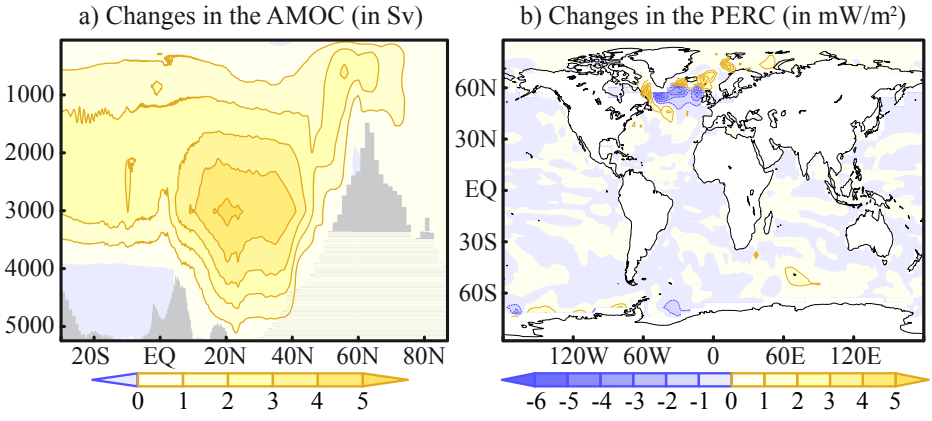

Fig. 6.1: Long-term differences between CTRL2 and CTRL1 for the: a) AMOC streamfunction (in Sv); b) Potential Energy Released by Convection (PERC, in mW/m^2).

In the last millennium, the GHG forcing produces the largest impacts in the ocean. Starting in the Industrial Era and continuing in the future scenarios, the AMOC experiences a final decrease of up to 40% with respect to the preindustrial average, following a weakening of Labrador convection due to reduced evaporation and increased precipitation at high latitudes. This estimate is within the range of future projections with different climate models (Schmittner et al., 2005; Schneider et al., 2007). Likewise, the future scenario simulations predict a thermal expansion of 0.14-0.17 m during the 21^{st} century. A rough estimate of the additional contributions to sea level rise not represented by the model (e.g.

melting from glaciers and land ice sheets) can be made by establishing a comparison with sea level reconstructions in the past 200 years (Jevrejeva et al., 2008a; Church and White, 2011). In this period, simulated thermal expansion represents a sixth of the total observed sea level rise. The ratio increases to one third in the period 1955-2010, but it is most probably overestimated due to the missing effect of sulfur aerosols. Indeed, comparison with observations of thermal expansion in this same period also suggest a contribution of about one sixth. Assuming that this ratio holds during the 21^{st} century, the total sea level rise would be in the order of one meter, well above the values reported in the IPCC 4th Assessment Report (Meehl et al., 2007). Yet, this simple estimate is in the range of recent global sea level projections (Rahmstorf, 2007; Pfeffer et al., 2008; Vermeer and Rahmstorf, 2009; Grinsted et al., 2010; Jevrejeva et al., 2010). The unresolved contribution of continental ice melting prevents, however, a rigorous sea level budget in the ECHO-G simulations. These missing processes can also affect the representation of other quantities, like the AMOC. If Greenland ice sheet melting was represented, the associated freshwater input would act to hamper deep convection, thus probably accelerating the simulated weakening of the AMOC strength throughout the 21^{st} century.

In the absence of anthropogenic forcing, the short-lived volcanic aerosols tend to produce larger impacts than the slowly varying solar irradiation. During the preindustrial period, volcanic forcing dominates the radiative response from interannual to multidecadal timescales (see Figure 5.14). In contrast, the impact of solar activity is considerably smaller. In the ECHO-G simulations, the cooling signal of volcanoes penetrates slowly into the ocean, where it persists for about a decade (Figure 4.13). The integration of this signal in periods of intense volcanism (e.g. 1150-1300 AD) introduces multidecadal changes in upper ocean temperature, and thereby in the OHC. The upper ocean cooling in the convection regions of the North Atlantic also induce a dynamical oceanic response to the largest volcanoes, that produce a slight strengthening of the whole AMOC circulation (see Figure 4.11b). However, the magnitude of this dynamic response is significantly weaker than that observed for the increasing GHGs. The lower sensitivity of the AMOC to the moderate forcing (e.g. solar irradiance and volcanic aerosols), is probably fostered by misrepresented deep convection in the model, given the lesser role that the high latitudes (more sensitive to the forcing) are found to play on deep water formation.

The main sources of uncertainty concerning the analysis of the forced response reside on the reconstructions considered, the model resolution and the methodologies applied. The range of solar variability between the Maunder Minimum

and the present climate has been reduced in a factor of 2-4 by recent estimates (Wang et al., 2005; Krivova et al., 2007; Tapping et al., 2007), as compared to the ones employed herein (Lean et al., 1995; Crowley, 2000). These new estimates should significantly weaken the global response in temperature, and thus reduce the global and local influence on the OHC. A significant AMOC response to these weaker temperature changes is therefore more unlikely. Also, the ocean impact of volcanic aerosols might be underestimated in the model because of the low-resolution, the simplified physics and the smoothing effect of composite averaging. The timing and latitude of the different eruptions could not be prescribed, since the volcanic forcing is included as a direct modulation of the solar constant. Therefore, only the most general effect of volcanoes can be reproduced in the ECHO-G simulations. In line with our findings, other works analysing large individual eruptions (e.g. Tambora, Pinatubo, Krakatoa) find a deep cooling signal persisting for several decades (Gleckler et al., 2006a,b), that may have a large impact on the AMOC (Stenchikov et al., 2009). The Bergen climate model, with a higher resolved atmospheric component, also shows a remarkable AMOC strengthening, caused both by the direct radiative cooling, and a volcanic modulation of the NAO (Ottera et al., 2010). Yet, one of the main open questions is to determine whether and how the AMOC responds to the increasing GHG concentrations, given the uncertainty in the future emissions (Nakicenovic et al., 2000) and the complexity of the feedback mechanisms involved. Indeed, in response to identical future scenarios, different models simulate somewhat different changes (Schmittner et al., 2005; Schneider et al., 2007). The multi-model spread is rather large, but no model predicts an abrupt change or a complete shutdown of the AMOC within the next century (Meehl et al., 2007), as observed in the ECHO-G simulations. Finally, the potential effect of other forcing factors is discussed. None of the forced simulations incorporate the influence from sulphate aerosols, which probably results in an overestimation of both the ocean warming and AMOC weakening (Delworth and Dixon, 2006) since the beginning of the industrial era. Changes in the vegetation cover, which have been found to attenuate the industrial warming trend in other GCM simulations (Bauer et al., 2003), were not included either. The associated cooling could also influence the variability of the AMOC, but the nature and magnitude of this change remains still uncertain.

6.2 Open questions and lines for future work

The current analysis is based on a set of different experiments with the ECHO-G model. These simulations, in turn, are forced by a particular selection of external forcing factors. This allowed for concentrating on the particularities of internal

ocean variability and forced response as represented by this specific model and setup. Although the main shortcomings and their influences have been discussed, an exhaustive assessment of both model and forcing related uncertainties ideally requires a comprehensive study including millennial simulations with other state-of-the-art models covering the whole range of forcing configurations, as well as a joint evaluation with ocean proxy evidence in the same period.

Thereby, a first natural continuation of this work would be to extend the model inter-comparison effort started in González-Rouco et al. (2011) analysing the main aspects of the MCA-LIA transition to key ocean variables like the ones studied herein. This study would be particularly important for the AMOC, given the limited knowledge of both its past variability throughout the last millennium and its sensitivity to the different forcings. Of especial interest is to determine if the AMOC played an active role during the Little Ice Age. Indeed, some proxy reconstructions suggest an AMOC slowdown may have been partly responsible for the anomalously cold climate in the North Atlantic during the LIA, by diminishing the meridional heat transport to high latitudes (Broecker, 2000; Lund et al., 2006).

A limited evaluation of AMOC variability during the short observational period can be done at 26°N, where the monitoring RAPID array is located (Cunningham and Marsh, 2010). In the millennial simulations, a comparison of the specific ocean conditions preceding the onset of rapid AMOC increases and decreases in each model, would help to better confine the regions and quantities that can anticipate large and rapid AMOC variations in the real ocean. Regarding the heat content, an important aspect to determine is its intermodel range of variability during the last millennium, and its sensitivity to the different total equivalent radiative forcings considered.

Another important issue among the forced experiments, most important for studies of ocean heat content and sea level variability as evidenced by our study, is the effect of initial conditions in the first hundred years of the simulations. Given the long time required by the deep ocean to reach thermal equilibrium and the high computational cost of the simulations, the spin-down periods considered to drive the model to the desired forcing conditions are not usually long enough to avoid the presence of some initial drifts. A comparison of the different spin-down setups considered, and their respective initial trends in the deep ocean can shed light on the best strategy to save computational time, while minimising the influence of the drift.

Despite the evident climatic interest of the study of both the AMOC and the global OHC, the lack of direct proxy sources of their past variability recommends two additional lines of research. The first is to extend the model intercomparison analysis to other related variables with available paleo-reconstructions in the last millennium, such as the NAO (e.g. Trouet et al., 2009), the AMO (e.g. Gray et al., 2004) or the changes in SL (e.g. Jevrejeva et al., 2008a; Kemp et al., 2011). Also of interest are variables and proxies with a direct influence on Greenland's climate, given its potential relevance for global climate in the coming decades. Likewise, the second topic of research would be to analyse the mechanisms linking the variability of these different variables in the different models and simulations. For example, the impact of the NAO on Greenland and AMOC variability, or the relationship of this latter with the changes in the AMO.

Finally, the new lines for future work would also require new tools of analysis. For example, the use of advanced statistical methodologies such as complex empirical orthogonal functions (CEOFs) or principal oscillation patterns (POPs) may allow for a better description and improve the understanding on the internal AMOC oscillatory features, that will facilitate the identification of mechanism for phase reversal and their comparison among simulations. In particular, this also allows for the identification of the features of forced and unforced internal AMOC variability in transient and control experiments with the same model. Non-linear statistical techniques could also provide additional information on the evolution of the modes described, and more explicitly on the interaction between modes like the NAO and the AMOC. Besides, for model and proxy intercomparison, the use of time-frequency decomposition and classification techniques can help to identify the common aspects of their variability.

References

Ammann, C. M., F. Joos, D. Schimel, B. L. Otto-Bliesner, and R. A. Tomas, 2007: Solar influence on climate during the past millennium: Results from transient simulations with the ncar climate system model. *Proc. Natl. Acad. Sci.*, **104**, 3713–3718.

Bacon, S., 1997: Circulation and fluxes in the North Atlantic between Greenland and Ireland. *J. Phys. Oceanogr.*, **27**, 1420–1435.

Bacon, S., W. J. Gould, and Y. Jia, 2003: Open convection in the Irminger Sea. *Geophys. Res. Lett.*, **30**, 1246.

Baehr, J., K. Keller, and J. Marotzke, 2008: Detecting potential changes in the meridional overturning circulation at 26N in the Atlantic. *Climatic Change*, **91**, 11–27, doi:10.1007/s10584-006-9153-z.

Bard, E., G. Raisbeck, F. Yiou, and J. Jouzel, 2000: Solar irradiance during the last 1200 years based on cosmogenic nuclides. *Tellus B*, **52**, 985–992.

Barnett, T., D. Pierce, and R. Schnur, 2001: Detection of anthropogenic climate change in the world's oceans. *Science*, **292**, 270.

Barnett, T. P., D. W. Pierce, K. M. AchutaRao, P. J. Gleckler, B. D. Santer, J. M. Gregory, and W. M. Washington, 2005: Penetration of Human-Induced Warming into the World's Oceans. *Science*, **309**, 284–287.

Barnston, A. G. and R. E. Livezey, 1987: Classification, seasonality and persistence of low-frequency atmospheric circulation patterns. *Monthly Weather Review*, **115**, 1083–1126.

Bauer, E., M. Claussen, V. Brovkin, and A. Huenerbein, 2003: Assessing climate forcings of the earth system for the past millennium. *Geophys. Res. Lett.*, **30**, 1276, doi:10.1029/2002GL016639.

Beltrami, H., J. F. González-Rouco, and M. B. Stevens, 2006: Subsurface temperatures during the last millennium: Model and observation. *Geophys. Res. Lett.*, **33**, L09705, doi:10.1029/2006GL026050.

Bentsen, M., H. Drange, T. Furevik, and T. Zhou, 2004: Simulated variability of the atlantic meridional overturning circulation. *Clim. Dyn.*, **22**, 701–720.

Bindoff, N., J. Willebrand, V. Artale, A. Cazenave, J. Gregory, S. Gulev, K. Hanawa, C. Le Quere, S. Levitus, Y. Nojiri, C. Shum, L. Talley, and A. Unnikrishnan, 2007: Observations: oceanic climate change and sea level. *Climate change 2007: The Physical Science basis. Contribution of Working Group I to the Fourth Assessment Report of the Intergovernmental Panel on Climate Change,*, S. Solomon, D. Qin, M. Manning, Z. Chen, M. Marquis, K.B. Averyt, M. Tignor and H.L. Miller, Eds., Cambridge University Press, Cambridge, 385–432.

Bingham, R., C. Hughes, V. Roussenov, and R. Williams, 2007: Meridional coherence of the North Atlantic meridional overturning circulation. *Geophys. Res. Lett*, **34**, L23606, doi:10.1029/2007GL031731.

Bloomfield, P., 1976: *Fourier analysis of time series: An introduction*. New York: Wiley.

Bond, G., H. Heinrich, W. Broecker, L. Labeyrie, J. McManus, J. Andrews, S. Huon, R. Jantschik, S. Clasen, C. Simet, K. Tedesco, M. Klas, G. Bonani, and S. Ivy, 1992: Evidence for massive discharge of icebergs into the North Atlantic ocean during the last glacial period. *Nature*, **360**, 245–249.

Bond, G., W. Showers, M. Cheseby, R. Lotti, P. Almasi, P. Demenocal, P. Priore, H. Cullen, I. Hajdas, and G. Bonani, 1997: A pervasive millennial-scale cycle in North Atlantic Holocene and glacial climates. *Science*, **278**, 1257–1266, doi:10.1126/science.278.5341.1257.

Bretherton, C., M. Widmann, V. Dymnikov, J. Wallace, and I. Bladé, 1999: The effective number of spatial degrees of freedom of a time-varying field. *J. Clim.*, **12**, 1990–2009.

Briffa, K., F. Schweingruber, P. Jones, T. Osborn, S. Shiyatov, and E. Vaganov, 1998: Reduced sensitivity of recent tree-growth to temperature at high northern latitudes. *Nature*, **391**, 678–682.

Broecker, W., 1987: The biggest chill. *Nat. Hist. Mag.*, **97**, 74–82.

Broecker, W. S., 2000: Was a change in thermohaline circulation responsible for the Little Ice Age ? *Proc. Natl. Acad. Sci.*, **97**, 1339–1342.

Bryan, F., G. Danabasoglu, N. Nakashiki, Y. Yoshida, D.-H. Kim, J. Tsutsui, and S. C. Doney, 2006: Response of the North Atlantic Thermohaline Circulation and Ventilation to Increasing Carbon Dioxide in CCSM3. *J. Clim.*, **19**, 2382–2397.

Cabanes, C., T. Lee, and L.-L. Fu, 2008: Mechanisms of Interannual Variations of the Meridional Overturning Circulation of the North Atlantic Ocean. *J. Phys. Oceanogr.*, **38**, 467–480.

Church, J. and N. White, 2011: Sea-level rise from the late 19th to the early 21st century. *Surveys in Geophysics*, 1–18, doi:10.1007/s10712-011-9119-1.

Church, J. A., N. J. White, and J. M. Arblaster, 2005: Significant decadal-scale impact of volcanic eruptions on sea level and ocean heat content. *Nature*, **438**, 74–77.

Clarke, R. A., 1984: Transport through the Cape Farewell-Flemish Cap Section. *Rapp. P. V. Reun. Cons. Int. Explor. Mer.*, **185**, 120–130.

Colin de Verdière, A. and T. Huck, 1999: Baroclinic instability: An oceanic wavemaker for interdecadal variability. *J. Phys. Oceanogr.*, **29**, 893–910.

Crowley, T. and T. Lowery, 2000: How warm was the Medieval Warm Period? a comment on 'man-made versus natural climate change'. *AMBIO*, **39**, 51–54.

Crowley, T. J., 2000: Causes of climate change over the past 1000 years. *Science*, **289**, 270–277.

Crowley, T. J., S. K. Baum, K.-Y. Kim, G. C. Hegerl, and W. T. Hyde, 2003: Modeling ocean heat content changes during the last millennium. *Geophys. Res. Lett.*, **30**, 1932, doi:10.1029/2003GL017801.

Cubasch, U., G. Meehl, G. Boer, R. Stouffer, M. Dix, A. Noda, C. Senior, S. Raper, and K. Yap, 2001: *Projections of future climate change, in Climate Change 2001: The Scientific Basis: Contribution of Working Group I to the Third Assessment Report of the Intergovernmental Panel on Climate Change*, Edited by Houghton et *al.*, Cambridge University Press, New York. 525–582.

Cubasch, U., R. Voss, G. C. Hegerl, J. Waszkewitz, and T. J. Crowley, 1997: Simulation of the influence of solar radiation variations on the global climate with an ocean-atmosphere general circulation model. *Clim. Dyn.*, **13**, 757–767.

Cunningham, S. and R. Marsh, 2010: Observing and modeling changes in the Atlantic MOC. *WIREs Clim. Chang.*, **1**, 180–191.

Cunningham, S. A., T. Kanzow, D. Rayner, M. O. Baringer, W. E. Johns, J. Marotzke, H. R. Longworth, E. M. Grant, J. J. M. Hirschi, L. M. Beal, C. S. Meinen, and H. L. Bryden, 2007: Temporal variability of the Atlantic meridional overturning circulation at 26.5 N. *Science*, **317**, 935–938.

Curry, R., M. McCartney, and T. Joyce, 1998: Oceanic transport of subpolar climate signals to mid-depth subtropical waters. *Nature*, **391**, 575–577.

Dansgaard, W., S. Johnsen, H. Clausen, D. Dahl-Jensen, N. Gundestrup, C. Hammer, C. Hvidberg, J. Steffensen, A. Sveinbjornsdottir, and J. Jouzel, 1993: Evidence for general instability of past climate from a 250-kyr ice-core record. *Nature*, **364**, 218–220.

Delworth, T. and K. Dixon, 2006: Have anthropogenic aerosols delayed a greenhouse gas-induced weakening of the North Atlantic thermohaline circulation? *Geophys. Res. Lett.*, **33**, L02606, doi:10.1029/2005GL024980.

Delworth, T., R. Stouffer, K. Dixon, M. J. Spelman, T. Knutson, A. Broccoli, P. Kushner, and R. Wetherald, 2002: Review of simulations of climate variability and change with the GFDL R30 coupled climate model. *Clim. Dyn.*, **19**, 555–574.

Delworth, T. L. and R. J. Greatbatch, 2000: Multidecadal Thermohaline Circulation Variability driven by atmospheric surface flux forcing. *J. Clim.*, **13**, 1481–1495.

Delworth, T. L., S. Manabe, and R. J. Stouffer, 1993: Interdecadal Variations in the Thermohaline Circulation in a Coupled Ocean-Atmosphere Model. *J. Clim.*, **6**, 1993–2011.

Delworth, T. L. and M. E. Mann, 2000: Observed and simulated multidecadal variability in the Northern Hemisphere. *Clim. Dyn.*, **16**, 661–676.

Delworth, T. L., V. Ramaswamy, and G. Stenchikov, 2005: The impact of aerosols on simulated ocean temperature and heat content in the 20th century. *Geophys. Res. Lett.*, **32**, L24709, doi:10.1029/2005GLD024457.

Deshayes, J. and C. Frankignoul, 2008: Simulated variability of the circulation in theNorth Atlantic from 1953 to 2003. *J. Climate*, **21**, 4919–4933.

Dickson, R., J. Lazier, J. Meincke, P. Rhines, and J. Swift, 1996: Long-term coordinated changes in the convective activity of the North Atlantic. *Progress in Oceanography*, **38**, 241–295.

Domingues, C. M., J. A. Church, N. J. White, P. J. Gleckler, S. E. Wijffels, P. M. Barker, and J. R. Dunn, 2008: Improved estimates of upper-ocean warming and multi-decadal sea-level rise. *Nature*, **453**, 1090–1093, doi:10.1038/nature07080.

Dong, B. and R. T. Sutton, 2005: Mechanism of Interdecadal Thermohaline Circulation Variability in a Coupled Ocean-Atmosphere GCM. *J. Clim.*, **18**, 1117–1135.

— 2007: Enhancement of ENSO Variability by a Weakened Atlantic Thermohaline Circulation in a Coupled GCM. *J. Clim.*, **20**, 4920–4939.

Dong, B., R. T. Sutton, and A. A. Scaife, 2006: Multidecadal Modulation of El Niño-Southern Oscillation (ENSO) variance by Atlantic Ocean sea surface temperatures. *Geophys. Res. Lett.*, **33**, L08705, doi:10.1029/2006GL025766.

Drijfhout, S. and W. Hazeleger, 2007: Detecting Atlantic MOC Changes in an Ensemble of Climate Change Simulations. *J. Clim.*, **20**, 1571–1582.

Drijfhout, S. S., W. Hazeleger, F. Selten, and R. Haarsma, 2008: Future changes in internal variability of the Atlantic Meridional Overturning Circulation. *Clim. Dyn.*, **30**, 407–419, doi: 10.1007/s00382–007–0297–y.

Eden, C. and R. J. Greatbatch, 2003: A damped decadal oscillation in the North Atlantic climate system. *J. Clim.*, **16**, 4043–4060.

Eden, C. and T. Jung, 2001: North Atlantic Interdecadal Variability: Oceanic Response to the North Atlantic Oscillation (1865-1997). *J. Clim.*, **14**, 676–691.

Eden, C. and J. Willebrand, 2001: Mechanism of Interannual to Decadal Variability of the North Atlantic Circulation. *J. Clim.*, **14**, 2266–2280.

Enfield, D., A. Mestas-Nunez, and P. J. Trimble, 2001: The Atlantic multidecadal oscillation and its relation to rainfall and river flows in the continental U.S. *Geophys. Res. Lett.*, **28**, 2077–2080.

Esper, J., E. Cook, and F. Schweingruber, 2002: Low-frequency signals in long tree-ring chronologies for reconstructing past temperature variability. *Science*, **295**, 2250.

Etheridge, D., L. P. Steele, R. L. Langenfelds, R. Francey, J. Barnola, and V. Morgan, 1996: Natural and anthropogenic changes in atmospheric co2 over the last 1000 years from air in antarctic ice and firn. *J. Geophys. Res.*, **101**, 4115–4128.

Frankcombe, L. M., A. von der Heydt, and H. Dijkstra, 2010: North Atlantic Multidecadal Climate Variability: An investigation of dominant time scales and processes. *J. Clim.*, **23**, 3626–3638, doi:10.1175/2010JCLI3471.1.

Frankignoul, C. and K. Hasselmann, 1977: Stochastic climate models. Part II: Application to sea-surface temperature anomalies and thermocline variability. *Tellus*, **29**, 289–305.

Franklin, B., 1786: A letter from Dr. Benjamin Franklin, to Mr. Alphonsus le Roy, member of several academies, at Paris. Containing sundry maritime observations. *Transactions of the American Philosophical Society*, **2**, 294–329.

Ganachaud, A. and C. Wunsch, 2000: Improved estimates of global ocean circulation, heat transport and mixing from hydrographic data. *Nature*, **408**, 453–457.

Gates, W. L., 1992: AMIP: The Atmosphere Model Intercomparison Project. Technical Report 7, Program for Climate Model Diagnosis and Intercomparison, Lawrence Livermore National Laboratory, L-264, PO Box 808, Livermore, CA, 94550, USA.

Getzlaff, J., C. Böning, C. Eden, and A. Biastoch, 2005: Signal propagation related to the North Atlantic overturning. *Geophys. Res. Lett.*, **32**, L09602, doi:10.1029/2004GL021002.

Gleckler, P., K. AchutaRao, J. Gregory, B. Santer, K. Taylor, and T. Wigley, 2006a: Krakatoa lives: The effect of volcanic eruptions on ocean heat content and thermal expansion. *Geophys. Res. Lett*, **33**, L17702, doi:10.1029/2006GL026771.

Gleckler, P. J., T. Wigley, B. Santer, J. Gregory, K. AchutaRao, and K. E. Taylor, 2006b: Krakatoa's signature persists in the ocean. *Nature*, **439**, 675.

González-Rouco, F. J., H. Beltrami, E. Zorita, and M. B. Stevens, 2009: Borehole climatology: a discussion based on contributions from climate modeling. *Clim. Past.*, **5**, 97–127.

González-Rouco, F. J., H. Beltrami, E. Zorita, and H. von Storch, 2006: Simulation and inversion of borehole temperature profiles in surrogate climates: Spatial distribution and surface coupling. *Geophys. Res. Lett.*, **33**, L01703, doi:10.1029/2005GL024693.

González-Rouco, F. J., L. Fernández-Donado, C. C. Raible, D. Barriopedro, J. Luterbacher, J. Jungclaus, D. Swingedouw, J. Servonnat, E. Zorita, S. Wagner, and C. Ammann, 2011: Medieval Climate Anomaly to Little Ice Age transition as simulated by current climate models. *Pages*, **19**, 7–8.

González-Rouco, J. F., H. von Storch, and E. Zorita, 2003a: Deep soil temperature as proxy for surface air-temperature in a coupled model simulation of the last thousand years. *Geophys. Res. Lett.*, **30**, 2116–2119.

González-Rouco, J. F., E. Zorita, U. Cubasch, H. von Storch, I. Fisher-Bruns, F. Valero, J. P. Montavez, U. Schlese, and S. Legutke, 2003b: Simulating the climate since 1000 AD with the AOGCM ECHO-G. *ESA*, **SP 535**, 329–338.

Goosse, H., T. Crowley, E. Zorita, C. Ammann, H. Renssen, and E. Driesschaert, 2005: Modelling the climate of the last millennium: What causes the differences between simulations? *Geophys. Res. Lett.*, **32**, L06710.

Gouirand, I., A. Moberg, and E. Zorita, 2007b: Climate variability in Scandinavia for the past millennium simulated by an atmosphere-ocean general circulation model. *Tellus*, **59A**, 30–49.

Gouirand, I., V. Moron, and E. Zorita, 2007a: Teleconnections between ENSO and North Atlantic in an ECHO-g simulation of the 1000-1990 period. *Geophys. Res. Lett.*, **34**, L06705,doi:10.1029/2006GL028 852.

Grassl, H., 2001: *Ocean circulation and climate*, Academic Press, volume 77 of *International Geophysics Series*, chapter Climate and Oceans. 3–9.

Gray, S., L. Graumlich, J. Betancourt, and G. Pederson, 2004: A tree-ring based reconstruction of the Atlantic Multidecadal Oscillation since 1567 AD. *Geophys. Res. Lett.*, **31**, L12205.

Gregory, J., 2010: Long-term effect of volcanic forcing on ocean heat content. *Geophys. Res. Lett.*, **37**, L22701, doi:10.1029/2010GL045507.

Gregory, J. M., H. T. Banks, P. A. Stott, J. A. Lowe, and M. D. Palmer, 2004: Simulated and observed decadal variability in ocean heat content. *Geophys. Res. Lett.*, **31**, L15312, doi:10.1029/2004GL020258.

Gregory, J. M., K. W. Dixon, R. J. Stouffer, A. J. Weaver, E. Driesschaert, M. Eby, T. Fichefet, H. Hasumi, A. Hu, J. H. Jungclaus, I. V. Kamenkovich,

A. Levermann, M. Montoya, S. Murakami, S. Nawrath, A. Oka, A. P. Sokolov, and R. B. Thorpe, 2005: A model intercomparison of changes in the Atlantic thermohaline circulation in response to increasing atmospheric CO2 concentration. *Geophys. Res. Lett.*, **32**, L12703, doi:10.1029/2005GL023209.

Gregory, J. M., J. A. Lowe, and S. F. B. Tett, 2006: Simulated global-mean sea level changes over the last half-millennium. *J. Clim.*, **19**, 4576–4591.

Griffies, S. and K. Bryan, 1997: A predictability study of simulated North Atlantic multidecadal variability. *Clim. Dyn.*, **13**, 459–487.

Griffies, S. M. and E. Tziperman, 1995: A Linear Thermohaline Oscillator Driven by Stochastic Atmospheric Forcing. *J. Clim.*, **8**, 2440–2453.

Grinsted, A., J. Moore, and S. Jevrejeva, 2004: Application of the cross wavelet transform and wavelet coherence to geophysical time series. *Nonlinear Processes in Geophysics*, **11**, 561–566.

Grinsted, A., J. C. Moore, and S. Jevrejeva, 2010: Reconstructing sea level from paleo and projected temperatures 200 to 2100 AD. *Clim. Dyn.*, **34**, 461–472, doi:10.1007/s00382-008-0507-2.

Guemas, V. and D. Salas-Mélia, 2008: Simulation of the Atlantic meridional overturning circulation in an atmosphere–ocean global coupled model. Part I: a mechanism governing the variability of ocean convection in a preindustrial experiment. *Clim. Dyn.*, **31**, 29–48, doi:10.1007/s00382-007-0336-8.

Hall, A. and R. Stouffer, 2001: An abrupt climate event in a coupled ocean–atmosphere simulation without external forcing. *Nature*, **409**, 171–174.

Hansen, B. and S. Østerhus, 2000: North Atlantic-Nordic seas exchanges. *Progress in Oceanography*, **45**, 109–208.

Hansen, J., L. Nazarenko, R. Ruedy, M. Sato, J. Willis, A. D. Genio, D. Koch, A. Lacis, K. Lo, S. Menon, T. Novakov, J. Perlwitz, G. Russell, G. A. Schmidt, and N. Tausnev, 2005: Earth's energy imbalance: Confirmation and implications. *Science*, **308**, 1431–1435.

Hasselmann, K., 1976: Stochastic climate models. Part I: Theory. *Tellus*, **28**, 473–484.

Hawkins, E. and R. Sutton, 2007: Variability of the Atlantic thermohaline circulation described by three-dimensional empirical orthogonal functions. *Clim. Dyn.*, **29**, 745–762.

— 2008: Potential predictability of rapid changes in the Atlantic meridional overturning circulation. *Geophys. Res. Lett.*, **35**, L11603, doi:10.1029/2008GL034059.

Heinrich, H., 1988: Origin and consequences of cyclic ice rafting in the northeast Atlantic Ocean during the past 130,000 years. *Quaternary Research*, **29**, 142–152.

Hermanson, L. and R. Sutton, 2010: Case studies in interannual to decadal climate predictability. *Climate Dynamics*, **35**, 1169–1189, doi:10.1007/s00382-009-0672-y.

Hermanson, L. and R. T. Sutton, 2009: Climate predictability in the second year. *Phil. Trans. R. Soc. A*, **367**, 913–916, doi:10.1098/rsta.2008.0181.

Hirschi, J. J.-M., P. D. Killworth, and J. R. Blundell, 2007: Subannual, Seasonal, and Interannual Variability of the North Atlantic Meridional Overturning Circulation. *J. Phys. Oceanogr.*, **37**, 1246–1265.

Hofer, D., C. C. Raible, and T. F. Stocker, 2011: Variations of the Atlantic meridional overturning circulation in control and transient simulations of the last millennium. *Clim. Past.*, **7**, 133–150, doi:10.5194/cp-7-133-2011.

Ishii, M. and M. Kimoto, 2009: Reevaluation of historical ocean heat content variations with time-varying XBT and MBT depth bias corrections. *Journal of Oceanography*, **65**, 287–299.

Jansen, E., J. Overpeck, K. Briffa, J.-C. Duplessy, F. Joos, V. Masson-Delmotte, D. Olago, B. Otto-Bliesner, W. Peltier, S. Rahmstorf, R. Ramesh, D. Raynaud, D. Rind, O. Solomina, R. Villalba, and D. Zhang, 2007: *Climate Change 2007: The Physical Science Basis. Contribution of Working Group I to the Fourth Assessment Report of the Intergovernmental Panel on Climate Change*, edited by S. Solomon and D. Qin and M. Manning and Z. Chen and M. Marquis and K.B. Averyt and M. Tignor and H.L. Miller, Cambridge University Press, Cambridge, United Kingdom and New York, NY, USA., chapter Palaeoclimate.

Jevrejeva, S., A. Grinsted, and J. C. Moore, 2009: Anthropogenic forcing dominates sea level rise since 1850. *Geophys. Res. Lett.*, **36**, L20706, doi:10.1029/2009GL040216.

Jevrejeva, S., J. Moore, and A. Grinsted, 2010: How will sea level respond to changes in natural and anthropogenic forcings by 2100. *Geophys. Res. Lett.*, **37**, L07703.

Jevrejeva, S., J. Moore, A. Grinsted, and P. Woodworth, 2008a: Recent global sea level acceleration started over 200 years ago. *Geophys. Res. Lett.*, **35**, L08715, doi:10.1029/2008GL033611.

Jevrejeva, S., J. C. Moore, and A. Grinsted, 2008b: Relative importance of mass and volume changes to global sea level rise. *J. Geophys. Res.*, **113**, D08105, doi:10.1029/2007JD009208.

Jones, P., K. Briffa, T. Barnett, and S. Tett, 1998: High-resolution palaeoclimatic records for the last millennium: interpretation, integration and comparison with general circulation model control-run temperatures. *The Holocene*, **8**, 455.

Jones, P. and M. Mann, 2004: Climate over past millennia. *Rev. Geophys.*, **42**, 1–42.

Jungclaus, J. H., H. Haak, M. Latif, and U. Mikolajewicz, 2005: Arctic-North Atlantic Interactions and Multidecadal Variability of the Meridional Overturning Circulation. *J. Clim.*, **18**, 4013–4031.

Jungclaus, J. H., S. J. Lorenz, C. Timmreck, C. H. Reick, V. Brovkin, K. Six, J. Segschneider, M. A. Giorgetta, T. J. Crowley, J. Pongratz, N. A. Krivova, L. E. Vieira, S. K. Solanki, D. Klocke, M. Botzet, M. Esch, V. Gayler, H. Haak, T. J. Raddatz, E. Roeckner, R. Schnur, H. Widmann, M. Claussen, B. Stevens, and J. Marotzke, 2010: Climate and carbon-cycle variability over the last millennium. *Clim. Past.*, **6**, 723–737, doi:10.5194/cp-6-723-2010.

Kanzow, T., S. A. Cunningham, W. E. Johns, J. J.-M. Hirschi, J. Marotzke, M. O. Baringer, C. S. Meinen, M. P. Chidichimo, C. Atkinson, L. M. Beal, H. L. Bryden, and J. Collins, 2010: Seasonal variability of the Atlantic Meridional Overturning Circulation at 26.5 °N. *J. Clim.*, **23**, 5678–5698, doi:10.1175/2010JCLI3389.1.

Kanzow, T., S. A. Cunningham, D. Rayner, J. J. M. Hirschi, W. E. Johns, M. O. Baringer, H. L. Bryden, L. M. Beal, C. S. Meinen, and J. Marotzke, 2007: Observed flow compensation associated with the MOC at 26.5 N in the Atlantic. *Science*, **317**, 938–941.

Katsman, C. and G. van Oldenborgh, 2011: Tracing the upper ocean's "missing heat". *Geophys. Res. Lett.*, **38**, L14610, doi:10.1029/2011GL048417.

Keenlyside, N., M. Latif, J. Jungclaus, L. Kornblueh, and E. Roeckner, 2008: Advancing decadal-scale climate prediction in the North Atlantic sector. *Nature*, **453**, 84–88, doi:10.1038/nature06921.

Keigwin, L. and E. Boyle, 2000: Detecting Holocene changes in thermohaline circulation. *Proc. Natl. Acad. Sci.*, **97**, 1343–1346.

Kemp, A., B. Horton, J. Donnelly, M. E. Mann, M. Vermeer, and S. Rahmstorf, 2011: Climate related sea-level variations over the past two millennia. *Proc. Natl. Acad. Sci.*, **published online**, 1–6, doi:10.1073/pnas.1015619108.

Kerr, R., 2000: A North Atlantic climate pacemaker for the centuries. *Science*, **288**, 1984–1986.

Knight, J. R., R. J. Allan, C. K. Folland, M. Vellinga, and M. E. Mann, 2005: A signature of persistent natural thermohaline circulation cycles in observed climate. *Geophys. Res. Lett.*, **32**, L20708, doi:10.1029/2005GL024233.

Knight, J. R., C. K. Folland, and A. A. Scaife, 2006: Climate impacts of the Atlantic Multidecadal Oscillation. *Geophys. Res. Lett.*, **33**, L17706.

Kravtsov, S. and M. Ghil, 2004: Interdecadal Variability in a Hybrid Coupled Ocean–Atmosphere–Sea Ice Model. *J. Phys. Oceanogr.*, **34**, 1756–1775.

Krivova, N., L. Balmaceda, and S. Solanki, 2007: Reconstruction of solar total irradiance since 1700 from the surface magnetic flux. *Astronomy and Astrophysics*, **467**, 335–346, doi:10.1051/0004-6361:20066725.

Kuhlbrodt, T., A. Griesel, M. Montoya, A. Levermann, M. Hofmann, and S. Rahmstorf, 2007: On the driving processes of the Atlantic meridional overturning circulation. *Rev. Geophys.*, **45**, RG2001.

Kushnir, Y., 1994: Interdecadal Variations in North Atlantic Sea Surface Temperature and Associated Atmospheric Conditions. *J. Clim.*, **7**, 141–157.

Latif, M., M. Botzet, M. Esch, H. Haak, S. Hagemann, J. Jungclaus, S. Legutke, S. Marsland, and U. Mikolajewicz, 2004: Reconstructing, monitoring, and predicting multidecadal-scale changes in the North Atlantic Thermohaline Circulation with sea surface temperature. *J. Clim.*, **17**, 1605–1614.

Lean, J., J. Beer, and R. Bradley, 1995: Reconstruction of solar irradiance since 1610: Implications for climate change. *Geophys. Res. Lett.*, **22**, 3195–3198.

Legutke, S. and R. Voss, 1999: The Hamburg Atmosphere-Ocean Coupled Circulation Model ECHO-G. Technical Report 18, DKRZ, Hamburg, Germany.

Levermann, A., A. Griesel, M. Hofmann, M. Montoya, and S. Rahmstorf, 2005: Dynamic sea level changes following changes in the thermohaline circulation. *Clim. Dyn.*, **24**, 347–354.

Levitus, S., J. Antonov, and T. Boyer, 2005a: Warming of the world ocean, 1955-2003. *Geophys. Res. Lett.*, **32**, L02604, doi:10.1029/2004GL021592.

Levitus, S., J. Antonov, T. Boyer, H. E. Garcia, and R. A. Locarnini, 2005b: EOF analysis of upper ocean heat content, 1956-2003. *Geophys. Res. Lett.*, **32**, L18607.

Levitus, S., J. I. Antonov, T. Boyer, R. Locarnini, H. Garcia, and A. Mishonov, 2009: Global ocean heat content 1955-2008 in light of recently revealed instrumentation problems. *Geophys. Res. Lett.*, **36**, L07608, doi:10.1029/2008GL037155.

Levitus, S., J. I. Antonov, T. P. Boyer, and C. Stephens, 2000: Warming of the World Ocean. *Science*, **287**, 2225–2229.

Levitus, S., J. I. Antonov, J. Wang, T. L. Delworth, K. W. Dixon, and A. J. Broccoli, 2001: Anthropogenic Warming of Earth's Climate System. *Science*, **292**, 267–270.

Levitus, S., R. Burgett, and T. P. Boyer, 1994: World Ocean Atlas 1994. Vol. 3, Salinity and Vol. 4, Temperature. Technical report, National Environmental Satellite, Data, and Information Service, Washington, DC (United States).

Lohmann, K., H. Drange, and M. Bentsen, 2009: Response of the North Atlantic subpolar gyre to persistent North Atlantic Oscillation like forcing. *Clim. Dyn.*, **32**, 273–285, doi:10.1007/s00382-008-0467-6.

Lund, D. C., J. Lynch-Stieglitz, and W. B. Curry, 2006: Gulf Stream density structure and transport during the past millennium. *Nature*, **444**, 601–604, doi:10.1038/nature05277.

Lyman, J. M., S. A. Good, V. V. Gouretski, M. Ishii, G. C. Johnson, M. D. Palmer, D. M. Smith, and J. K. Willis, 2010: Robust warming of the global upper ocean. *Nature*, **465**, 334–337, doi:10.1038/nature09043.

Mainelli, M., M. DeMaria, L. Shay, and G. Goni, 2008: Application of oceanic heat content estimation to operational forecasting of recent Atlantic Category 5 Hurricanes. *Weather and Forecasting*, **23**, 3–16.

Manabe, S. and R. J. Stouffer, 1994: Multiple-century response of a coupled ocean-atmosphere mocel to an increase of atmospheric carbon dioxide. *J. Clim.*, **7**, 5–23.

Mann, M., R. Bradley, and M. Hughe, 1999: Northern hemisphere temperatures during the past millennium: inferences, uncertainties, and limitations. *Geophys. Res. Lett.*, **26**, 759–762.

Mantua, N., S. Hare, Y. Zhang, J. Wallace, and R. Francis, 1997: A pacific interdecadal climate oscillation with impacts on salmon production. *Bull. Amer. Meteor. Soc.*, **78**, 1069–1080.

Marotzke, J. and P. Stone, 1995: Atmospheric transports, the thermohaline circulation, and flux adjustments in a simple coupled model. *J. Phys. Oceanogr.*, **25**, 1350–1364.

Marshall, J. C. and F. Schott, 1999: Open ocean convection: Observations, theory and models. *Rev. Geophys.*, **37-1**, 1–64.

Meehl, G., L. Goddard, J. Murphy, R. J. Stouffer, G. J. Boer, G. Danabasoglu, K. W. Dixon, M. A. Giorgetta, A. M. Greene, E. Hawkins, G. Hegerl, D. Karoly, N. Keenlyside, M. Kimoto, B. Kirtman, A. Navarra, R. Pulwarty, D. M. Smith, D. Stammer, and T. Stockdale, 2009: Decadal prediction: Can it be skillful? *Bull. Amer. Meteor. Soc.*, **90**, 14671485, doi:10.1175/2009BAMS2778.1.

Meehl, G. A., T. F. Stocker, W. D. Collins, P. Friedlingstein, A. T. Gaye, J. M. Gregory, A. Kitoh, R. Knutti, J. M. Murphy, A. Noda, S. C. B. Raper, I. G. Watterson, A. J. Weaver, and Z.-C. Zhao, 2007: *Global Climate Projections, in Climate Change 2007: The Physical Science Basis. Contribution of Working Group I to the Fourth Assessment Report of the Intergovernmental Panel on Climate Change*, Cambridge University Press, Cambridge, United Kingdom and New York, NY, USA.

Mignot, J. and C. Frankignoul, 2005: The Variability of the Atlantic Meridional Overturning Circulation, the North Atlantic Oscillation, and the El Niño-Southern Oscillation in the Bergen Climate Model. *J. Clim.*, **18**, 2361–2375.

Miller, L. and B. C. Douglas, 2004: Mass and volume contributions to twentieth-centur global sea level rise. *Nature*, **428**, 406–409.

Min, S., S. Legutke, A. Hense, and W. Kwon, 2005a: Internal variability in a 1000-yr control simulation with the coupled climate model ECHO-G -I. Near surface temperature, precipitation and sea level pressure. *Tellus*, **57A**, 605–621.

— 2005b: Internal variability in a 1000-yr control simulation with the coupled climate model ECHO-G -II. El Niño Sourthern Oscillation and North Atlantic Oscillation. *Tellus*, **57A**, 622–640.

Monahan, A., J. Alexander, and A. Weaver, 2008: Stochastic models of the meridional overturning circulation: time scales and patterns of variability. *Phil. Trans. R. Soc. A*, **366**, 2525–2542, doi:10.1098/rsta.2008.0045.

Moore, G. W. K., 2003: Gale force winds over the Irminger Sea to the east of Cape Farewell, Greenland. *Geophys. Res. Lett.*, **30**, 1894, doi:10.1029/2003GL018012.

Msadek, R., K. Dixon, T. Delworth, and W. Hurlin, 2010: Assessing the predictability of the Atlantic meridional overturning circulation and associated fingerprints. *Geophys. Res. Lett.*, **37**, L19608, doi:10.1029/2010GL044517.

Msadek, R. and C. Frankignoul, 2009: Atlantic multidecadal oceanic variability and its influence on the atmosphere in a climate model. *Clim. Dyn.*, **33**, 45–62, doi:10.1007/s00382-008-0452-0.

Nakicenovic, N., J. Alcamo, G. Davis, B. de Vries, J. Fenhann, S. Gaffin, K. Gregory, A. Grubler, T. Y. Jung, T. Kram, E. L. L. Rovere, L. Michaelis, S. Mori, T. Morita, W. Pepper, H. Pitcher, L. Price, K. Riahi, A. Roehrl, H. H. Rogner, A. Sankovski, M. Schlesinger, P. Shukla, S. Smith, R. Swart, S. van Rooijen, N. Victor, and Z. Dadi, 2000: *Special Report on Emissions Scenarios*. Cambridge University Press, 599 pp.

Newman, M., G. Compo, and M. Alexander, 2003: ENSO-forced variability of the Pacific decadal oscillation. **16**, 3853–3857.

Olsen, S. M., B. Hansen, D. Quadfasel, and S. Østerhus, 2008: Observed and modelled stability of overflow across the Greenland–Scotland ridge. *Nature*, **455**, 519–522, doi:10.1038/nature07302.

Orsi, A. H., G. C. Johnson, and J. L. Bullister, 1999: Circulation, mixing, and production of Antarctic Bottom Water. *Progress in Oceanography*, **43**, 55–109.

Ortega, P., J. F. González-Rouco, M. Montoya, and H. Beltrami, 2011a: Variability of the ocean heat content during the last millennium. An assessment with the ECHO-g Model. *Manuscript in preparation*.

Ortega, P., E. Hawkins, and R. T. Sutton, 2011b: Processes governing the predictability of the Atlantic Meridional Overturning Circulation in a coupled GCM. *Clim. Dyn.*, **37**, 1771–1782, doi:10.1007/s00382-011-1025-1.

Ortega, P., M. Montoya, F. González-Rouco, J. Mignot, and S. Legutke, 2011c: Variability of the Atlantic meridional overturning circulation in the last millennium and two IPCC scenarios. *Clim. Dyn. (accepted)*, doi:10.1007/s00382-011-1081-6.

Osborn, T. J., S. C. B. Raper, and K. R. Briffa, 2006: Simulated climate change during the last 1000 years: comparing the ECHO-G general circula-

tion model with the MAGICC simple climate model. *Clim. Dyn.*, **27**, 185–197, doi:doi:10.1007/s00382-006-0129-5.

Ottera, O. H., M. Bentsen, H. Drange, and L. Suo, 2010: External forcing as a metronome for Atlantic multidecadal variability. *Nature Geoscience*, **3**, 688–694, doi:10.1038/NGEO955.

Palmer, M. D., S. A. Good, K. Haines, N. A. Rayner, and P. A. Stott, 2009: A new perspective on warming of the global oceans. *Geophys. Res. Lett.*, **36**, L20709, doi:10.1029/2009GL039491.

Palmer, M. D., D. J. Mcneall, and N. J. Dunstone, 2011: Importance of the deep ocean for estimating decadal changes in earth's radiation balance. *Geophys. Res. Lett.*, **38**, L13707, doi:10.1029/2011GL047835.

Peng, S., W. Robinson, S. Li, and M. Hoerling, 2005: Tropical Atlantic SST forcing of coupled North Atlantic seasonal responses. *J. Clim.*, **18**, 480–496.

Pfeffer, W. T., J. T. Harper, and S. O'Neel, 2008: Kinematic constraints on glacier contributions to 21st-century sea-level rise. *Science*, **321**, 1340–1343, doi:10.1126/science.1159099.

Pickart, R. S., M. A. Spall, M. J. Ribergaard, G. W. K. Moore, and R. F. Milliff, 2003: Deep convection in the Irminger Sea forced by the Greenland tip jet. *Nature*, **424**, 152–156.

Pohlmann, H., J. H. Jungclaus, A. Köhl, D. Stammer, and J. Marotzke, 2009: Initializing Decadal Climate Predictions with the GECCO Oceanic Synthesis: Effects on the North Atlantic. *J. Clim.*, **22**, 3926–3938, doi:10.1175/2009JCLI2535.1.

Rahmstorf, S., 2007: A semi-empirical approach to projecting future sea-level rise. *Science*, **315**, 368–370, doi:10.1126/science.1135456.

Rahmstorf, S. and A. Ganopolski, 1999: Long-term global warming scenarios computed with an efficient coupled climate model. *Climatic Change*, **43**, 353.

Reynaud, T. H., A. J. Weaver, and R. J. Greatbatch, 1995: Summer mean circulation of the northwestern Atlantic Ocean. *J. Geophys. Res.*, **100**, 779–816.

Rind, D., D. Shindell, J. Perlwitz, J. Lerner, P. Lonergan, J. Lean, and C. McLinden, 2004: The relative importance of solar and anthropogenic forcing of climate change between the maunder minimum and the present. *J. Clim.*, **17**, 906–929.

Roberts, M. and R. Wood, 1997: Topographic sensitivity studies with a Bryan–Cox-type ocean model. *J. Phys. Oceanogr.*, **27**, 823–836.

Rodwell, M., D. Rowell, and C. Folland, 1999: Oceanic forcing of the wintertime North Atlantic Oscillation and European climate. *Nature*, **398**, 320–323.

Roeckner, E., K. Arpe, L. Bengtsson, M. Christoph, M. Claussen, L. Dumenil, M. Esch, M. Giorgetta, U. Schlese, and U. Schulzweida, 1996: The atmospheric general circulation model ECHAM4: model description and simulation

of present-day climate. Technical Report 218, Max-Planck-Institut fuer Meterologie, Hamburg, Germany.

Saravanan, R. and J. McWilliams, 1997: Stochasticity and Spatial Resonance in Interdecadal Climate Fluctuations. *J. Clim.*, **10**, 2299–2320.

Schaeffer, M., F. Selten, J. Opsteegh, and H. Goosse, 2004: The influence of ocean convection patterns on high-latitude climate projections. *J. Clim.*, **17**, 4316–4329.

Schmittner, A., M. Latif, and B. Schneider, 2005: Model projections of the North Atlantic thermohaline circulation for the 21st century assessed by observations. *Geophys. Res. Lett*, **32**, L23710, doi: 10.1029/2005GL024368.

Schneider, B., M. Latif, and A. Schmittner, 2007: Evaluation of Different Methods to Assess Model Projections of the Future Evolution of the Atlantic Meridional Overturning Circulation. *J. Clim.*, **20**, 2121–2132, doi:10.1175/JCLI4128.1.

Sedláček, J. and L. A. Mysak, 2009a: A model study of the Little Ice Age and beyond: changes in ocean heat content, hydrography and circulation since 1500. *Clim. Dyn.*, **33**, 461–475, doi:10.1007/s00382-008-0503-6.

— 2009b: Sensitivity of sea ice to wind-stress and radiative forcing since 1500: a model study of the Little Ice Age and beyond. *Clim. Dyn.*, **32**, 817–831, doi:10.1007/s00382-008-0406-6.

Servonnat, J., P. Yiou, M. Khodri, D. Swingedouw, and S. Denvil, 2010: Influence of solar variability, CO2 and orbital forcing between 1000 and 1850 AD in the IPSLCM4 model. *Clim. Past.*, **6**, 445–460, doi:10.5194/cp-6-445-2010.

Shindell, D., G. Schmidt, M. Mann, D. Rind, and A. Waple, 2001: Solar forcing of regional climate change during the Maunder Minimum. *Science*, **294**, 2149–2152, doi:10.1126/science.1064363.

Smith, D. M., S. Cusack, A. Colman, C. Folland, G. Harris, and J. Murphy, 2007: Improved Surface Temperature Prediction for the Coming Decade from a Global Climate Model. *Science*, **317**, 796–799, doi:10.1126/science.1139540.

Stenchikov, G., T. Delworth, V. Ramaswamy, R. J. Stouffer, A. Wittenberg, and F. Zeng, 2009: Volcanic signals in oceans. *J. Geophys. Res.-Atmos.*, **114**, D16104, doi:10.1029/2008JD011673.

Stendel, M., I. Mogensen, and J. Christensen, 2006: Influence of various forcings on global climate in historical times using a coupled atmosphere–ocean general circulation model. *Clim. Dyn.*, **26**, 1–15, doi:10.1007/s00382-005-0041-4.

Stephenson, D., V. Pavan, M. Collins, M. Junge, and R. Quadrelli, 2006: North Atlantic Oscillation response to transient greenhouse gas forcing and the impact on European winter climate: a CMIP2 multi-model assessment. *Clim. Dyn.*, **27**, 401–420.

Stevens, M. B., J. E. Smerdon, J. F. González-Rouco, M. Stieglitz, and H. Beltrami, 2007: Effects of bottom boundary condition placement on subsurface

heat storage: Implications for climate model simulations. *Geophys. Res. Lett.*, **34**, L02702,doi:10.1029/2006GL028 546.

Stouffer, R. J., J. Yin, J. M. Gregory, K. W. Dixon, M. J. Spelman, W. Hurlin, A. J. Weaver, M. Eby, G. M. Flato, H. Hasumi, A. Hu, J. H. Jungclaus, I. V. Kamenkovich, A. Levermann, M. Montoya, S. Murakami, S. Nawrath, A. Oka, W. R. Peltier, D. Y. Robitaille, A. P. Sokolov, G. Vettoretti, and S. L. Weber, 2006: Investigating the causes of the response of the thermohaline circulation to past and future climate changes. *J. Clim.*, **19**, 1365–1387.

Sun, S. and J. Hansen, 2003: Climate simulations for 1951–2050 with a Coupled Atmosphere-Ocean Model. *J. Clim.*, **16**, 2807–2826.

Sutton, R. T. and D. L. R. Hodson, 2003: Influence of the Ocean on North Atlantic Climate Variability 1871-1999. *J. Clim.*, **16**, 3296–3313.

— 2005: Atlantic Ocean Forcing of North American and European Summer Climate. *Science*, **309**, 115–118, doi:10.1126/science.1109496.

Swingedouw, D., L. Terray, C. Cassou, A. Voldoire, D. Salas-Mélia, and J. Servonnat, 2010: Natural forcing of climate during the last millennium: fingerprint of solar variability. *Clim. Dyn.*, **36**, 1349–1364, doi:DOI 10.1007/s00382-010-0803-5.

Talley, L. D., 2003: Shallow, intermediate, and deep overturning components of the global heat budget. *J. Phys. Oceanogr.*, **33**, 530–560.

Talley, L. D., J. L. Reid, and P. E. Robbins, 2003: Data-based meridional overturning streamfunctions for the global ocean. *J. Clim.*, **16**, 3213–3226.

Tanner, W., 1992: 3000 years of sea level change. *Bull. Amer. Meteor. Soc.*, **73**, 297–303.

Tapping, K. F., D. Boteler, P. Charbonneau, A. Crouch, A. Manson, and H. Paquette, 2007: Solar magnetic activity and total irradiance since the Maunder Minimum. *Solar Physics*, **246**, 309–326, doi:10.1007/s11207- 007-9047-x.

Te Raa, L. and H. Dijkstra, 2002: Instability of the thermohaline ocean circulation on interdecadal timescales. *J. Phys. Oceanogr.*, **32**, 138–160.

Tett, S., R. Betts, T. Crowley, J. Gregory, T. Johns, A. Jones, T. Osborn, E. Öström, D. Roberts, and M. Woodage, 2007: The impact of natural and anthropogenic forcings on climate and hydrology since 1550. *Clim. Dyn.*, **28**, 3–34, doi:10.1007/s00382-006-0165-1.

Thorpe, R. B., J. M. Gregory, T. C. Johns, R. A. Wood, and J. F. B. Mitchell, 2001: Mechanisms determining the Atlantic Thermohaline Circulation response to greenhouse gas forcing in a non-flux-adjusted coupled climate model. *J. Clim.*, **14**, 3102–3116.

Timmermann, A., M. Latif, R. Voss, and A. Grötzner, 1998: Northern Hemispheric Interdecadal Variability: a Coupled Air-Sea Mode. *J. Clim.*, **11**, 1906–1931.

Timmermann, A., Y. Okumura, S. I. An, A. Clement, B. Dong, E. Guilyardi, A. Hu, J. H. Jungclaus, M. Renold, T. F. Stocker, R. J. Stouffer, R. Sutton, S. P. Xie, and J. Yin, 2007: The Influence of a Weakening of the Atlantic Meridional Overturning Circulation on ENSO. *J. Clim.*, **20**, 4489–4919.

Trenberth, K., 1997: The definition of El Niño. *Bull. Amer. Meteor. Soc.*, **78**, 2771–2778.

— 2010: The ocean is warming, isn't it? *Nature*, **465**, 304.

Trenberth, K. and J. T. Fasullo, 2010: Tracking earth's energy. *Science*, **328**, 316–317, doi:10.1126/science.1187272.

Trenberth, K. E. and J. M. Caron, 2001: Estimates of meridional atmosphere and ocean heat transport. *Clim. Dyn.*, **14**, 3433–3443.

Trenberth, K. E. and D. J. Shea, 1987: On the evolution of the southern oscillation. *Monthly Weather Review*, **115**, 3078–3096.

Trouet, V., J. Esper, N. Graham, A. Baker, J. Scourse, and D. C. Frank, 2009: Persistent positive North Atlantic Oscillation mode dominated the Medieval Climate Anomaly. *Science*, **324**, 78–80, doi:10.1126/science.1166349.

Van De Plassche, O., K. Van Der Borg, and A. De Jong, 1998: Sea level-climate correlation during the past 1400 yr. *Geology*, **26**, 319–322.

Vellinga, M. and R. A. Wood, 2002: Global climatic impacts of a collapse of the Atlantic thermohaline circulation. *Climatic Change*, **54**, 251–267.

Vellinga, M. and P. Wu, 2004: Low-latitude freshwater influence on centennial variability of the Atlantic thermohaline circulation. *J. Clim.*, **17**, 4498–4511.

Vermeer, M. and S. Rahmstorf, 2009: Global sea level linked to global temperature. *Proc. Natl. Acad. Sci.*, **106**, 21527–21532.

von Storch, H., E. Zorita, J. M. Jones, Y. Dimitriev, F. Gonzalez-Rouco, and S. F. B. Tett, 2004: Reconstructing Past Climate from Noisy Data. *Science*, **306**, 679–682, doi:10.1126/science.1096109.

Wallace, J. and D. Gutzler, 1981: Teleconnections in the geopotential height field during the Northern Hemisphere winter. *Monthly Weather Review*, **109**, 784–812.

Wang, Y., J. Lean, and N. Sheeley, 2005: Modeling the sun's magnetic field and irradiance since 1713. *Astrophysical Journal*, **625**, 522–538.

Weaver, A. H. and S. Valcke, 1998: On the variability of the thermohaline circulation in the gfdl coupled model. *J. Clim.*, **11**, 759–767.

Weaver, A. J. and E. Sarachik, 1991: Evidence for decadal variability in an ocean general circulation model: An advective mechanism. *Atmosphere-Ocean*, **29**, 197–231.

Willis, J., D. Roemmich, and B. Cornuelle, 2004: Interannual variability in upper ocean heat content, temperature, and thermosteric expansion on global scales. *J. Geophys. Res.*, **109**, C12036, doi:10.1029/2003JC002260.

Wolff, J. O., E. Maier-Reimer, and S. Legutke, 1997: The Hamburg Ocean Primitive Equation Model. Technical Report 13, DKRZ, Hamburg, Germany.

Wu, P. and C. Gordon, 2002: Oceanic influence on North Atlantic climate variability. *J. Clim.*, **15**, 1911–1925.

Zhang, R., 2008: Coherent surface-subsurface fingerprint of the atlantic meridional overturning circulation. *Geophys. Res. Lett.*, **35**, L20705, doi:10.1029/2008GL035463.

Zhang, R. and T. Delworth, 2006: Impact of Atlantic multidecadal oscillations on India/Sahel rainfall and Atlantic hurricanes. *Geophys. Res. Lett.*, **33**, L17712, doi:10.1029/2006GL026267.

— 2007: Impact of the Atlantic multidecadal oscillation on North Pacific climate variability. *Geophys. Res. Lett.*, **34**, L23708, doi:10.1029/2007GL031601.

Zhang, Y., J. Wallace, and D. S. Battisti, 1997: ENSO-like interdecadal variability: 1900-93. *J. Clim.*, **10**, 1004–1020.

Zorita, E., F. Gonzalez-Rouco, and H. von Storch, 2007: Comments on "Testing the fidelity of methods used in proxy-based reconstructions of past climate". *J. Clim.*, **20**, 3693–3698.

Zorita, E., J. F. González-Rouco, and S. Legutke, 2003: Testing the Mann et al. (1999) approach to paleoclimate reconstructions in the context of a 1000-yr control simulation with the ECHO-G coupled climate model. *J. Clim.*, **16**, 1378–1390.

Zorita, E., J. F. González-Rouco, H. von Storch, J. P. Montávez, and F. Valero, 2005: Natural and anthropogenic modes of surface temperature variations in the last thousand years. *Geophys. Res. Lett.*, **32**, L08707.

Zorita, E., H. von Storch, F. J. González-Rouco, J. L. U. Cubasch, S. Legutke, I. Fischer-Bruns, and U. Schlese, 2004: Climate evolution in the last five centuries simulated by an atmosphere-ocean model: global temperatures, the North Atlantic Oscillation and the Late Maunder Minimum. *Meteorologische Zeitschrift*, **13**, 271–289.

Glossary

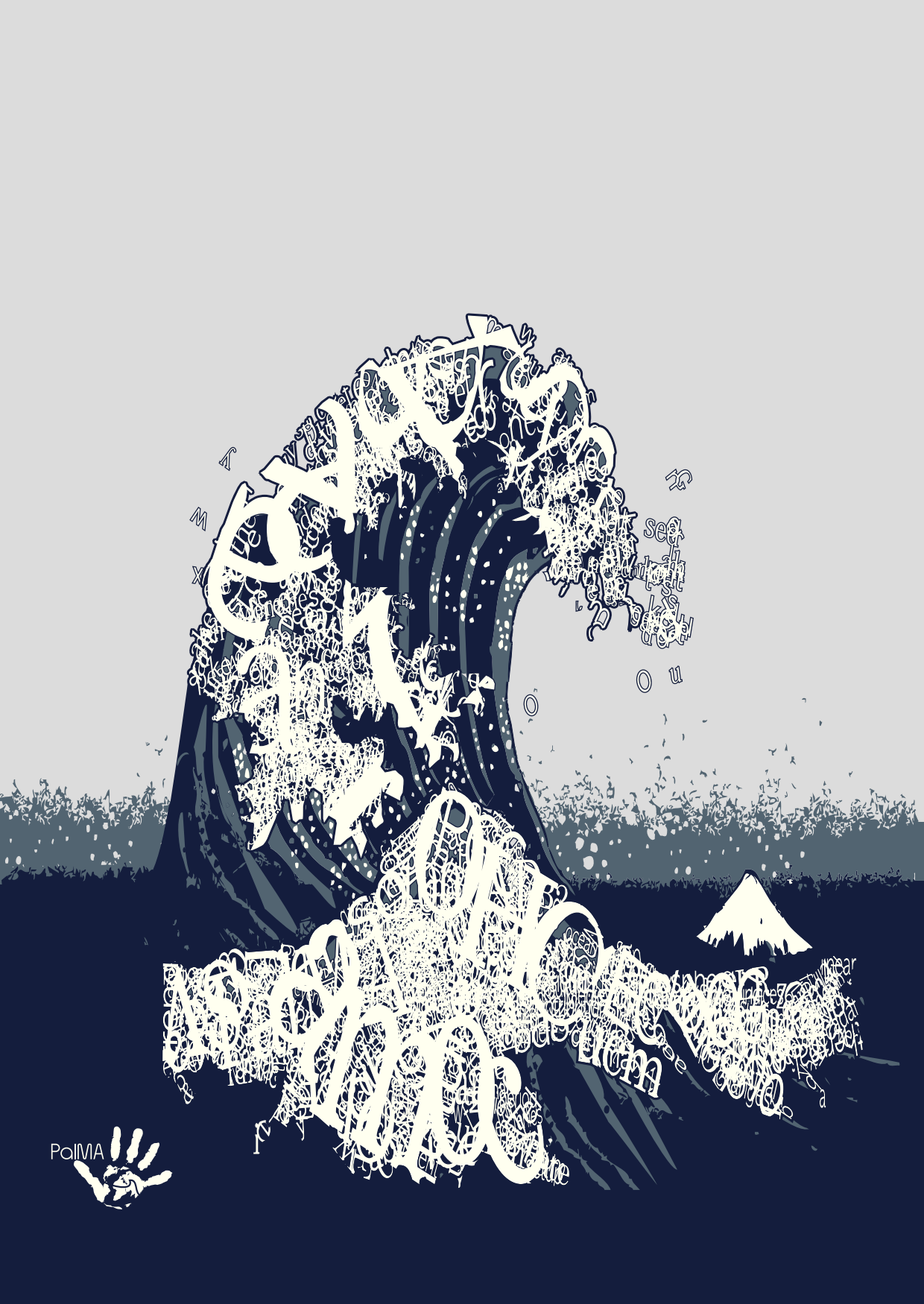
PalMA